HVDC Interaction Studies Using Small Signal Stability Assessment

by

Chandana Karawita

A dissertation submitted to the Faculty of Graduate Studies in partial fulfillment of the requirements for the degree of

Doctor of Philosophy

The Department of Electrical and Computer Engineering

The University of Manitoba

Winnipeg, Manitoba, Canada

THE UNIVERSITY OF MANITOBA

FACULTY OF GRADUATE STUDIES

*****

COPYRIGHT PERMISSION

HVDC Interaction Studies Using Small Signal Stability Assessment

BY

Chandana Karawita

A Thesis/Practicum submitted to the Faculty of Graduate Studies of The University of Manitoba in partial fulfillment of the requirement of the degree

Of

Doctor of Philosophy

To my wife and daughter.

Acknowledgements

First, my sincere thanks must go to my advisor, Professor Udaya Annakkage for his continuous advice, guidance and encouragement throughout the course of this work. I consider myself privileged to have the opportunity to work under his guidance. I greatly appreciate the advice and assistance received from Professor Ani Gole. I am also grateful to Professor Rohan Lucas of University of Moratuwa, Sri Lanka for useful inputs received, while he was working in the University of Manitoba as a visiting professor. I must also thank the technical staff at the Department of Electrical and Computer Engineering, especially Mr. Erwin Dirks for his support.

The financial support received from the University of Manitoba, the provincial government of Manitoba and the National Science and Engineering Research Council is greatly appreciated.

I would like to thank Dr. Bathiya Jayasekara, all my friends and the staff of the Department of Electrical and Computer Engineering for their continuous encouragement and for making my years at the University of Manitoba a pleasant experience.

This acknowledgement would not be complete without thanking my family. I extend my heartfelt gratitude to my wife and the daughter. They were always understanding and encouraged me during my hard times. I would like to also thank my parents and the sister for all the love and support.

Chandana Karawita

April 2009

Summary

Small signal stability analysis is typically concerned with electromechanical oscillations in a power system. For this purpose, it is adequate to model the transmission system using a constant admittance matrix. For torsional oscillations and HVDC interactions, the frequency of interest is much higher and the constant admittance representation is not sufficient. The modeling details necessary to adequately represent the dynamics of the HVDC converters and the AC network are investigated and the models are validated against an electromagnetic transient simulation program. The thesis shows that AC network dynamics must be modeled in order to obtain meaningful results from the small signal stability study of the high frequency interactions (up to 200Hz). The dynamic phasor representation of the AC network is used to model the network and the dynamic devices are combined with the network model using current injection models. However, it is impractical to model the dynamics of the entire AC network of a large power system because of high computational burden.

This thesis proposes a hybrid model, which allows the parts of the transmission network in the vicinity of HVDC converters or any other dynamic devices to be modeled with their dynamics and the remaining parts to be modeled as constant admittances. This model can be efficiently used for large power systems. The proposed hybrid methodology is validated against an electromechanical transient program using time responses.

The thesis presents an analysis of multi-in-feed HVDC interactions using small signal analysis techniques. A small test system with two HVDC in-feeds and the IEEE New England 39 bus system with two HVDC in-feeds are used to demonstrate the presence of interactions in those systems. The case studies presented in the thesis indicate that it is possible to have interactions between the HVDC terminals in an

AC system. The thesis recommends that a small signal interaction study similar to what is presented in the thesis should be performed to identify these interactions. For large power systems, the proposed hybrid model can be used to accurately and efficiently analyze these interactions.

Furthermore, the thesis demonstrates that the small signal stability assessment techniques described in the thesis can be used to identify the HVDC-generator-turbine torsional interactions in power systems. Two case studies are performed using the small signal model including the dynamics of the entire AC network and the proposed hybrid small signal model. The case studies indicate that it is possible to have subsynchronous frequency torsional interactions between the HVDC systems and generator-turbine units and these interactions may cause instabilities under certain conditions. Further, the electromagnetic transient simulations validate these findings.

The thesis further investigates the inclusion of the auxiliary controllers at the HVDC terminal to control the electromechanical and torsional oscillations of the nearby generator-turbine units. The design procedures are briefly described using small signal stability assessment and the performances of them are evaluated using time domain simulations.

In general, the analytical techniques proposed in this thesis would be useful to analyze the high frequency interactions of HVDC systems, generator-turbine units and FACTS devices. The modeling techniques can be used for very large power systems.

List of Principal Symbols

t	Time
ω_0	Fundamental angular frequency of power system
V_l	Line to line rms voltage
δ	Generator rotor angle or bus voltage angle
V_R, V_I	Real and imaginary components of AC bus voltage
I_R, I_I	Real and imaginary components of AC current injected to a bus
X_c	Converter transformer reactance referred to DC side
T	Converter transformer turns ratio (AC/DC)
B	Number of 6-pulse bridges in a converter
α, μ, γ	Converter firing angle, commutation angle and extinction angle
L_{dc}, R_{dc}, C	DC line inductance, resistance and capacitance
L_{eff}	Effective inductance of an HVDC terminal
K_{Pr}, K_{Ir}	Proportional and integral gains of rectifier current controller
$I_{dc,order}$	Current reference of rectifier current controller
$X_{\alpha r}$	State variable of rectifier current controller
K_{Pi}, K_{Ii}	Proportional and integral gains of inverter controller
γ_{order}	Extinction angle reference of inverter extinction angle controller
$V_{dc,order}$	DC voltage reference of inverter DC voltage controller
$X_{\alpha i}$	State variable of inverter extinction angle/DC voltage controller
K_{PP}, K_{II}	Proportional and integral gains of phase lock oscillator
R_{ij}, L_{ij}	Series resistance and inductance between nodes i and j
C_i	Shunt capacitance connected to node i
$[Y_{bus}]$	Bus admittance matrix
ω_{gen}	Generator angular speed
ω_{HP}, ω_{IP}	Angular speeds of HP and IP turbines
ω_{LPA}, ω_{LPB}	Angular speeds of LPA and LPB turbines
δ_{HP}, δ_{IP}	Rotor angles of HP and IP turbines
δ_{LPA}, δ_{LPB}	Rotor angles of LPA and LPB turbines
K_d, H	Damping and inertia constants of a generator
T_m, T_e	Generator input mechanical torque and output electrical torque
$[A]$, $[B]$	System matrix and input matrix of a state space model
$[\Lambda]$	Eigenvalue matrix
λ	An eigenvalue
f, ζ	Frequency and damping ratio (D) of an eigenvalue
$[\Phi]$, $[\Psi]$	Right and left eigenvector matrix
Φ_i, Ψ_i	Right and left eigenvectors of i^{th} eigenvalue
p_i	Participation vector of i^{th} eigenvalue

Table of Contents

1 Introduction 1
1.1 Background 1
1.2 Thesis Objectives 6
1.3 Thesis Outline 7

2 Linearized Models of Power Systems 10
2.1 Introduction 10
2.2 Linearized Model of an HVDC System 12
2.2.1 Converter Model 13
2.2.2 DC Transmission System 22
2.2.3 HVDC Controllers 23
2.2.4 State Space Model of HVDC System 29
2.2.5 Validation of Linearized HVDC Model 30
2.3 AC Network Model 37
2.3.1 Admittance Matrix Representation 37
2.3.2 Dynamic Network Model 38
2.4 Generator Model 41
2.5 Multi-Mass Turbine Model 42
2.6 Linearized Model of Entire Power System 42
2.6.1 Conventional Model 42
2.6.2 Small Signal Model With Network Dynamics 43
2.7 Adequacy of Linearized Models of Power Systems 46
2.8 Concluding Remarks 51

3 Hybrid AC Network Model for Large Power Systems 53
3.1 Introduction 53
3.2 Proposed Hybrid AC Network Model 54
3.3 Validation of Proposed Model 57
3.3.1 Small Signal Models of Test System 57
3.3.2 Validations Using Time Domain Simulations 60
3.4 Concluding Remarks 64

4 Small Signal Stability Assessment of Power Systems 66
4.1 Introduction 66
4.2 Stability of Linearized Systems 67
4.3 Modes and Modal Characteristics 68
4.3.1 Modes 68
4.3.2 Mode Shapes (Right Eigenvectors) 70
4.3.3 Left Eigenvectors 70

4.3.4 Participation Factors 71
4.3.5 Mode Controllability and Observability 72
4.4 Summary: Modal Analysis Used in The Thesis 73

5 HVDC Interactions in Power Systems 75
5.1 Introduction 75
5.2 Case Study-1: Multi-in-feed HVDC Interactions 76
5.2.1 Small Signal Model of Test System 76
5.2.2 AC Network Interactions 78
5.2.3 DC Line Resonances 78
5.2.4 Controller Interactions 79
5.2.5 Effect of Tie Line Impedance 81
5.2.6 Effect of Current Controller 81
5.2.7 HVDC Controllers For Electromechanical Oscillations 84
5.2.8 Summary of Analysis 85
5.3 Case Study-2:
HVDC Interactions in Large Power Systems 87
5.3.1 HVDC Interaction Modes 88
5.3.2 Electromechanical Modes 91
5.3.3 Summary of Analysis 92
5.4 Concluding Remarks 92

6 HVDC-Generator-Turbine Torsional Interactions 94
6.1 Introduction 94
6.2 HVDC-Generator-Turbine Torsional Interactions Analysis Using a Small Test System 95
6.2.1 Linearized Model 95
6.2.2 Modal Analysis of Test System 97
6.2.3 HVDC-Generator-Turbine Torsional Interactions 99
6.2.4 Design of SSDC Using Small Signal Stability Assessment . . . 103
6.3 HVDC-Generator-Turbine Torsional Interactions Analysis in Large Power Systems 108
6.3.1 Modal Analysis of Test System 108
6.3.2 HVDC-Generator-Turbine Torsional Interactions 110
6.3.3 Control of Torsional Modes Through HVDC 111
6.3.4 Importance of The Hybrid Model 117
6.4 Concluding Remarks 117

7 Conclusions 119
7.1 General Conclusions 119
7.2 Contributions 122
7.3 Suggestions for Future Research 124

A Test Systems Data 126
A.1 CIGRE Benchmark HVDC Test System 126
A.2 Multi-in-feed HVDC Test System 127
A.2.1 AC voltage Sources 127
A.2.2 HVDC systems 127
A.2.3 Generator at S2 128
A.3 New England 39 Bus System 129
A.3.1 Power Flow - AC Bus Data 129
A.3.2 Power Flow - Load Data 130
A.3.3 Power Flow - Generator Data 130
A.3.4 Power Flow - Line Data 131
A.3.5 Power Flow - Transformer Data 132
A.3.6 Dynamic Data - Generators 132
A.3.7 Dynamic Data - Exciters (AC4A) 132
A.3.8 Dynamic Data - Turbines & Governors (HyTur1 and HyGov1) 133

B AC Network Models 134
B.1 Linearized AC network models-An Example 134
B.1.1 Admittance Matrix Representation 135
B.1.2 Dynamic Phasor Representation 136

C Generator, Exciter And Governor-Turbine Models 140
C.1 Linearized Generator Models 140
C.1.1 Conventional Generator Model 140
C.1.2 Generator Model Including Stator Transients 145
C.2 Linearized Exciter Model (AC4A) 150
C.3 Linearized Governor-Turbine Model 151
C.4 State Space Generator Model With Exciter And Governor 153
C.4.1 Generator-Exciter Combination 154
C.4.2 Generator-Governor-Turbine Combination 154
C.4.3 Overall State Space Model 155
C.5 Multi Mass Turbine Model 155

D An Algorithm For Proposed Hybrid Small Signal Model 157

E Governor-Turbine Torsional Interactions With AC Network 160
E.1 Test System -IEEE First Benchmark Model 160
E.2 Small Signal Stability Model of Test System 161
E.3 Generator-Turbine-AC network Torsional Interactions 162
E.4 Summary of Analysis 166

Acronyms 167

List of Figures

2.1 6-pulse converter bridge 14
2.2 DC side voltages and AC side phase a current of a 6-pulse Bridge . . 16
2.3 Phase Locked Oscillator 21
2.4 DC transmission system 22
2.5 HVDC operating points at nominal conditions 24
2.6 HVDC control schemes 25
2.7 Linearized model of HVDC system 28
2.8 CIGRE benchmark test system with infinite AC buses 31
2.9 Frequency response between rectifier firing angle and state variables/outputs (magnitude is given as % change for a 5% change in α_r) 32
2.10 Frequency response between rectifier AC voltage and state variables/outputs (magnitude is given as % change for a 5% change in $V_{mag,r}$) 34
2.11 Changes in state variables for a 5%, 0.3s pulse on the rectifier current controller input. 35
2.12 Changes in state variables for a 5%, 200Hz sinusoidal change in rectifier AC voltage magnitude. 36
2.13 Test system used to discuss implementation aspects of dynamic network model 44
2.14 Multi-in-feed HVDC test system 47
2.15 Accuracy of different models (initial changes in Rectifier side DC currents for a 5%, 0.3s pulse on the current controller input in HVDC1) 48
2.16 Changes in Rectifier side DC currents for a 5%, 0.3s pulse on the current controller input in HVDC1 (An extended simulation) 49
2.17 Change in generator speed for a 5%, 0.3s pulse on the current controller input in HVDC1 49
2.18 Changes in Rectifier side DC currents for a 5%, 200Hz sinusoidal change of the HVDC1 rectifier side AC source voltage (V_{S1}) 50

3.1 Transmission line model at the boundary 55
3.2 39 bus test system with two HVDC in-feeds 58
3.3 Initial changes in rectifier side DC currents for a 5%, 0.3s step on the current controller input in HVDC1 62
3.4 Initial changes in inverter side DC currents for a 5%, 0.3s step on the current controller input in HVDC1 62
3.5 Changes in generator rotor speeds (in pu) for a 5%, 0.3s step on the current controller input in HVDC1 63
3.6 Changes in rectifier side DC currents for a 10%, 200Hz 200Hz sinusoidal change of the HVDC1 rectifier side AC source voltage 64

5.1 Multi-in-feed HVDC test system (redrawn - same as Figure 2.14) . . 76

5.2 Participation of state variables in mode 6 of Model-1 (Table 5.1). Note that, the state variables of HVDC systems are arranged in the order [$X_{\alpha r}$, $X_{\alpha i}$, I_{dcr}, I_{dci}, V_{cap} and four PLO variables]. 79
5.3 Mode shapes of major participants - Modes 6,7,8 and 9 (Table 5.1) . 80
5.4 Participation of state variables in mode 9 of Model-1 (Table 5.1). Note that, the state variables of HVDC systems are arranged in the order [$X_{\alpha r}$, $X_{\alpha i}$, I_{dcr}, I_{dci}, V_{cap} and four PLO variables]. 81
5.5 Participation of state variables in the similar mode corresponding to mode 6 (Table 5.1) when the tie line impedance is increased by 5 times 82
5.6 Participation of state variables in the similar mode corresponding to mode 9 (Table 5.1) when the tie line impedance is increased by 5 times 82
5.7 Polar plot of modes 6,7,8,9 and 10 - HVDC1 rectifier PI controller input gain is changed from 0.2 to 10 83
5.8 Change in rectifier side DC current of HVDC1 for a 5%, 0.3s step on the current controller input in HVDC1, when the HVDC1 rectifier PI controller input gain is 0.2 84
5.9 Change in generator speed for a 5%, 0.3s step on the current controller input in HVDC1, when the HVDC damping controller gain is 50. . . 86
5.10 Participations of HVDC1 and HVDC2 state variables in Mode-a . . 89
5.11 Participations of HVDC1 and HVDC2 state variables in Mode-b . . 89
5.12 Modeshapes of HVDC interaction modes 90

6.1 Test system used to analyze HVDC-generator turbine interactions . . 96
6.2 Changes in rectifier side DC currents for a 10%, 10ms pulse on the rectifier current controller input 97
6.3 Changes in generator rotor speed (in pu) for a 10%, 10ms pulse on the rectifier current controller 97
6.4 Participation factors (%) of multi-mass speed terms and HVDC state variables in Modes A and B 101
6.5 Changes in rectifier side DC currents for a 10%, 10ms pulse on the rectifier current controller input (when current controller gains are adjusted) 102
6.6 Changes in generator rotor speed (in pu) for a 10%, 10ms pulse on the rectifier current controller (when current controller gains are adjusted) 102
6.7 Subsynchronous damping controller attached to the rectifier current controller 103
6.8 Controllability of torsional modes through rectifier current controller input 104
6.9 Phase plot of frequency response between generator electrical torque and rectifier current controller input 105
6.10 Changes in mode dampings with SSDC gain 106

6.11 Changes in rectifier side DC currents for a 10%, 10ms pulse on the rectifier current controller input (when SSDC is connected at rectifier) 107
6.12 Changes in generator rotor speed (in pu) for a 10%, 10ms pulse on the rectifier current controller (when SSDC is connected at rectifier) . . . 107
6.13 39 bus test system used to analyze HVDC-generator turbine torsional interactions 109
6.14 Change in generator-36 speed (in pu) for a 10%, 10ms pulse on the rectifier current controller input 113
6.15 Changes in DC side currents of HVDC system for a 10%, 10ms pulse on the rectifier current controller input 114

B.1 AC Network Example 134

C.1 AC4A exciter control block diagram (simplified as required for small signal stability assessment) 150
C.2 Governor-turbine control block diagram (simplified as required for small signal stability assessment) 152
C.3 Multi-mass generator-turbine system 155

D.1 Flowchart of proposed hybrid small signal model 158

E.1 IEEE first benchmark model for subsynchronous resonance studies - fault reactance is not included 161
E.2 Polar plot of the modes obtained when the compensation level is changed 163
E.3 Damping versus compensation level characteristics of the modes . . . 164
E.4 Change in generator speed (in pu) for a 5%, 100ms pulse on the generator field voltage 165

List of Tables

2.1 Conduction pattern of valves in a 6 pulse bridge 14

3.1 State Variables in Small Signal Models 59

5.1 Major Participations of Some Selected Modes in Multi-in-feed Test System 77
5.2 HVDC Interaction Modes of Test System 88
5.3 Electromechanical Modes of Test System 92

6.1 Some important modes of the test system 99
6.2 Participations and mode shapes of multi-mass speed terms in torsional modes 99
6.3 Participating modes in torsional interactions when controller gains are adjusted 100
6.4 Some important modes of the 39 bus test system used to analyze HVDC-generator-turbine torsional interactions 110

E.1 Some important modes of the test system 161

Chapter 1

Introduction

1.1 Background

Since the first commercial project in 1950s, the High Voltage Direct Current (HVDC) power transmission technology has been well developed over 50 years and widely used in modern power systems [1]. Line commutated converters and capacitor commutated converters are used in the HVDC systems. Although the capacitor commutated HVDC converters have gained some popularity recently for low power applications, the line commutated HVDC conveners are still leading in high power applications and can be found all around the world [2].

In HVDC systems, the AC power is converted into DC at a converter (Rectifier) and the power is transported in DC form to another converter at which the DC power is again converted into AC (Inverter). In line commutated converters, the smoothing reactors connected in series with the converters in the DC side are used to facilitate the AC to DC conversion of the thyristor based converters. A DC transmission line is used to transport the power from the rectifier to the inverter. In some cases, the rectifier and the inverter are placed at the same location and they are connected

together without having a DC line (back to back HVDC links). These back to back HVDC links are used either to connect two power systems with unequal operating frequencies or to enhance the stability of two power systems by effectively separating them.

The conversion process of the HVDC converters produces higher order harmonics in addition to the fundamental frequency component. For example, a 12 pulse HVDC converter generates $12n \pm 1$ (n=1,2,3...) harmonics in the AC side and $12n$ (n=1,2,3...) harmonics in the DC side. The harmonic filters are connected at the AC and DC sides to suppress the significant harmonic components.

This thesis is concerned with the interactions of the line commutated HVDC systems. The HVDC systems may interact with the other dynamic devices in the power systems. The HVDC controllers may affect the damping of the electromechanical modes [3]. Especially, the damping controllers can be incorporated with the HVDC controllers to damp out some troublesome electromechanical modes [4] [5] [6].

Some HVDC systems may interact with tightly coupled generator-turbine systems, which have torsional oscillations. These torsional interactions, which lie in the subsynchronous frequency range (0 to fundamental frequency), occur between the rectifier current/power controller and the multi-mass rotor-turbine systems of the generators [7]. In some practical cases, torsional instabilities caused by HVDC-generator-turbine interactions have been reported. In Square Butt project in North Dakota, The rectifier current controller interacted in an adverse way with a 11.5 Hz torsional mode of an adjacent generator-turbine unit [8]. Investigations carried out in the Coal Creek HVDC station, North Dakota have indicated some possibility of a torsional instability at a 19 Hz torsional mode associated with a nearby generator-turbine unit [9]. Although, the HVDC controllers may cause torsional instabilities

in generator-turbine units, they can also be utilized to improve the damping of the torsional modes. A subsynchronous damping controller (SSDC) can be included in the rectifier current/power controller as an auxiliary controller [10, 11, 12, 13]. SSDC consists of gain blocks, washout filters and lead-lag blocks to appropriately damp out one or more troublesome torsional modes.

Multi-HVDC systems, in which more than one HVDC system is connected to the power system within close proximity, can also be found in modern power systems [14]. When more than one HVDC inverters are connected to a power system within close proximity, they are considered as "multi-in-feed HVDC systems". In multi-in-feed HVDC systems, the HVDC links may interact with each other as well as with other dynamic devices in the power system. Sufficient attention has not been paid in the literature to the interactions among the HVDC links in multi-in-feed HVDC environments.

It is important to identify these multi-HVDC and HVDC-generator-turbine interactions accurately for stability analysis and controller design. Electro-Magnetic Transient (EMT) type time domain simulations, transient stability analysis techniques and small signal stability assessment are the most common techniques employed for the stability assessment. EMT type simulations use detailed models and therefore, give more accurate results. The major limitations in EMT type simulations are the size of the system and the simulation time. Only small power systems can be modeled in this type of programs and the simulation time increases as the size of the system increases. These limitations are overcome in transient stability simulations by using simplified models. The interactions in HVDC systems can be analyzed qualitatively, using the time domain responses obtained from these EMT and transient stability simulation techniques. However, some of the modes in the system may not be ob-

servable in the responses. Although, the modes are observable, the contributions for these modes cannot be identified accurately using the responses. The interactions at a particular steady state operating point of the power system can be analyzed quantitatively in the frequency domain using small signal stability assessment techniques. The contributions towards the interactions are identified accurately using eigenvalue analysis techniques [15]. Furthermore, this technique can be applied for large systems efficiently [16].

Small signal stability is concerned with the ability of power systems to maintain synchronism under small disturbances [17]. The disturbances are considered to be sufficiently small that the linearization of the system's nonlinear behavior is permissible. The nonlinear behavior of the dynamic devices of the power system is first linearized at a particular steady state operating point. The linear state space model of the power system is then obtained by combining the linearized model of the dynamic devices together. The small signal stability of the power system is determined from the eigenvalues of the system matrix of the state space model using Lyapunov's stability criteria [18].

In order to apply in large power systems, some simplification techniques are used in conventional small signal stability programs. The objective of these programs is to analyze the low frequency electromechanical oscillations ($<$ 3Hz) of power systems. Therefore, the electrical network is modeled using algebraic equations (admittance matrix), ignoring high frequency network transients. Furthermore, the generator stator dynamics are also ignored to be consistent with the algebraic network model [15]. The admittance matrix representation of the AC network helps to reduce the size of the system matrix dramatically. SSAT (DSA Power Tools) [19], PacDyn [20], NEVA (PSS/E) and DIgSILENT PowerFactory are some of the commercial software

packages, which can be employed to analyze the electromechanical oscillations of large power systems.

In order to accurately analyze the interactions related to HVDC and flexible AC transmission system (FACTS) devices and the torsional interactions, the conventional small signal stability assessment technique has to be modified. These interactions may contain frequencies up to 200Hz [21] and therefore, the above approximations are not valid. The AC network dynamics have to be included and the generators are required to be modeled including stator winding dynamics. The network components can be modeled using the dynamic phasor model [22, 23, 24]. The higher order harmonics in the HVDC systems can still be ignored since they are well above the frequencies of interest. For example, the lowest AC side harmonic in a 60Hz, 12 pulse converter is 660Hz and there is no influence of this harmonic on the low frequency interactions (up to 200Hz).

Inclusion of network dynamics and stator dynamics of generators increases the number of state variables and hence the size of the system matrix. Therefore, it is impractical to model all the network dynamics of large power systems. Therefore, the HVDC interaction studies reported in the literature [5, 6, 21, 25, 26] have been limited to very small test systems such as CIGRE benchmark HVDC test system [27]. When high frequency interactions need to be studied, only a small portion of the power system is modeled including network dynamics and the rest of the system is represented using simplified models such as an infinite bus behind the Thevenin's impedance. Some locally spread interactions can be analyzed using these simplified models. However, the effect of these interactions on the rest of the system cannot be investigated. Especially, when designing controllers to control some high frequency interactions, the effect of them on widely spread interactions such as inter-area modes

cannot be analyzed using these simplified models.

In summary, the HVDC systems may interact with the other dynamic devices of power systems. The small signal stability assessment can be used to analyze the interactions quantitatively if it is modified appropriately to be accurate up to around 200Hz frequency oscillations in the power systems. However, the capabilities of the small signal stability assessment in analyzing HVDC interactions have not been well explored in the literature.

1.2 Thesis Objectives

The main objective of this research is to analyze the HVDC interactions in power systems using small signal stability assessment techniques. The following goals were set to achieve the main objective.

The nonlinear devices in power systems such as HVDC systems, generators and AC network are linearized at a particular steady state operating point such that the linear models are accurate for the desired frequency range. The linearized models are presented as current injection models, which can be easily combined with the conventional small signal stability models of other devices. A linearized model of an HVDC system including converter models, rectifier and inverter controllers, DC transmission system and Phase Lock Oscillators (PLOs) are developed using the knowledge provided in [25] and [21]. The dynamic phasor model [22][23][24] are used to model the AC network. Transmission lines, transformers, static loads and AC filters are included in the AC network model. The generators are modeled including their stator dynamics. The modeling adequacy in the range of frequencies of interest are evaluated using the time domain simulations and the frequency domain analysis.

The ultimate goal of this research is to analyze HVDC interactions in large power

systems. For this, a single platform, which can be employed to analyze conventional electromechanical oscillations as well as high frequency interactions is proposed in this thesis. The areas of the network, which consist of dynamic devices causing high frequency oscillations, are modeled including network dynamics and the rest of the network is modeled using the power frequency admittance matrix. The linearized models of the dynamic devices are combined with the dynamic network models using Kirchhoff's laws. The resultant linearized models of the dynamic network areas are combined with the admittance matrix of the rest of the network using current injection models. The model is referred to in this thesis as "hybrid AC network model" or "hybrid small signal model". The accuracy of the proposed model is evaluated using detailed models and time domain simulations.

The HVDC interactions are analyzed in the frequency domain using developed models. The interactions between the HVDC terminals in multi-in-feed HVDC power systems, the HVDC-generator electromechanical interactions and the HVDC-generator-turbine torsional interactions are mainly focused on the studies. The methodology can be directly used for the interaction studies of the other dynamic devices such as FACTS devices. However, these devices are not included in the analysis carried out in this thesis.

1.3 Thesis Outline

The linearized models of the power systems are presented in **Chapter 2**. The linearized model of an HVDC system and its accuracy is extensively discussed. The model is validated up to 200Hz using frequency response analysis. The linearized models of generators with and without stator dynamics are briefly discussed in this chapter and the models are given in Appendix C. The conventional model of the AC

network (admittance matrix representation) and the dynamic phasor model are presented and the accuracy of these two models in analyzing high frequency HVDC interactions are evaluated using time domain simulations obtained for a small multi-in-feed HVDC test system. The detailed EMT simulations obtained using PSCAD/EMTDC [28] are used as a benchmark for the comparisons.

The proposed hybrid AC network model is presented in **Chapter 3**. The formation of the dynamic network areas and combination of the dynamic network areas with the rest of the system (admittance matrix model) are discussed using simple examples. The model is tested using a modified version of the IEEE New England 39 bus test system [29]. Two generators of the test system are replaced with two HVDC in-feeds and the neighborhood of these HVDC in-feeds are modeled including the network dynamics. The performance of the hybrid model is compared against an EMT model, the conventional small signal model and the small signal model including the dynamics of the entire AC network.

The small signal stability assessment of power system is briefly summarized in **Chapter 4**. The modes in the power systems are identified using eigenvalues of the linearized model and the modal characteristics are given by the properties of the eigenvalues and eigenvectors.

The HVDC interactions of the power systems are analyzed in **Chapter 5** using the small signal stability assessment. This includes the multi-in-feed HVDC interactions and the HVDC-generator electromechanical interactions. The interactions are first analyzed for a small multi-in-feed HVDC test system (Case Study-1) using a small signal model including the dynamics of the entire AC network. The analysis is then extended to the IEEE New England 39 bus test system in Case Study-2 using the proposed hybrid small signal model. The detailed model including the dynamics of

the entire AC network is also used to validate the results of the hybrid model.

The HVDC-generator-turbine torsional interactions are discussed in **Chapter 6**. The studies are carried out using a simple test system to show that a small signal stability model with the AC network dynamics modeled is adequate to analyze the interactions. Furthermore, the hybrid model is used to analyze torsional interactions in the IEEE New England 39 bus test system. The possibilities of designing subsynchronous damping controllers for the HVDC systems are briefly discussed using small signal stability assessment.

Chapter 7 presents the conclusions of the research and the recommended future studies.

Chapter 2

Linearized Models of Power Systems

2.1 Introduction

In small signal stability assessment, nonlinear behavior of dynamic devices is first linearized at a particular steady state operating point. It is assumed that the power system is balanced among the three phases and therefore, only the positive sequence relationships are considered. This helps to reduce the size of the equivalent linear model significantly.

In general, linearization of a nonlinear function is carried out by expanding it into a Taylor series at the nominal operating point. Only the first order terms of the expansion are considered assuming that the higher order changes are negligible. Therefore, the method is applied to smooth nonlinearities with small deviations from the operating point.

Consider the nonlinear function given in Equation (2.1). The variables $x_1, x_2, .., x_n$ may be state variables, inputs, outputs or their derivatives.

$$y = f(x_1, x_2, .., x_n) \tag{2.1}$$

At the steady state operating point at which the linearization is done, the value of the function is given by,

$$y^0 = f(x_1^0, x_2^0, .., x_n^0). \tag{2.2}$$

$x_1^0, x_2^0, .., x_n^0$ are the values of variables at the steady state operating point.

The change in the value of the function from the steady state, i.e. $y - y^0$, can be obtained using the first order Taylor series expansion as given in Equation 2.3.

$$\Delta y = \sum_{i=1:n} \left(\frac{\partial f}{\partial x_i}\right)^0 \Delta x_i \tag{2.3}$$

Where, $\left(\frac{\partial f}{\partial x_i}\right)^0$ is the steady state value of the partial derivative of the function with respect to the i^{th} variable. Δx_i is the change in i^{th} variable from the steady state operating point $(x_i - x_i^0)$.

This analytical technique is used to linearize nonlinear dynamic behaviors of the power system devices. The linearized models of the dynamic devices are combined together to obtain the linear state space model of the power system. It is important to evaluate the adequacy of the linearized models in small signal stability assessment, since there are approximations associated with each model. The linearization of some of the important dynamic devices and the adequacy of them are discussed in this chapter. This includes HVDC systems, synchronous generator-turbine units and their controllers, multi mass torsional turbine models and AC network models. The linear models are tested for the accuracy in the time domain as well as in the frequency domain by comparing with the detailed electromagnetic transient (EMT) simulations

obtained using PSCAD/EMTDC [28].

2.2 Linearized Model of an HVDC System

The linearization of HVDC converter models is challenging because of the non-linear switching and self commutation of the converter valves. For small changes, the linearization is carried out based on some approximations. The higher order harmonics generated in the conversion process are ignored and the fundamental AC components are assumed to be balanced among three phases. Some linearized models based on these assumptions can be found in [21, 25].

In [25], a linearized converter model has been derived from the well known HVDC steady state relationships. A more extensive approach has been employed in [21] to obtain the linearized model, where the frequency conversion process of the converters has been taken into account by frequency shifting the equations of the AC network dynamics. The HVDC converter model has been based on the frequency dependent model described in [30] and [31]. The original idea came from Larsen [32] and therefore, the equations are referred to as Larsen's equations. However, the frequency dependency could not be included in the small signal stability model. The changes in zero frequency component in DC side and the fundamental frequency component in the AC side have been considered. The AC side equations were frequency shifted by $\pm$ fundamental frequency to combine the AC side and DC side equations. Preliminary studies done on the CIGRE benchmark HVDC test system [27], have shown that the above two methods give similar results as far as the converter operation is concerned. Neither of the above references include the inverter firing controllers in the models.

In this thesis, a current injection model, which can be easily combined with the

other devices in power systems is proposed to be used as the linearized model of the HVDC system. The converter linearized model is obtained using the the fundamental frequency relationships derived from the converter switching waveforms. The HVDC system consists of the converter model, rectifier constant current controller (CC), inverter constant extinction angle controller (CEA) or constant voltage controller (VC) and the DC transmission system.

2.2.1 Converter Model

The 6-pulse Graetz bridge shown in Figure 2.1 is the basic building block of the HVDC converters. Six thyristor valves are connected between three phase AC side and DC side such that three valves (1,3 and 5) are in the upper limb and the other three valves (4,6 and 2) are in the lower limb. Each valve is fired at a particular instant. The firing instant with respect to a reference is called "firing angle" (α). The DC side voltage can be changed by changing the firing angle. When the next valve on the same limb is fired, the valve conducting will stop. There is a period in which the both of the valves conduct, before the first valve completely stops conduction. This period is called "commutation period" and the corresponding phase angle is referred to as "commutation angle" (μ). The conduction pattern of the valves and the commutation periods are given in Table 2.1 for a cycle of the fundamental frequency. The angle is measured with respect to the phase-a terminal voltage.

Each valve in the bridge has a normal conduction period of 120° and two commutation periods ($2 \times \mu$) in each cycle. During the normal conduction of Valve-1 (phase-a), the upper DC side voltage with respective to the ground (V_{dc1}) and the AC side phase a current (i_a) are given by Equations (2.4) and (2.5) respectively. L_c is the leakage inductance of the converter transformer.

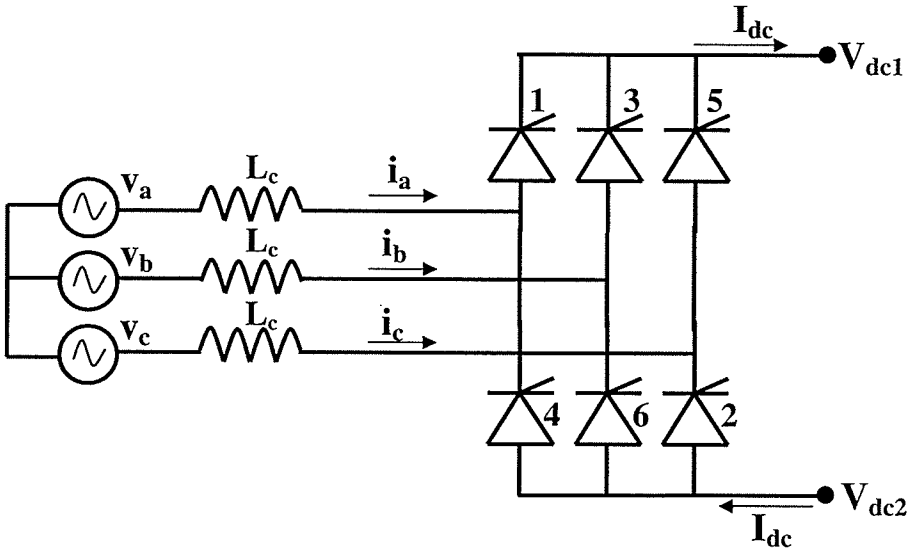

Figure 2.1: 6-pulse converter bridge

Table 2.1: Conduction pattern of valves in a 6 pulse bridge

Angle [°] (w.r.t. phase-a)		**Valves to be conducted**	**Comments**
From	**To**		
Upper limb			
0	$30+\alpha$	5	
$30+\alpha$	$30+\alpha+\mu$	5,1	commutation period
$30+\alpha+\mu$	$150+\alpha$	1	
$150+\alpha$	$150+\alpha+\mu$	1,3	commutation period
$150+\alpha+\mu$	$270+\alpha$	3	
$270+\alpha$	$270+\alpha+\mu$	3,5	commutation period
$270+\alpha+\mu$	360	5	
Lower limb			
0	$90+\alpha$	6	
$90+\alpha$	$90+\alpha+\mu$	6,2	commutation period
$90+\alpha+\mu$	$210+\alpha$	2	
$210+\alpha$	$210+\alpha+\mu$	2,4	commutation period
$210+\alpha+\mu$	$330+\alpha$	4	
$330+\alpha$	$330+\alpha+\mu$	4,6	commutation period
$330+\alpha+\mu$	360	6	

$$V_{dc1} = v_a - L_c \frac{dI_{dc}}{dt} \tag{2.4}$$

$$i_a = I_{dc} \tag{2.5}$$

During the commutation period (μ) of valves 1 (phase-a) and 3 (phase-b), the upper DC side voltage (V_{dc1}) and the AC side phase a current (i_a) are given by Equations (2.6) and (2.7) respectively.

$$V_{dc1} = \frac{v_a + v_b}{2} - \frac{L_c}{2}\frac{dI_{dc}}{dt} \tag{2.6}$$

$$\frac{di_a}{dt} = \frac{v_a - v_b}{2L_c} + \frac{1}{2}\frac{dI_{dc}}{dt} \tag{2.7}$$

If the derivatives of the DC current are ignored, the resultant upper limb DC side voltage (V_{dc1}), lower limb DC side voltage (V_{dc2}) and the AC side current in phase a (i_a) can be obtained as shown in Figure 2.2. The zero frequency component of the resultant DC side voltage ($V_{dc1} - V_{dc2}$) is given by Equation 2.8.

$$V_{dc} = \frac{3\sqrt{2}B}{\pi T} V_l \cos\alpha - \frac{3X_c B}{\pi} I_{dc} \tag{2.8}$$

AC currents and voltages are represented using phasors, which are defined by a magnitude and an angle with respect to a reference voltage waveform. The phasor of the reference voltage has zero angle. The phasor quantities can be transformed into two quadrature directions: one is along the reference voltage (real component) and the other one is 90^o ahead of the real component (imaginary component). These real and imaginary components are also used to represent the voltage and current

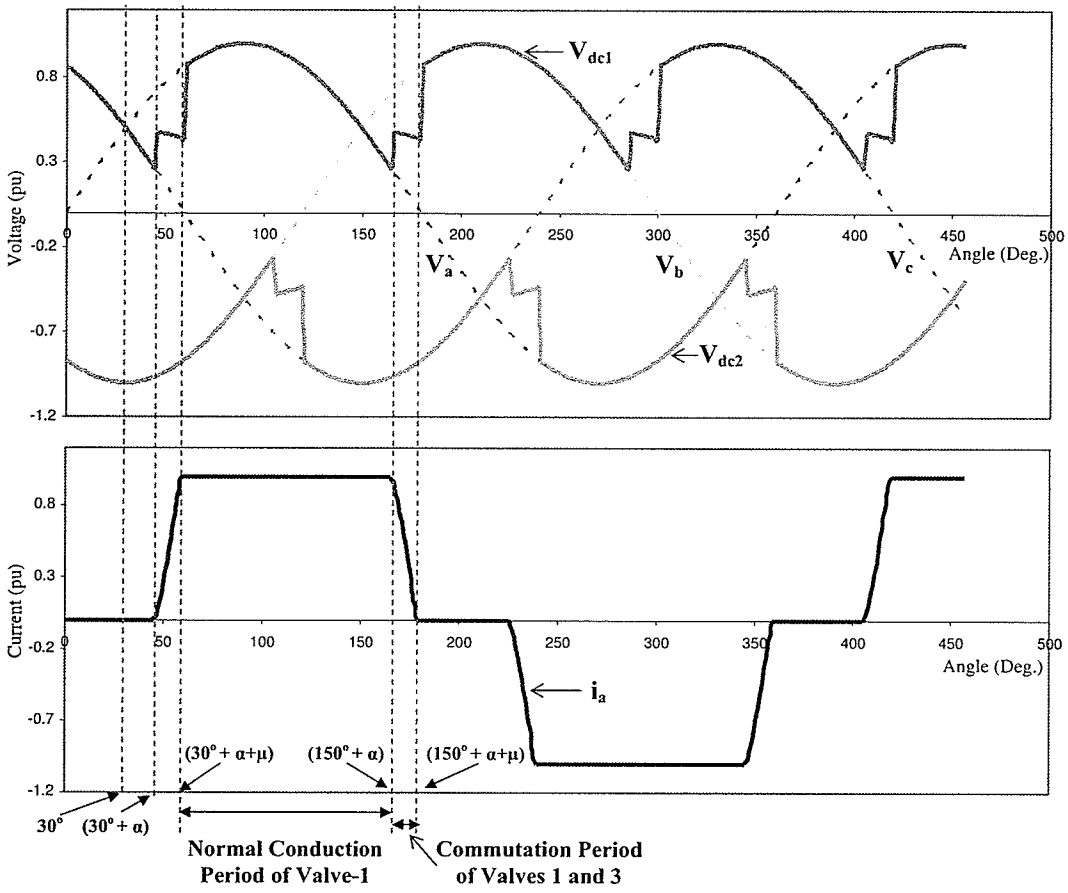

Figure 2.2: DC side voltages and AC side phase a current of a 6-pulse Bridge

phasors.

The fundamental frequency component of the converter AC current can be obtained from the current waveform shown in Figure 2.2 using Fourier series expansion. The fundamental component of the phase-a current is given by,

$$i_{a1} = A_{a1}\cos(\omega_0 t) + B_{a1}\sin(\omega_0 t) \tag{2.9}$$

where,

$$A_{a1} = \frac{\sqrt{2}BV_l}{\pi X_c T^2}\int_{\frac{\pi}{6}+\alpha}^{\frac{\pi}{6}+\alpha+\mu}[\cos(\alpha)-\cos(\theta-\frac{\pi}{6})]\cos(\theta)d\theta + \frac{2B}{\pi T}\int_{\frac{\pi}{6}+\alpha}^{\frac{5\pi}{6}+\alpha+\mu} I_{dc}\cos(\theta)d\theta$$
$$-\frac{\sqrt{2}BV_l}{\pi X_c T^2}\int_{\frac{5\pi}{6}+\alpha}^{\frac{5\pi}{6}+\alpha+\mu}[\cos(\alpha)-\cos(\theta-\frac{5\pi}{6})]\cos(\theta)d\theta$$

$$B_{a1} = \frac{\sqrt{2}BV_l}{\pi X_c T^2}\int_{\frac{\pi}{6}+\alpha}^{\frac{\pi}{6}+\alpha+\mu}[\cos(\alpha)-\cos(\theta-\frac{\pi}{6})]\sin(\theta)d\theta + \frac{2B}{\pi T}\int_{\frac{\pi}{6}+\alpha}^{\frac{5\pi}{6}+\alpha+\mu} I_{dc}\sin(\theta)d\theta$$
$$-\frac{\sqrt{2}BV_l}{\pi X_c T^2}\int_{\frac{5\pi}{6}+\alpha}^{\frac{5\pi}{6}+\alpha+\mu}[\cos(\alpha)-\cos(\theta-\frac{5\pi}{6})]\sin(\theta)d\theta$$

The real phasor component (I_R) and the imaginary phasor component (I_I) of the fundamental AC current can be obtained from,

$$\begin{bmatrix} I_R \\ I_I \end{bmatrix} = \begin{bmatrix} -\sin(\delta) & \cos(\delta) \\ \cos(\delta) & \sin(\delta) \end{bmatrix} \begin{bmatrix} A_{a1}/\sqrt{2} \\ B_{a1}/\sqrt{2} \end{bmatrix} \tag{2.10}$$

where, δ is the phase angle of the converter AC voltage with respect to the common reference.

The real and the imaginary components of the AC current can be simplified as given in Equations (2.11) and (2.12) respectively.

$$I_R = -\frac{\sqrt{3}BX_cI_{dc}^2V_R}{\pi V_l^2} + \frac{\sqrt{3}BM_1V_I}{2\pi X_cT^2} - \frac{\sqrt{6}BI_{dc}}{\pi T}\cos(\delta-\alpha-\mu) \tag{2.11}$$

$$I_I = -\frac{\sqrt{3}BM_1V_R}{2\pi X_cT^2} - \frac{\sqrt{3}BX_cI_{dc}^2V_I}{\pi V_l^2} - \frac{\sqrt{6}BI_{dc}}{\pi T}\sin(\delta-\alpha-\mu) \tag{2.12}$$

In the above equations,

$M1 = (1 - \cos(\mu))\sin(2\alpha + \mu) + \sin(\mu) - \mu$

B - Number of 6 pulse bridges

T - Converter transformer turns ratio (AC/DC)

α - Converter firing angle

μ - commutation angle

X_c - Transformer reactance referred to DC side

V_l - L-L voltage magnitude of the AC bus

δ - angle of the AC bus voltage with respect to the common reference

V_R - real component of the AC bus voltage

V_I - imaginary component of the AC bus voltage

The higher order harmonics of the DC side voltage and the AC side currents are neglected since they are well above the range of frequency of interest (0-200Hz). For example, in a commonly used 12 pulse bridge, the DC side voltage produces 12^{th} harmonic next to the DC component [33]. In the AC side, 11^{th} and 13^{th} harmonics are next to the fundamental component [33]. These frequencies are well above 200Hz.

In the above steady state relationships, the derivatives of the DC current are ignored. In the small signal stability model, the derivative part is considered separately with the DC transmission system. This is explained in Section 2.2.2.

The DC side voltage and real and imaginary components of the AC current (Equations 2.8, 2.11 and 2.12) depend on the commutation angle (μ). If it is assumed that the change in the DC current during the commutation period is negligible, the commutation angle can be obtained as a function of DC side current, AC side voltage and firing angle as given in Equation (2.13). The commutation period is usually small ($< 30^o$) and the DC current cannot be changed very quickly because of the high

smoothing and line inductance. Therefore, this assumption is fairly accurate.

$$\mu = \cos^{-1}(\cos\alpha - \frac{\sqrt{2}X_cTI_{dc}}{V_l}) - \alpha \tag{2.13}$$

The fundamental frequency relationships (Equations 2.8, 2.11 and 2.12) derived from the converter switching waveforms are used to obtain the linearized model. The commutation angle appeared in these relationships is replaced by Equation (2.13). The converter linearized relationships can be defined using four inputs (real component and imaginary component of AC side voltage, DC side current and firing angle) and three outputs (real component and imaginary component of AC side current and DC side voltage). The changes of the outputs for small changes in the inputs are given by Equation (2.14).

$$\begin{bmatrix} \Delta I_R \\ \Delta I_I \\ \Delta V_{dc} \end{bmatrix} = \begin{bmatrix} Ka & Kb & Kc & Kd \\ Ke & Kf & Kg & Kh \\ Ki & Kj & Kk & Kl \end{bmatrix} \begin{bmatrix} \Delta V_R \\ \Delta V_I \\ \Delta I_{dc} \\ \Delta\alpha \end{bmatrix} \tag{2.14}$$

The parameters of the linearized model (Equation 2.14) can be obtained using the following equations at a particular steady state condition.

$$Ka = -\frac{\sqrt{3}BX_cI_{dc}^2}{\pi V_l^2} - \frac{\sqrt{6}BI_{dc}V_I\sin(\delta-\alpha-\mu)}{\pi TV_l^2}$$

$$Kb = \frac{\sqrt{3}BM1}{2\pi X_cT^2} + \frac{\sqrt{6}BI_{dc}V_R\sin(\delta-\alpha-\mu)}{\pi TV_l^2}$$

$$Kc = -\frac{\sqrt{6}B\cos(\delta-\alpha-\mu)}{\pi T}$$

$$Kd = -\frac{\sqrt{6}BI_{dc}\sin(\alpha)\sin(\delta-\alpha-\mu/2)}{\pi T\sin(\alpha+\mu/2)}$$

$$Ke = -\frac{\sqrt{3}BM1}{2\pi X_cT^2} + \frac{\sqrt{6}BI_{dc}V_I\cos(\delta-\alpha-\mu)}{\pi TV_l^2}$$

$$Kf = -\frac{\sqrt{3}BX_cI_{dc}^2}{\pi V_l^2} - \frac{\sqrt{6}BI_{dc}V_R\cos(\delta-\alpha-\mu)}{\pi TV_l^2}$$

$$Kg = -\frac{\sqrt{6}B\sin(\delta-\alpha-\mu)}{\pi T}$$

$$Kh = \frac{\sqrt{6}BI_{dc}\sin(\alpha)\cos(\delta-\alpha-\mu/2)}{\pi T\sin(\alpha+\mu/2)}$$

$$Ki = \frac{3\sqrt{2}BV_R\cos(\alpha)}{\pi TV_l}$$

$$Kj = \frac{3\sqrt{2}BV_I\cos(\alpha)}{\pi TV_l}$$

$$Kk = -\frac{3X_cB}{\pi}$$

$$Kl = -\frac{3\sqrt{(2)}BV_l\sin(\alpha)}{\pi T}$$

This model is similar to the one given in [21], except, the real and imaginary components are used as the variables to be consistent with the common approach of linearized power systems, instead of positive and negative sequences. Note that the signs of Ki, Kj, Kk and Kl should be inverted in order to represent a positive voltage pole inverter.

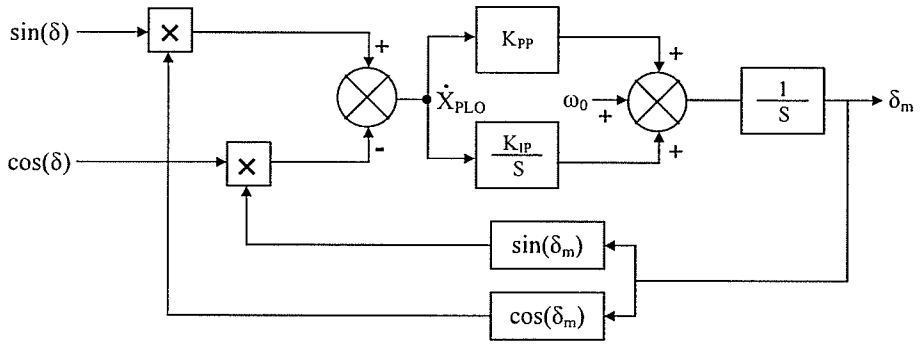

Figure 2.3: Phase Locked Oscillator

Phase Locked Oscillator

Firing control of valves is one of the major parts in HVDC converters. The firing instant of a value is determined based on the phase of the AC voltage. Phase Locked Oscillators (PLO) based on the phase vector techniques are used to determine the AC voltage phase in HVDC converters [34]. A simplified version of PLO is shown in Figure 2.3. The simplification is carried out based on the assumption that the three phases are balanced. An error signal $[\sin(\delta - \delta_m)]$ of the actual phase angle (δ) and the calculated phase angle (δ_m) is given to a P-I controller, in order to obtain the angular frequency error. The frequency error is added to the nominal frequency (ω_0) and the resultant frequency is integrated to obtain the phase angle.

The actual phase angle can be obtained in terms of V_R and V_I (note that, $\tan(\delta) = V_I/V_R$). Two state variables: X_{PLO} and δ_m are used to represent the P-I controller and the integrator respectively. The small signal PLO model is given in Equation 2.15.

$$\begin{bmatrix} \Delta\dot{X}_{PLO} \\ \Delta\dot{\delta}_m \end{bmatrix} = \begin{bmatrix} 0 & -1 \\ K_{IP} & -K_{PP} \end{bmatrix} \begin{bmatrix} \Delta X_{PLO} \\ \Delta\delta_m \end{bmatrix} + \begin{bmatrix} -\frac{V_I}{V_t^2} & \frac{V_R}{V_t^2} \\ -\frac{K_{PP}V_I}{V_t^2} & \frac{K_{PP}V_R}{V_t^2} \end{bmatrix} \begin{bmatrix} \Delta V_R \\ \Delta V_I \end{bmatrix} \quad (2.15)$$

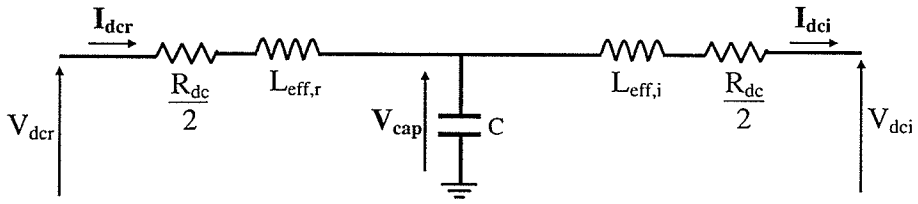

Figure 2.4: DC transmission system

The phase angle (δ_m) determined by the PLO is added to the desired firing angle (α) to obtain the firing instant.

2.2.2 DC Transmission System

A T-model is used to represent the DC system as shown in Figure 2.4. The DC side inductance and resistance are distributed into two series inductor-resistor units and the line to ground capacitance is concentrated at the middle.

In the steady state relationships, the time derivative terms of the DC current are ignored. In the small signal model, these derivative parts are included by considering the average effect of the converter transformer leakage reactance. It is shown in Equations (2.4) and (2.6), that the contribution of the transformer leakage inductance is different during the normal conduction and commutation periods. Therefore, an average inductance is obtained and it is added to the half of the DC line inductance to obtain the effective inductance [35] given in Equation (2.16).

$$L_{eff} = \frac{L_{dc}}{2} + B(2 - \frac{3\mu}{2\pi})L_c \tag{2.16}$$

L_{dc} is the DC side total inductance and L_c is the transformer leakage inductance. The effective inductances in the rectifier side and the inverter side are different because

the transformer leakage inductances are different.

The dynamics of the DC line are modeled using three state variables, namely, the rectifier side DC current (ΔI_{dcr}), the inverter side DC current (ΔI_{dci}) and the mid-point capacitor voltage (ΔV_{cap}). The linearized model of the DC line is given in Equation (2.17).

$$\begin{bmatrix} \Delta\dot{I}_{dcr} \\ \Delta\dot{I}_{dci} \\ \Delta\dot{V}_{cap} \end{bmatrix} = \begin{bmatrix} -\frac{R_{dc}}{2L_{eff,r}} & 0 & -\frac{1}{L_{eff,r}} \\ 0 & -\frac{R_{dc}}{2L_{eff,i}} & \frac{1}{L_{eff,i}} \\ \frac{1}{C} & -\frac{1}{C} & 0 \end{bmatrix} \begin{bmatrix} \Delta I_{dcr} \\ \Delta I_{dci} \\ \Delta V_{cap} \end{bmatrix} + \begin{bmatrix} \frac{1}{L_{eff,r}} & 0 \\ 0 & -\frac{1}{L_{eff,i}} \\ 0 & 0 \end{bmatrix} \begin{bmatrix} \Delta V_{dcr} \\ \Delta V_{dci} \end{bmatrix} \quad (2.17)$$

Where, V_{dcr} and V_{dci} are the rectifier and the inverter side DC voltages. $L_{eff,r}$ and $L_{eff,i}$ are the rectifier and the inverter side effective inductances. R_{dc} and C are the DC resistance and the capacitance respectively.

2.2.3 HVDC Controllers

In small signal stability, only the active controllers under nominal conditions are considered. Usually, rectifier constant current controller (CC) and inverter constant extinction angle controller (CEA) or inverter constant voltage controller (VC) are included. Other auxiliary controllers such as damping controllers can also be included.

In this thesis, two different operating points are considered as shown in Figure 2.5. The rectifier current controller and the inverter extinction angle controller are the active controllers in the operating point shown in Figure 2.5(a). The rectifier current controller and the inverter voltage controller are the active controllers in the operating point shown in Figure 2.5(b). Small Signal models of the individual controllers are

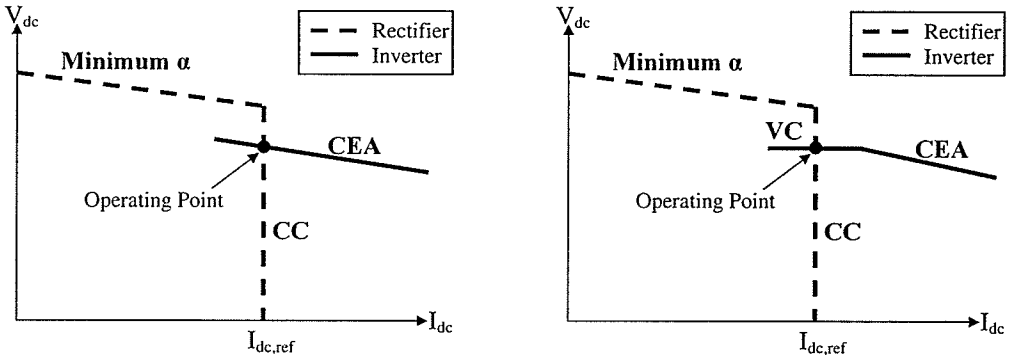

(a) Operating point at rectifier current control and inverter extinction angle control

(b) Operating point at rectifier current control and inverter voltage control

Figure 2.5: HVDC operating points at nominal conditions

described in the following sections.

Rectifier Constant Current Control

The PI controller shown in Figure 2.6(a) is used to control the firing angle of the rectifier. The difference between the measured DC current and the desired current is used as the input. One state variable ($X_{\alpha r}$) is used to represent the integral controller. The state space equation and the change in required firing angle ($\Delta\alpha r^*$) are given by Equations (2.18) and (2.19) respectively.

$$\Delta\dot{X}_{\alpha r} = \Delta I_{dcr} - \Delta I_{dc,order} \tag{2.18}$$

$$\Delta\alpha r^* = K_{Ir}\Delta X_{\alpha r} + K_{Pr}\Delta I_{dcr} - K_{Pr}\Delta I_{dc,order} \tag{2.19}$$

K_{Pr} and K_{Ir} are the proportional and integral gains respectively and $I_{dc,order}$ is the rectifier current reference.

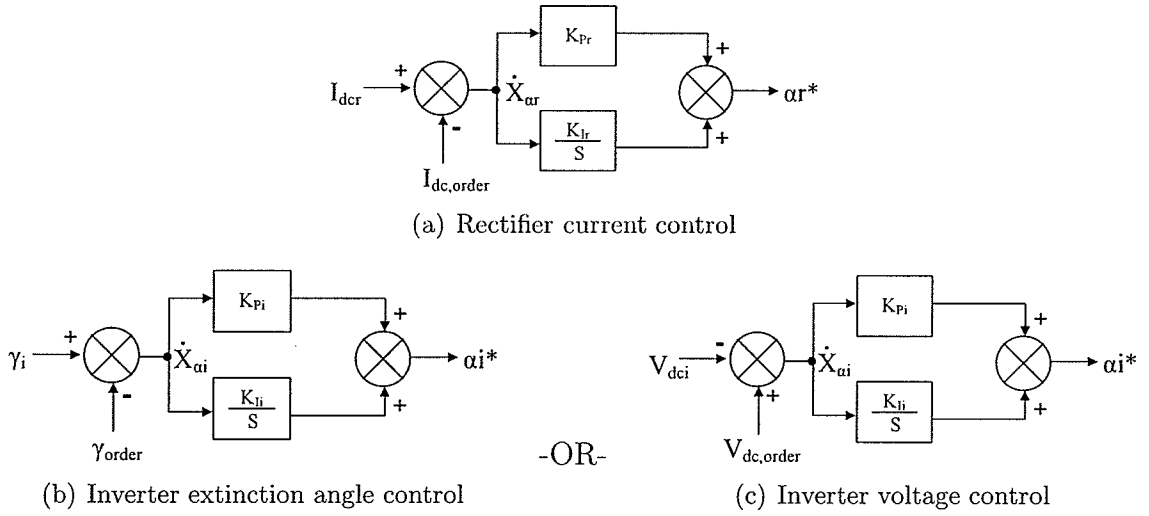

(a) Rectifier current control

(b) Inverter extinction angle control

(c) Inverter voltage control

Figure 2.6: HVDC control schemes

Inverter Constant Extinction Angle Control

The PI controller shown in Figure 2.6(b) is used to control the firing angle of the inverter. One state variable ($X_{\alpha i}$) is used to represent the integral controller. The difference between the measured extinction angle and the desired angle is used as the input. The measured extinction angle is equal to ($\pi - \alpha - \mu$). Therefore, the linearized model of the controller can be obtained as in Equations (2.20) and (2.21).

$$\Delta\dot{X}_{\alpha i} = -\Delta\alpha i^* - \Delta\mu_i - \Delta\gamma_{order} \tag{2.20}$$

$$(1 + K_{Pi})\Delta\alpha i^* = K_{Ii}\Delta X_{\alpha i} - K_{Pi}\Delta\mu_i - K_{Pi}\Delta\gamma_{order} \tag{2.21}$$

As shown in Equation 2.13, the commutation angle (μ) is a function of the AC side voltages, the inverter DC current and the firing angle. Therefore, the change in commutation angle ($\Delta\mu$) can be replaced by those variables. The resultant linearized model of the controller is given in Equations (2.22) and (2.23).

$$\Delta\dot{X}_{\alpha i} = k_{1a}\Delta X_{\alpha i} + k_{2a}\Delta I_{dci} + k_{3a}\Delta V_{Ri} + k_{4a}\Delta V_{Ii} + k_{5a}\Delta\gamma_{order} \quad (2.22)$$

$$\Delta\alpha i^* = K_{Pi}k_{1a}\Delta X_{\alpha i} + K_{Pi}k_{2a}\Delta I_{dci} + K_{Pi}k_{3a}\Delta V_{Ri} - \frac{\sin(\alpha+\mu)}{\sin(\alpha)}k_{4a}\Delta V_{Ii} + K_{Pi}k_{5a}\Delta\gamma_{order} \quad (2.23)$$

In the above Equations,

$$k_{1a} = -\frac{K_{Ii}}{\sin(\alpha_i) + sin(\alpha_i+\mu_i)}$$

$$k_{2a} = -\frac{\sqrt{2}TX_c}{V_{li}(K_{Pi}\sin(\alpha_i) + sin(\alpha_i+\mu_i))}$$

$$k_{3a} = \frac{\sqrt{2}TX_cI_{dci}V_{Ri}}{V_{li}^3(K_{Pi}\sin(\alpha_i) + sin(\alpha_i+\mu_i))}$$

$$k_{4a} = \frac{\sqrt{2}TX_cI_{dci}V_{Ii}}{V_{li}^3(K_{Pi}\sin(\alpha_i) + sin(\alpha_i+\mu_i))}$$

$$k_{5a} = -\frac{sin(\alpha_i+\mu_i)}{K_{Pi}\sin(\alpha_i) + sin(\alpha_i+\mu_i)}$$

Inverter Constant Voltage Control

The PI controller shown in Figure 2.6(c) is used to control the firing angle of the inverter. Since only one of the excitation angle controller or the voltage controller is active, the same notation of the state variable used in the excitation controller ($X_{\alpha i}$) is used to represent the integral controller. The difference between the measured inverter side DC voltage and the desired DC voltage is used as the input. The inverter side DC voltage is a function of the AC side voltages, the inverter DC current and the firing angle as given in the linearized converter model in Equation (2.14). Therefore, ΔV_{dci} terms in the controller can be replaced by the corresponding terms of Equation (2.14). The resultant linearized model is given in Equations (2.24) and (2.25).

$$\Delta\dot{X}_{\alpha i} = k_{1b}\Delta X_{\alpha i} + k_{2b}\Delta I_{dci} + k_{3b}\Delta V_{Ri} + k_{4b}\Delta V_{Ii} + k_{5b}\Delta V_{dc,order} \tag{2.24}$$

$$\Delta\alpha i^* = -\frac{k_{1b}}{Kl_i}\Delta X_{\alpha i} + K_{Pi}k_{2b}\Delta I_{dci} + K_{Pi}k_{3b}\Delta V_{Ri} + K_{Pi}k_{4b}\Delta V_{Ii} + K_{Pi}k_{5b}\Delta V_{dc,order} \tag{2.25}$$

In the above Equations,

$$k_{1b} = -\frac{K_{Ii}Kl_i}{1 + K_{Pi}Kl_i}$$

$$k_{2b} = -\frac{Kk_i}{1 + K_{Pi}Kl_i}$$

$$k_{3b} = -\frac{Ki_i}{1 + K_{Pi}Kl_i}$$

$$k_{4b} = -\frac{Kj_i}{1 + K_{Pi}Kl_i}$$

$$k_{5b} = \frac{1}{1 + K_{Pi}Kl_i}$$

Ki_i, Kj_i, Kk_i and Kl_i can be obtained from the linearized converter model given in (2.14) by substituting the values corresponding to the inverter. Note that, suffix "i" is used to represent the inverter.

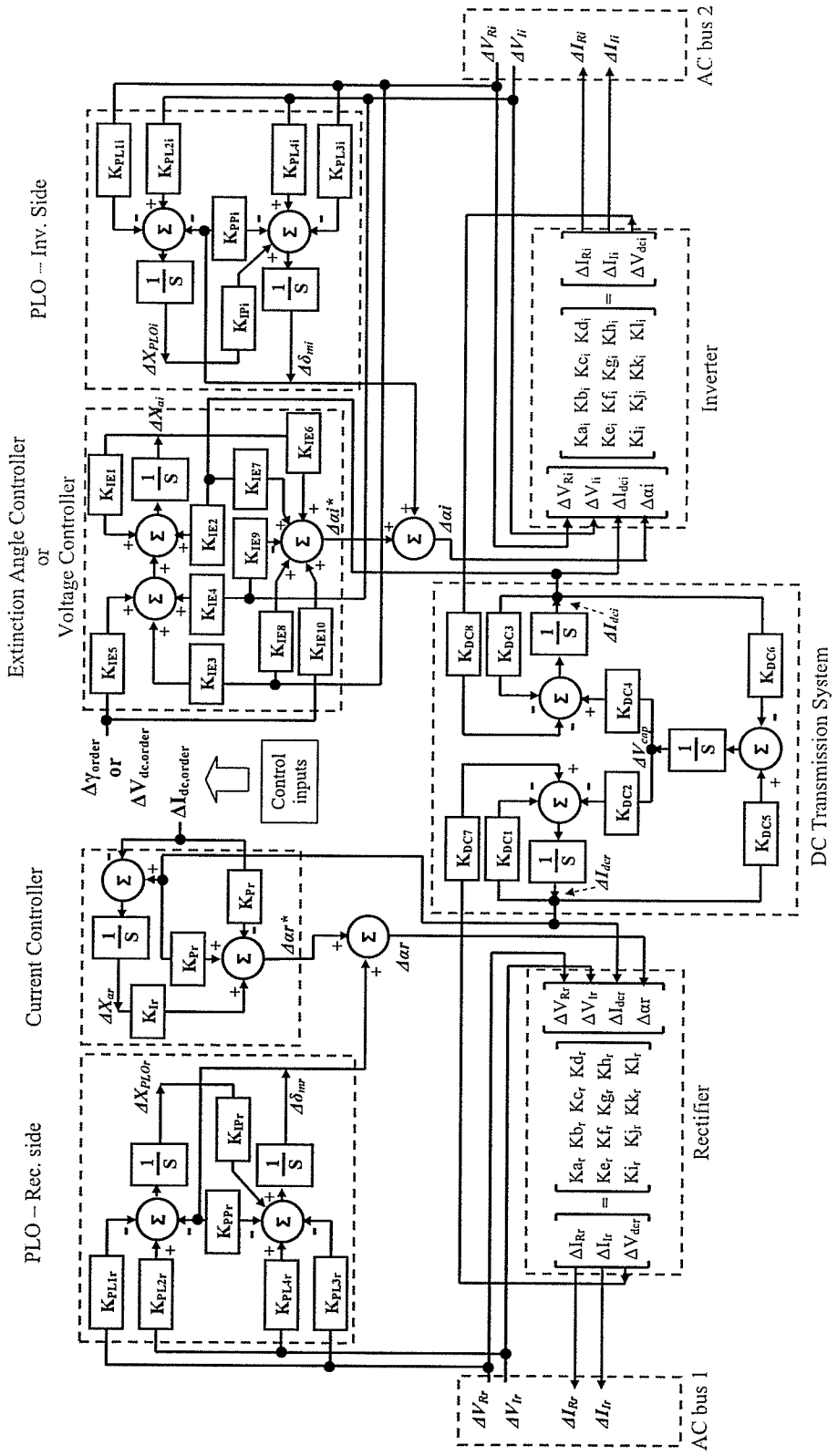

Figure 2.7: Linearized model of HVDC system

2.2.4 State Space Model of HVDC System

The linearized models of the subsystems are combined together to obtain the state space model of the HVDC system. This combination process is illustrated in the control block diagram shown in Figure 2.7.

The change in desired firing angle ($\Delta\alpha r^*$) given by the rectifier current controller (Equation (2.19)) is added to the change in phase angle ($\Delta\delta_{mr}$) given by the PLO model (Equation (2.15)) to obtain the change in firing instant of the rectifier ($\Delta\alpha r$) as shown in Equation (2.26). Similarly, for the inverter, the change in desired firing angle ($\Delta\alpha i^*$) given by the extinction angle controller (Equation (2.23)) or the voltage controller (Equation (2.25)) is added to the change in phase angle ($\Delta\delta_{mi}$) to obtain the change in firing instant ($\Delta\alpha i$) as shown in Equation (2.27).

$$\Delta\alpha r = \Delta\alpha r^* + \Delta\delta_{mr} \tag{2.26}$$

$$\Delta\alpha i = \Delta\alpha i^* + \Delta\delta_{mi} \tag{2.27}$$

The firing instants are substituted in the rectifier and inverter models obtained using Equation (2.14). The changes in DC voltages given by the rectifier and inverter models are substituted in the DC transmission system (Equation (2.17)). This procedure results in the state space model of the HVDC system given in Equation (2.28). The overall system consists of nine state variables and two control inputs. The real and imaginary components of the rectifier and inverter output currents are obtained from Equation (2.29).

$$\Delta\dot{X}_H = \underset{(9\times9)}{A_H}\ (\Delta X_H) + \underset{(9\times2)}{B_H}\ (\Delta U_H) + \underset{(9\times4)}{E_H}\ (\Delta V_H) \tag{2.28}$$

$$\Delta I_H = \underset{(4\times9)}{C_H}\ (\Delta X_H) + \underset{(4\times2)}{D_H}\ (\Delta U_H) + \underset{(4\times4)}{Y_H}\ (\Delta V_H) \tag{2.29}$$

where, $\Delta X_H = \begin{bmatrix} \Delta X_{\alpha r} & \Delta X_{\alpha i} & \Delta I_{dcr} & \Delta I_{dci} & \Delta V_{cap} & \Delta X_{PLOr} & \Delta \delta_{mr} & \Delta X_{PLOi} & \Delta \delta_{mi} \end{bmatrix}^T$,

$\Delta U_H = \begin{bmatrix} \Delta I_{dc,order} \\ \Delta \gamma_{order} \end{bmatrix}$, $\Delta V_H = \begin{bmatrix} \Delta V_{Rr} \\ \Delta V_{Ir} \\ \Delta V_{Ri} \\ \Delta V_{Ii} \end{bmatrix}$ *and* $\Delta I_H = \begin{bmatrix} \Delta I_{Rr} \\ \Delta I_{Ir} \\ \Delta I_{Ri} \\ \Delta I_{Ii} \end{bmatrix}$.

A_H, B_H, E_H, C_H, D_H and Y_H matrices are obtained using the procedure described above.

2.2.5 Validation of Linearized HVDC Model

Since the system harmonics are ignored, the linearized HVDC model is accurate only up to a certain frequency. According to [21], the linearized model of a 12 pulse HVDC converter is accurate up to around 200Hz. A 60Hz, 12 pulse converter produces lowest harmonic of 660Hz in the AC side. In order to neglect the effect of this frequency component, the maximum frequency of the system should be less than the Nyquist frequency, which is the half of that frequency (330Hz). The practical limit is much lower than this value. Therefore, 0-200Hz is an acceptable frequency range. This frequency range (0-200Hz) is good enough to analyze the HVDC-generator interactions and the multi-HVDC interactions accurately. However, it is required to validate the linearized model for small disturbances within this frequency range. For this, an empirical approach is used in this thesis. The responses obtained from the linearized HVDC model and the detail PSCAD/EMTDC simulation models are compared in the time and frequency domains. The HVDC simulations produced by the electromagnetic transient program PSCAD/EMTDC have been validated using field tests

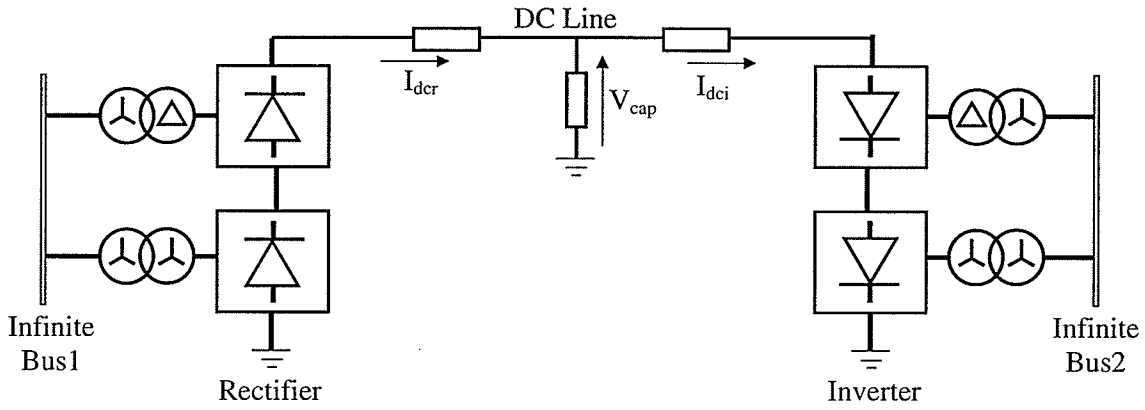

Figure 2.8: CIGRE benchmark test system with infinite AC buses

[36] and therefore those simulations can be used as a benchmark.

Frequency Response Analysis

For the simplicity, the HVDC system without controllers are considered in the analysis. Therefore, constant firing angle operation of the HVDC controllers is considered. The CIGRE benchmark HVDC test system [27] is used in the validations. The rectifier and inverter AC buses are modeled as infinite buses, in which the voltage can be controlled. The test system is shown in Figure 2.8 and the relevant data are given in Appendix A.

In the PSCAD/EMTDC simulation, a sinusoid in which the peak value is 5% of the nominal value is added to one of the inputs of the converters. The rectifier firing angle and the rectifier side AC voltage are considered as the inputs. The frequency of the sinusoid is changed from 0 to 200Hz in small steps and the relevant frequency components of the state variables and the outputs are scanned. The frequency responses between the inputs and the outputs/state variables obtained in this manner are compared with the responses of the linearized model. The frequency responses

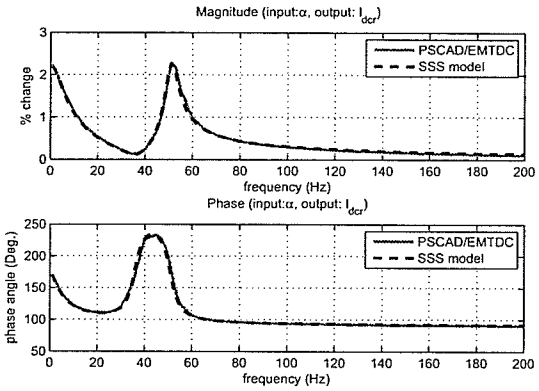

(a) **Input**: rectifier firing angle, **Output**: rectifier side DC current

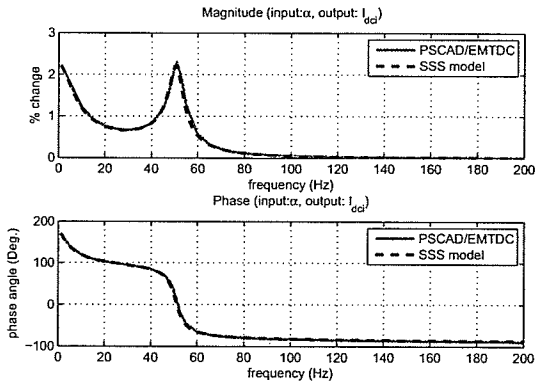

(b) **Input**: rectifier firing angle, **Output**: inverter side DC current

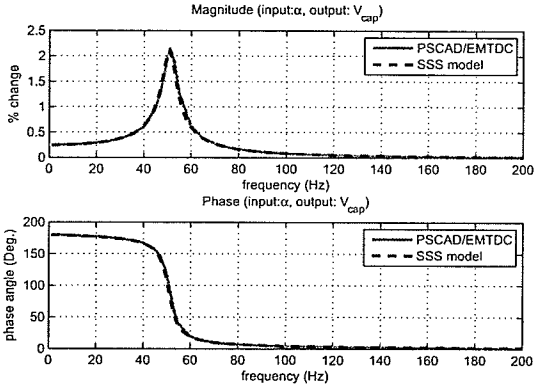

(c) **Input**: rectifier firing angle, **Output**: mid point DC capacitor voltage

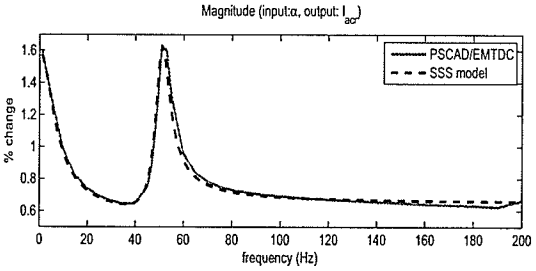

(d) **Input**: rectifier firing angle, **Output**: rectifier side AC current

Figure 2.9: Frequency response between rectifier firing angle and state variables/outputs (magnitude is given as % change for a 5% change in α_r)

between different inputs and outputs are discussed below.

- **Input at rectifier firing angle:**

  The rectifier firing angle is considered as the input. The frequency response (magnitude and phase plots) between the firing angle and the rectifier side DC current is shown in Figure 2.9(a). The frequency responses obtained at the inverter side DC current and the mid point capacitor voltage are shown in Figures 2.9(b) and 2.9(c) respectively. In these plots, the frequency is expressed with

respect to the DC side. The responses obtained from the small signal stability model and the PSCAD/EMTDC model match very well within the required frequency range. The magnitude plots show the DC line resonance frequency around 50 Hz. As the frequency increases, the gains between the input and the out puts decrease and they are small at 200Hz.

The frequency response (only the magnitude plot) at the AC side current is shown in Figure 2.9(d). The magnitude of the DC side frequency embedded in the AC current obtained from the PSCAD/EMTDC model is extracted using the fast fourier transform. The results are compared with those of small signal stability model. The close match in Figure 2.9(d) confirms that the DC to AC current transformation in the small signal model is accurately modeled within the frequency range.

- **Input at rectifier AC voltage:**

  In order to examine the accuracy of the AC to DC transformation of the linearized model, the rectifier AC voltage is considered as the input and the sinusoidal signal is added to the voltage magnitude. The frequency responses obtained at the rectifier side DC current, the inverter side DC current and the mid point capacitor voltage are shown in Figures 2.10(a), 2.10(b) and 2.10(c) respectively. The responses are similar to the responses obtained between the firing angle and the outputs in shape, but the gains are high in the responses between the AC voltage and the outputs.

  Furthermore, the comparisons of the responses between the AC voltage magnitude and AC current magnitude given in Fig. 2.10(d) also show a close match.

The frequency domain analysis shows that the Linearized small signal HVDC

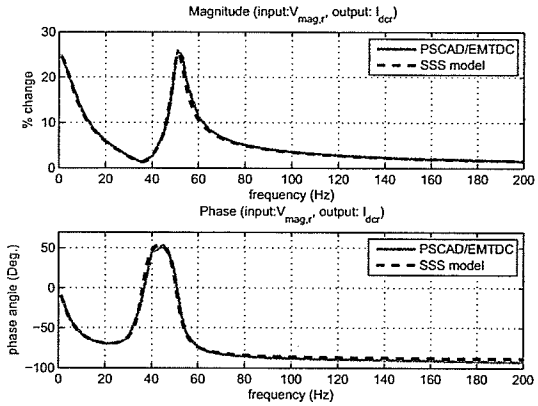

(a) **Input**: rectifier AC voltage, **Output**: rectifier side DC current

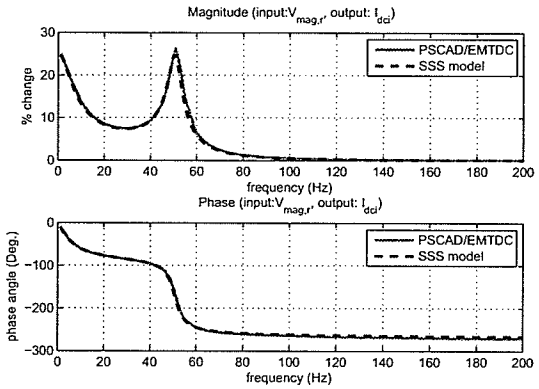

(b) **Input**: rectifier AC voltage, **Output**: inverter side DC current

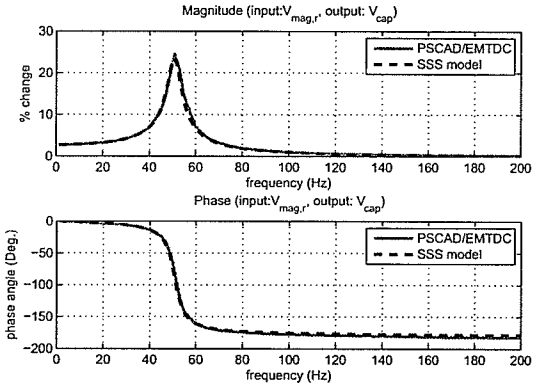

(c) **Input**: rectifier AC voltage, **Output**: mid point DC capacitor voltage

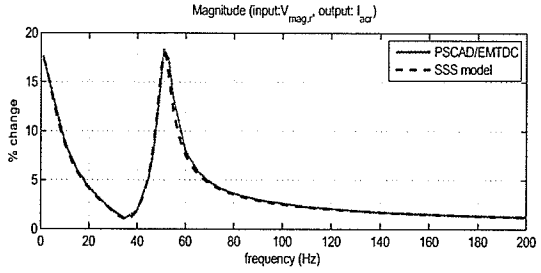

(d) **Input**: rectifier AC voltage, **Output**: rectifier side AC current

Figure 2.10: Frequency response between rectifier AC voltage and state variables/outputs (magnitude is given as % change for a 5% change in $V_{mag,r}$)

model gives very close results to those of the detailed electromagnetic transient simulation model within the frequency range of 0-200Hz.

Time Domain Simulations

The accuracy of the linearized HVDC model is further validated using time domain simulations. The test system shown in Figure 2.8 is used for the simulations. The rectifier constant current controller and the inverter constant extinction angle controller

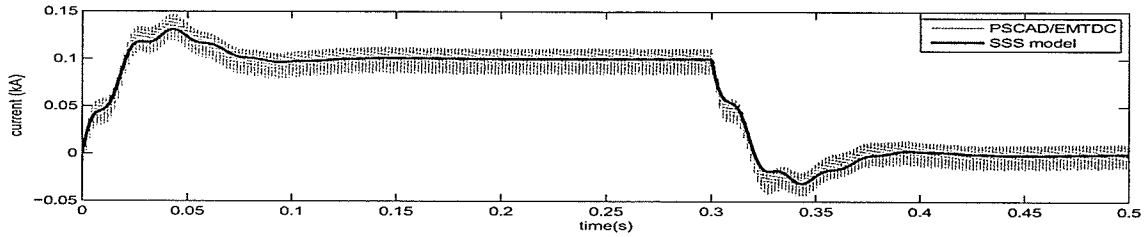

(a) Change in rectifier side DC current

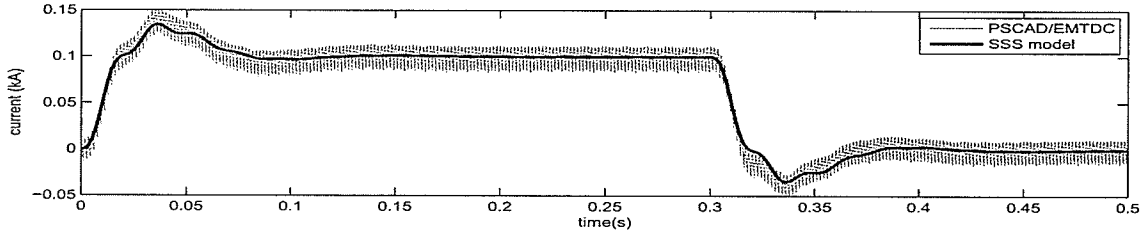

(b) Change in inverter side DC current

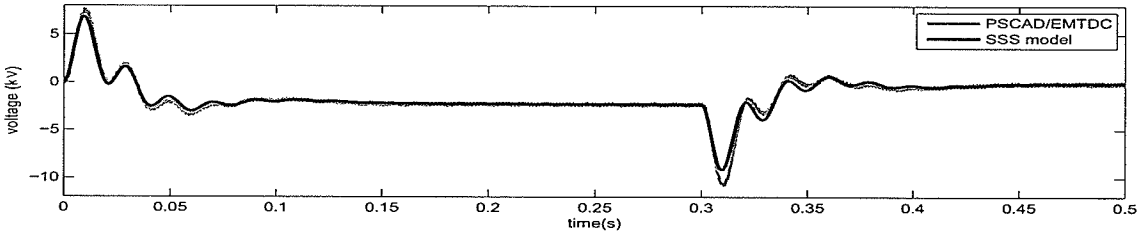

(c) Change in mid-point DC voltage

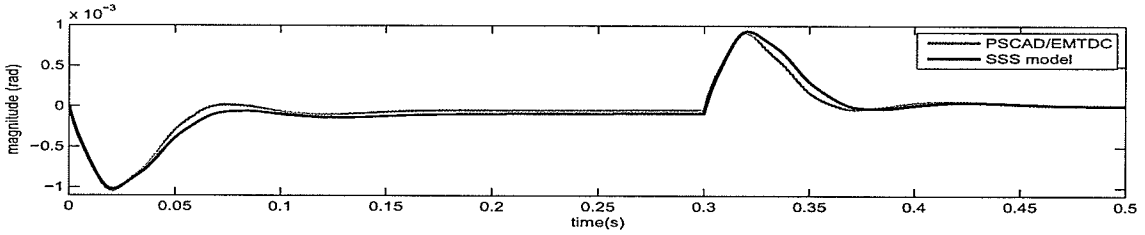

(d) Change in rectifier controller state variable

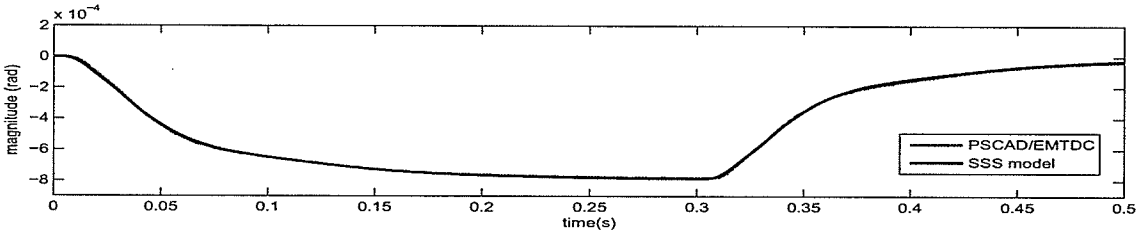

(e) Change in inverter controller state variable

Figure 2.11: Changes in state variables for a 5%, 0.3s pulse on the rectifier current controller input.

are included in the model.

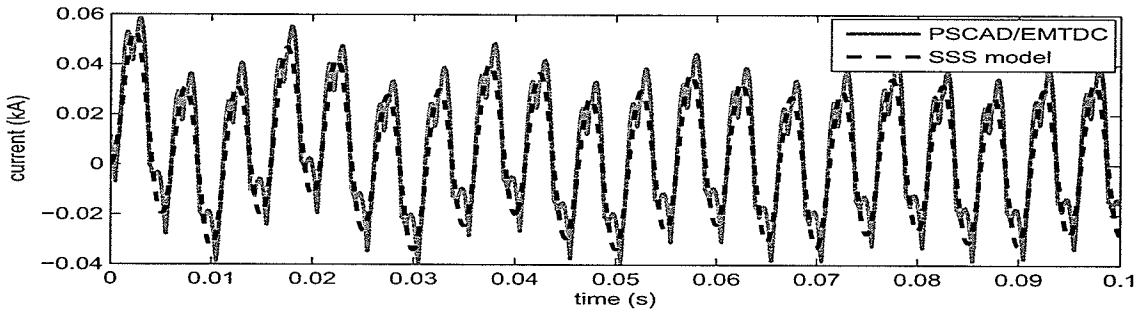

(a) Change in rectifier side DC current

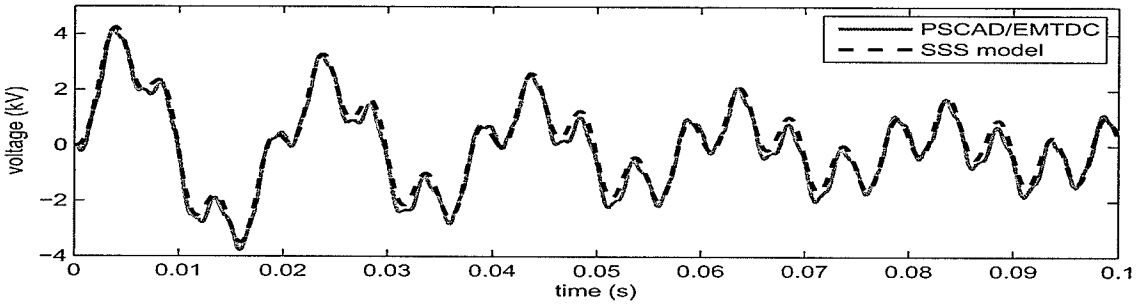

(b) Change in mid point capacitor voltage

Figure 2.12: Changes in state variables for a 5%, 200Hz sinusoidal change in rectifier AC voltage magnitude.

A pulse of magnitude of +5% and duration of 0.3s was applied to the rectifier current controller input. The responses of the controller and DC line state variables obtained using the small signal model are compared with those of PSCAD/EMTDC model in Figure 2.11. It is seen that the results of the linearized model agree well with those of PSCAD/EMTDC. Similar results were obtained for the perturbations applied on the other inputs as well.

In order to demonstrate the accuracy at high frequencies, a 5%, 200Hz sinusoidal change is added to the rectifier AC voltage magnitude and the rectifier side DC current and the mid point capacitor voltage are compared in Figures 2.12(a) and 2.12(b) respectively. The comparisons show a close match even at 200Hz.

Both frequency domain and time domain comparisons verify that the linearized HVDC model adequately represents the dynamics in the frequency range of 0-200Hz.

Therefore, the model is suitable for analyzing interactions such as subsynchronous oscillations.

The AC side converter transformers are included in the HVDC model. The rest of the AC network components are to be modeled separately. In order to obtain meaningful results from an analysis of a AC-DC power system, it is important to model the AC network adequately.

2.3 AC Network Model

All the transmission lines, transformers, static loads and AC filters are included in the AC network model. In conventional small signal stability assessment tools designed for electromechanical oscillation studies, the AC network is represented using the admittance matrix. This method is accurate only for low frequency oscillations (0-3Hz). However, in HVDC and SSO interaction studies, it is necessary to consider some higher frequency interactions (0-60Hz). A more accurate way of representing the AC network is to use a dynamic model [24][23][22]. These representations of the AC network are discussed in the following sections.

2.3.1 Admittance Matrix Representation

In electromechanical oscillation studies, the AC network dynamics are ignored and the network is represented using the power frequency admittance matrix [15]. The relationship between the node voltages and the node current injections are given by Equation 2.30.

$$[\Delta I] = [Y_{bus}][\Delta V] \tag{2.30}$$

ΔI consists of the changes in the currents injected by the dynamic devices at the nodes (busbars). ΔV includes the voltages of the those busbars. Y_{bus} is calculated using the power frequency admittances of the network components.

The modeling details of this technique can be found in [15]. An example case is explained in Appendix B.

2.3.2 Dynamic Network Model

The dynamics of the R-L-C components of the AC network are included in this model. However, the well known dynamic relationships of these components cannot be directly used with the phasor quantities of the voltages and currents. Therefore, a dynamic phasor model [24][23][22], which consists of the relationships of the phasor quantities, is used. The basis of this model is briefly described below.

The complex rotating phasor of an AC current (or voltage) can be expressed as in Equation 2.31.

$$i_{ac} = A_m e^{j\phi} e^{j\omega_0 t} = [A_m \cos(\phi) + jA_m \sin(\phi)] e^{j\omega_0 t} \tag{2.31}$$

Where, A_m is the magnitude of the current and ϕ is the phase of the current. These parameters are referred to as phasor components. ω_0 is the nominal system frequency.

Equation 2.31 can also be written in terms of rectangular coordinate components (real and imaginary axes components) of the phasor components, as shown in Equation 2.32.

$$i_{ac} = (I_R + jI_I) e^{j\omega_0 t} \tag{2.32}$$

Where $I_R = A_m \cos(\phi)$ and $I_I = A_m \sin(\phi)$.

The oscillatory frequencies generated by the dynamic devices are included in the phasor current $(I_R + jI_I)$. For example, the output phasor currents of an HVDC system contain the DC side oscillatory frequencies.

Therefore, the oscillations can be analyzed with respect to the DC side frequencies by considering only the phasor components. Equation 2.32 and the fundamental relationships of the R-L-C components of the network are combined together to obtain the dynamic phasor relationships. It is assumed that the fundamental frequency of the system is constant.

Most of the AC network components can be represented as combinations of series R-L components and parallel R-C components. Therefore, linearized models of series R-L components and parallel R-C components are given below as examples.

Example 1: Series R-L Component

Consider a series R-L circuit connected between nodes 1 and 2. The instantaneous voltage across node 1 and 2 can be written as,

$$v_{12} = L\frac{di_{12}}{dt} + Ri_{12} \tag{2.33}$$

The complex rotating phasor relationships of the currents (eg: Equation 2.32) and voltages are substituted into Equation (2.33) as follows.

$$(V_R + jV_I)e^{j\omega_0 t} = L\frac{d(I_R + jI_I)e^{j\omega_0 t}}{dt} + R(I_R + jI_I)e^{j\omega_0 t} \tag{2.34}$$

The phasor relationship given in equation (2.35) is obtained from Equation (2.34) by assuming that the nominal system frequency (ω_0) is constant.

$$V_R + jV_I = L\frac{d(I_R + jI_I)}{dt} + (R + j\omega_0 L)(I_R + jI_I) \tag{2.35}$$

In Equation 2.35, V_R $(= V1_R - V2_R)$ and V_I $(= V1_I - V2_I)$ are the real part and imaginary part of the phasor voltage deference between node-1 and node-2.

The linearized model of Equation (2.35) is given by Equation (2.36). Note that, all the values are in pu. Since L is in pu, (ω_0/L) terms appear instead of $(1/L)$.

$$\begin{bmatrix} \Delta\dot{I}_R \\ \Delta\dot{I}_I \end{bmatrix} = \begin{bmatrix} \frac{-R\omega_0}{L} & \omega_0 \\ -\omega_0 & \frac{-R\omega_0}{L} \end{bmatrix} \begin{bmatrix} \Delta I_R \\ \Delta I_I \end{bmatrix} + \begin{bmatrix} \frac{\omega_0}{L} & 0 & \frac{-\omega_0}{L} & 0 \\ 0 & \frac{\omega_0}{L} & 0 & \frac{-\omega_0}{L} \end{bmatrix} \begin{bmatrix} \Delta V1_R \\ \Delta V1_I \\ \Delta V2_R \\ \Delta V2_I \end{bmatrix} \tag{2.36}$$

Example 2: Parallel R-C Component

Consider a parallel R-C circuit connected between node 1 and the ground. The instantaneous current injected to the circuit can be written as,

$$i = C\frac{dv_1}{dt} + \frac{1}{R}v_1 \tag{2.37}$$

The phasor relationship similar to Equation (2.35) is given by,

$$I_R + jI_I = C\frac{d(V_{1R} + jV_{1I})}{dt} + (\frac{1}{R} + j\omega_0 C)(V_{1R} + jV_{1I}) \tag{2.38}$$

The linearized model of Equation (2.38) is given by Equation (2.39). Note that, all the values are in pu. Since C is in pu, (ω_0/C) terms appear instead of $(1/C)$.

$$\begin{bmatrix} \Delta\dot{V}_{1R} \\ \Delta\dot{V}_{1I} \end{bmatrix} = \begin{bmatrix} \frac{-\omega_0}{RC} & \omega_0 \\ -\omega_0 & \frac{-\omega_0}{RC} \end{bmatrix} \begin{bmatrix} \Delta V_{1R} \\ \Delta V_{1I} \end{bmatrix} + \begin{bmatrix} \frac{\omega_0}{C} & 0 \\ 0 & \frac{\omega_0}{C} \end{bmatrix} \begin{bmatrix} \Delta I_R \\ \Delta I_I \end{bmatrix} \tag{2.39}$$

All the R-L-C components of the AC network are modeled using the same methodology. The overall network model, which consists of inductor currents and capacitor voltages as state variables, is obtained by combining the currents and voltages using Kirchhoff's laws. A simple example is given in Appendix B.

2.4 Generator Model

The AC network dynamics are neglected in conventional stability models of power systems. To be consistent with the network representation, the stator dynamics of the synchronous generators are also neglected [15]. Therefore, the conventional round rotor (6^{th} order) and the salient pole (5^{th} order) models [15] are used when the admittance matrix is used to represent the AC network. Two additional differential equations for the stator flux components in d-q axes are added to the synchronous machine model, when the AC network is represented using a dynamic phasor model. Therefore, an 8^{th} order model is used for round rotor type and a 7^{th} order model is used for salient pole type. The linearized models of AC4A exciter [37] and non-elastic water column hydro turbine and governor system [38] are combined with the generator models. The linearized models of the generators, the exciters and the governor-turbines are given in Appendix C.

2.5 Multi-Mass Turbine Model

The multi-mass turbine model described in [39] is linearized for analyzing the HVDC-generator-turbine torsional interactions. The masses of the high pressure (HP), intermediate pressure (IP) and low pressure (LPA and LPB) turbines and the generator are included in the analysis. Since the inertia of the exciter mass is low, it is not included in the study. The linearized model is obtained as described in Appendix C.

2.6 Linearized Model of Entire Power System

The linearized models of the dynamic devices of the power system are combined with the AC network model to obtain the overall state space model of the power system. Two small signal models can be obtained based on the AC network model. The admittance matrix representation of the AC network is used in conventional model and the AC network dynamics are included in the other model as described in Section 2.3.2. These linearized models are briefly discussed in the following sections.

2.6.1 Conventional Model

The linearized models of the dynamic devices in the power system are represented using current injection models. The synchronous generators are modeled using 6^{th} order (round rotor type) or 5^{th} order (salient pole rotor type) models neglecting stator winding dynamics. In general, the state space model of the dynamic devices is given by Equations (2.40) and (2.41).

$$\Delta\dot{X} = A_d\ \Delta X + B_d\ \Delta U + E_d\ \Delta V \tag{2.40}$$

$$\Delta I = C_d\ \Delta X + D_d\ \Delta U + Y_d\ \Delta V \tag{2.41}$$

The AC network dynamics are ignored and the network is represented using the admittance matrix model described in Section 2.3.1. The admittance matrix of the network (Equation 2.30) is combined with the current injection equations of the dynamic devices (Equation 2.41) to obtain the voltage terms (ΔV) in terms of state variables and the inputs as given in Equation (2.42).

$$\Delta V = [Y_{bus} - Y_d]^{-1}(C_d\ \Delta X + D_d\ \Delta U) \tag{2.42}$$

The voltage terms obtained in this manner are substituted in the state space equation (Equation 2.40) to obtain the overall state space model given in Equation (2.43).

$$\Delta \dot{X} = A\ \Delta X + B\ \Delta U \tag{2.43}$$

Where, $A = (A_d + E_d[Y_{bus} - Y_d]^{-1}C_d)$ and $B = (B_d + E_d[Y_{bus} - Y_d]^{-1}D_d)$.

More details of this conventional model can be found in Chapter 12 of [15].

2.6.2 Small Signal Model With Network Dynamics

The dynamics of the entire network are included in the small signal model. The network is modeled using the dynamic network model described in Section 2.3.2. Differential and algebraic equations of the dynamic devices are combined with those of the network using Kirchhoff's laws.

In order to explain the implementation aspects, formation of the state space model is briefly discussed in the following text using a simple test system shown in Figure 2.13. In this test system a generator and an HVDC system feed a load in a remote

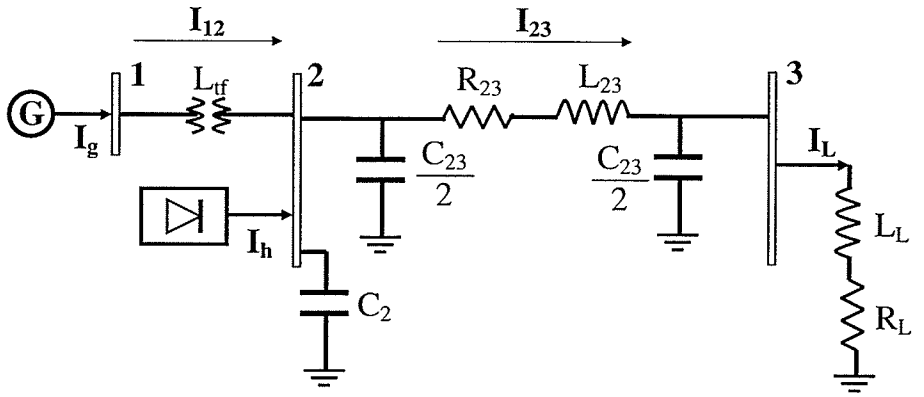

Figure 2.13: Test system used to discuss implementation aspects of dynamic network model

location through a transmission line.

Example: Combining Network Components

The dynamics of series R-L components in the network are given by,

$$\begin{bmatrix} \Delta\dot{I}_{12} \\ \Delta\dot{I}_{23} \\ \Delta\dot{I}_{L} \end{bmatrix} = A_I \begin{bmatrix} \Delta I_{12} \\ \Delta I_{23} \\ \Delta I_{L} \end{bmatrix} + M_{I1}\left[\Delta V_1\right] + M_{I2} \begin{bmatrix} \Delta V_2 \\ \Delta V_3 \end{bmatrix}. \tag{2.44}$$

A_I, M_{I1} and M_{I2} matrices can be obtained as described in Section 2.3.2. Each voltage and current component has two entities for the real and imaginary parts.

Similarly, the dynamics of parallel R-C components are given by,

$$\begin{bmatrix} \Delta\dot{V}_2 \\ \Delta\dot{V}_3 \end{bmatrix} = A_V \begin{bmatrix} \Delta V_2 \\ \Delta V_3 \end{bmatrix} + N_{V1} \begin{bmatrix} \Delta I_{12} \\ \Delta I_{23} \\ \Delta I_L \end{bmatrix} + N_{V2} \left[\Delta I_h\right]. \tag{2.45}$$

The state variables in Equations (2.44) and (2.45) are combined together to obtain the state space model of the network given in Equation (2.46).

$$\Delta\dot{X}_{net} = A_{net}\ \Delta X_{net} + M_{net}\ \Delta V_1 + N_{net}\ \Delta I_h \tag{2.46}$$

Where, ΔX_{net} contains the three current components and the two voltage components given in Equations (2.44) and (2.45) respectively. $A_{net} = \begin{bmatrix} A_I & M_{I2} \\ N_{V1} & A_V \end{bmatrix}$, $M_{net} = \begin{bmatrix} M_{I1} & 0 \\ 0 & 0 \end{bmatrix}$ and $N_{net} = \begin{bmatrix} 0 & 0 \\ 0 & N_{V2} \end{bmatrix}$.

Example: Combining HVDC System

The linear state space model of an HVDC system (or any other dynamic device) can be represented as in Equations (2.47) and (2.48).

$$\Delta\dot{X}_h = A_h\ \Delta X_h + B_h\ \Delta U_h + E_h\ \Delta V_2 \tag{2.47}$$

$$\Delta I_h = C_h\ \Delta X_h + D_h\ \Delta U_h + Y_h\ \Delta V_2 \tag{2.48}$$

Equation (2.48) is substituted in the network model (Equation 2.46) to eliminate ΔI_h terms. The modified Equation (2.46) and the HVDC state Equation (2.47) are

combined together to obtain the resultant state space model.

Example: Combining The Generator

The generator including stator dynamics can be represented as in Equations (2.49) and (2.50). The output current of the generator is a function of the state variables.

$$\Delta \dot{X}_g = A_g \, \Delta X_g + B_g \, \Delta U_g + E_g \, \Delta V_1 \tag{2.49}$$

$$\Delta I_g = C_g \, \Delta X_g \tag{2.50}$$

The generator output current I_g is equal to the generator-transformer current flow I_{12}, which is a state variable of the network model. The relevant network equation is rewritten in Equation (2.51) in terms of the generator current.

$$\Delta \dot{I}_g = A_{tf} \, \Delta I_g + E_{tf1} \, \Delta V_1 + E_{tf2} \, \Delta V_2 \tag{2.51}$$

The time derivative of Equation (2.50) is combined with Equations (2.49) and (2.51) to find ΔV_1 in terms of the state variables, inputs and ΔV_2 (a state variable of the network model). ΔV_1 is then substituted in Equations (2.46) and (2.49) to obtain the overall state space model.

2.7 Adequacy of Linearized Models of Power Systems

The conventional small signal model is accurate enough to analyze electromechanical oscillations of a power system. However, a better model, which includes the AC network dynamics is required to analyze higher frequency oscillations such as HVDC interactions. It is shown in Section 2.2.5 that the linearized HVDC model produces

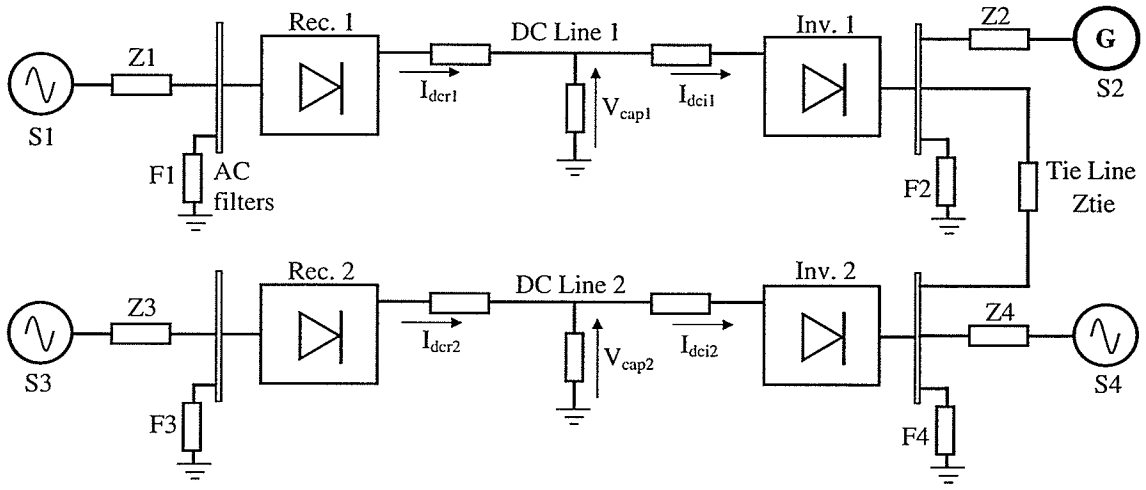

Figure 2.14: Multi-in-feed HVDC test system

accurate results in the frequency range of 0-200Hz. However, when it is combined with the AC networks, the representation of the AC network may also affect the results. Therefore, it is required to validate the linearized models of power systems, which include different AC network models.

In order to analyze the adequacy of the AC network models, a simple test system, in which two HVDC in-feeds are connected through a tie-line, is used. The circuit is shown in Figure 2.14. A synchronous generator is connected at S2 and all other sources are voltage sources. The relevant data are given in Appendix A.

The linearized power system models discussed in Section 2.6 are evaluated for the adequacy. The models are summarized below.

Model-1: Conventional Model (admittance matrix representation for AC network and standard dynamic model of synchronous machine used in stability studies)

Model-2: Small signal model including network dynamics (dynamic phasor representation for AC network and synchronous machine with stator winding differential equations)

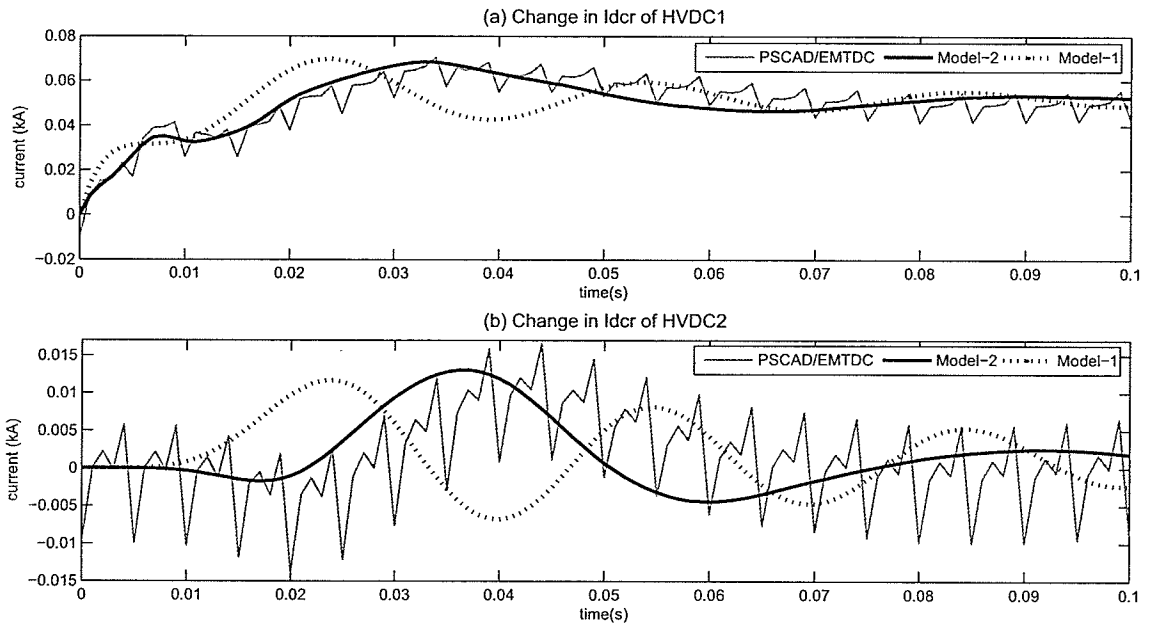

Figure 2.15: Accuracy of different models (initial changes in Rectifier side DC currents for a 5%, 0.3s pulse on the current controller input in HVDC1)

The linearized state space models of the test system were formulated in MATLAB. For small perturbations in the control inputs, the system responses obtained using the linearized models were compared with the responses of the detailed electro-magnetic transient simulations obtained using PSCAD/EMTDC.

A pulse of magnitude of +5% and duration of 0.3s was applied to the rectifier current controller input in HVDC1. The initial transients obtained with small signal models are compared with those of PSCAD/EMTDC in Figure 2.15. Note that the scales of the y-axes of the sub figures (a) and (b) are different. Since the perturbation was applied at HVDC1, much larger changes in the HVDC1 rectifier side DC current can be observed compared to that of HVDC2. It is seen that Model-2 agrees well with PSCAD/EMTDC. Model-1 shows a poorly damped oscillatory frequency which does not agree with PSCAD/EMTDC results.

An extended simulation up to 1.5s for the same perturbation is shown in Figure

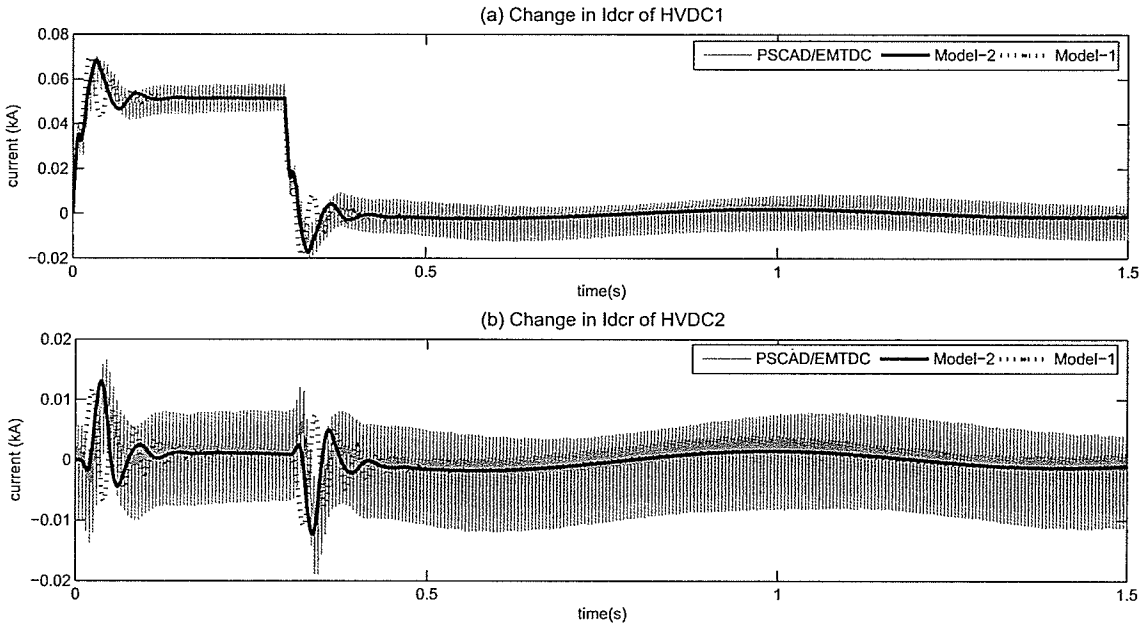

Figure 2.16: Changes in Rectifier side DC currents for a 5%, 0.3s pulse on the current controller input in HVDC1 (An extended simulation)

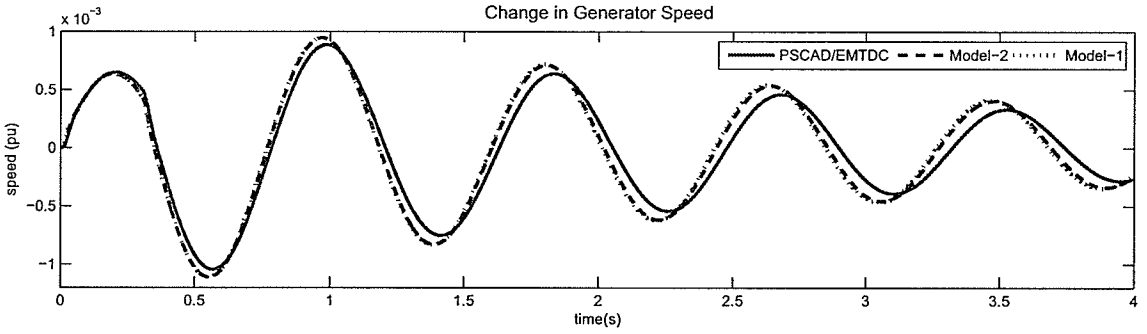

Figure 2.17: Change in generator speed for a 5%, 0.3s pulse on the current controller input in HVDC1

2.16. The DC current of HVDC1 increases by 5% (0.05kA) during the disturbance (0 to 0.3s). The changes in the AC network voltages cause small changes in the HVDC2 currents. The results of Model-2 show a good agreement with the average variation of the time response. It is noticed that the effect of electromechanical oscillations of the generator is also embedded in the current waveforms. Although Model-1 gives

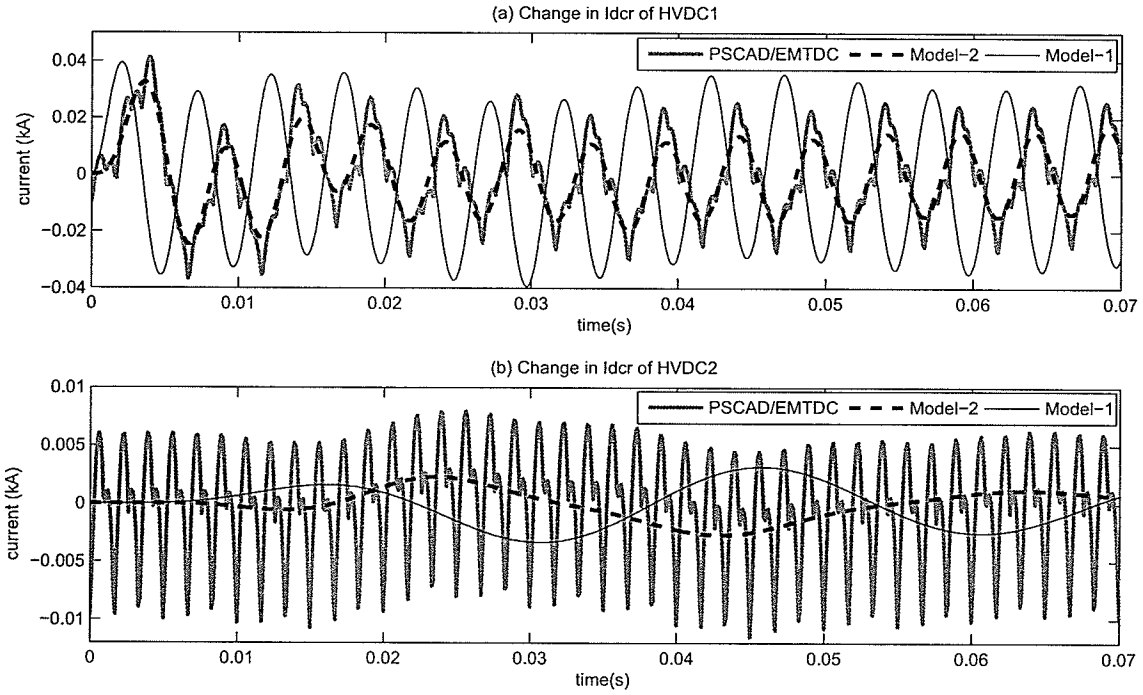

Figure 2.18: Changes in Rectifier side DC currents for a 5%, 200Hz sinusoidal change of the HVDC1 rectifier side AC source voltage (V_{S1})

quite different results for high frequency transients, the waveforms coincide with those of Model-2 and PSCAD/EMTDC in the latter part, where only the low frequency electromechanical oscillations are present. Furthermore, the comparison given in Figure 2.17 for the rotor speed of the generator confirms that both of the models are good for low frequency electromechanical oscillation studies.

Accuracy of the models at high frequencies was further verified by applying a 5%, 200Hz sinusoidal change to the HVDC1 rectifier side AC source voltage (V_{S1}). The changes in rectifier side DC currents of HVDC1 and HVDC2 are compared in Figure 2.18. The disturbance applied at S1 propagates through the AC network (Z1) to the HVDC1. The 200Hz sinusoidal signal can be observed in the rectifier DC current of HVDC1 obtained using PSCAD/EMTDC. The rectifier side DC current obtained

using Model-2 follows PSCAD/EMTDC results well. However, the results of the conventional model (Model-1) is inaccurate at this frequency. The high frequency oscillations dies out at HVDC2 while propagating through Z1, HVDC1 and the tie line (Ztie). Therefore, the 200Hz signal cannot be observed in the rectifier side DC current of HVDC2. PSCAD/EMTDC and Model-2 results well agree for the low frequency changes observed in that current and Model-1 does not show these changes accurately.

In conclusion, The time domain validations provided in this section confirm that the admittance matrix representation of the AC network exhibits some oscillations, which are not present in the more accurate EMT simulations. This confirms that for HVDC interaction studies, a simple model with admittance matrix representation of the network and the generators without stator dynamics is not adequate. The model with dynamic phasor representation of AC network and the generators with stator dynamics shows accurate results, which agree with EMT simulations in the required frequency range. Therefore, this model is used in this thesis to analyze the HVDC interactions in power systems.

2.8 Concluding Remarks

The modeling requirements for small signal stability analysis of power systems with HVDC lines have been analyzed in this chapter. The linearized models of the power system dynamic devices including HVDC systems have been presented. Frequency and time domain comparisons carried out for the small signal and EMT type models confirm that the linearized HVDC model is accurate in the frequency range of 0-200Hz. In the generators, the stator dynamics have been included in the linearized models in order to obtain accurate results in this frequency range.

The adequacy of the admittance matrix representation and the dynamic phasor representation of the AC networks to analyze HVDC interactions in power systems has been investigated. The comparisons of small signal model simulations against EMT type simulations have been used to conclude that the dynamic network representation of the AC network is essential to produce meaningful results from a small signal analysis.

Chapter 3

Hybrid AC Network Model for Large Power Systems

3.1 Introduction

As concluded in Chapter 2, the dynamic network representation of the AC network is essential to produce meaningful results from a small signal analysis of a power system with high frequency interactions such as HVDC interactions. In addition to that, the generators are required to be modeled including stator winding dynamics. Including network dynamics and stator dynamics of generators increase the number of state variables and hence the size of the system matrix A. Therefore, it is impractical to model all the network dynamics of large power systems.

This thesis proposes a single platform, which can be employed to analyze conventional low frequency electromechanical oscillations as well as high frequency interactions using small signal stability assessment. The areas of the network that consist of dynamic devices causing high frequency oscillations are modeled including network dynamics and the rest of the network is modeled using the power frequency admit-

tance matrix. The linearized models of the dynamic devices are combined with the dynamic network models using Kirchhoff's laws. The resultant linearized models of the dynamic network areas are combined with the admittance matrix of the rest of the network using current injection models.

The proposed technique is compared with two small signal stability models: the conventional model with the admittance matrix representation of the network and a more detailed model with a dynamic network model for the entire network. Electromagnetic transient simulations obtained using PSCAD/EMTDC are used as the benchmark for the comparisons. The IEEE New England 39 bus test system [29] with some modifications is used to validate the proposed technique.

3.2 Proposed Hybrid AC Network Model

The areas with the dynamic devices, which produce high frequency oscillations are modeled including network dynamics. For example, the areas with multi-in-feed HVDC systems, generator-turbine torsional oscillations and other FACT devices can be considered. These areas are modeled using the dynamic phasor model described in Section 2.3.2. The rest of the network is modeled using the admittance matrix representation described in Section 2.3.1. The transmission lines at the boundary between two models are treated in a slightly different way. For example, consider the transmission line shown in Figure 3.1. Node 1 is included in the admittance matrix and node 2 is in the dynamic network model. The line capacitance connected to node 2 is modeled using the dynamic model and the line capacitance connected to node 1 is included in the admittance matrix. The series R-L component of the line is modeled using the dynamic model and the current in the series R-L component (I_{12}) is considered as the current injected to the admittance matrix model from the

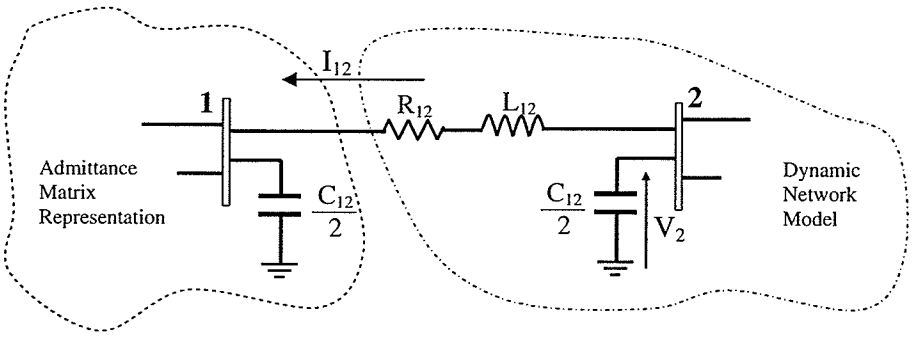

Figure 3.1: Transmission line model at the boundary

dynamic network model. The multiple lines connected between the admittance matrix model and a dynamic network model are treated in the same manner. Therefore, one dynamic network area can be considered as a single dynamic device connected to the admittance matrix model with single or multiple current injections.

In general, the state space model of a dynamic network area can be represented by Equations (3.1) and (3.2).

$$\Delta \dot{X}_{ai} = A_{ai}\ \Delta X_{ai} + B_{ai}\ \Delta U_{ai} + E_{ai}\ \Delta V_{ai} \tag{3.1}$$

$$\Delta I_{out,ai} = C_{ai}\ \Delta X_{ai} \tag{3.2}$$

ΔX_{ai} and ΔU_{ai} contain all the state variables and the inputs of the dynamic devices of i^{th} dynamic area respectively. ΔV_{ai} contains the voltages of the boundary nodes in the admittance matrix model side (similar to node 1 of Figure 3.1). $\Delta I_{out,ai}$ represents the current injections from the dynamic network to the admittance matrix model at those nodes.

The state space model of the dynamic devices connected to the rest of the network (admittance matrix model) is given by Equations (3.3) and (3.4).

$$\Delta\dot{X}_r = A_r\ \Delta X_r + B_r\ \Delta U_r + E_r\ \Delta V \tag{3.3}$$

$$\Delta I_{out,r} = C_r\ \Delta X_r + D_r\ \Delta U_r + Y_r\ \Delta V \tag{3.4}$$

ΔX_r and ΔU_r contain all the state variables and the inputs of the dynamic devices connected to the network except the dynamic areas, respectively. ΔV contains the bus voltages of the network including the boundary nodes (similar to node 1 of Figure 3.1). $\Delta I_{out,r}$ represents the current injections from the dynamic devices to the network.

The state space Equations (3.1) and (3.3) are combined as in Equation (3.5) to obtain the state space equation of the entire system.

$$\begin{bmatrix} \Delta\dot{X}_r \\ \Delta\dot{X}_{ai} \end{bmatrix} = \begin{bmatrix} A_r & 0 \\ 0 & A_{ai} \end{bmatrix} \begin{bmatrix} \Delta X_r \\ \Delta X_{ai} \end{bmatrix} + \begin{bmatrix} B_r & 0 \\ 0 & B_{ai} \end{bmatrix} \begin{bmatrix} \Delta U_r \\ \Delta U_{ai} \end{bmatrix} + \begin{bmatrix} E_r \\ E_a \end{bmatrix} \begin{bmatrix} \Delta V \end{bmatrix} \tag{3.5}$$

In E_a, the value corresponding to i^{th} node is E_{ai} and all the other elements are zero.

The total current injections to the network (admittance matrix model) can be obtained by combining Equations (3.2) and (3.4) as follows.

$$\begin{bmatrix} \Delta I_{out,r} \\ \Delta I_{out,ai} \end{bmatrix} = \begin{bmatrix} C_r & 0 \\ 0 & C_{ai} \end{bmatrix} \begin{bmatrix} \Delta X_r \\ \Delta X_{ai} \end{bmatrix} + \begin{bmatrix} D_r & 0 \\ 0 & 0 \end{bmatrix} \begin{bmatrix} \Delta U_r \\ \Delta U_{ai} \end{bmatrix} + \begin{bmatrix} Y_r \\ 0 \end{bmatrix} \begin{bmatrix} \Delta V \end{bmatrix} \tag{3.6}$$

In summary, the state space Equation (3.5) and the current injections (3.6) can be represented by Equations (3.7) and (3.8) respectively.

$$\Delta\dot{X} = A_1\ \Delta X + B_1\ \Delta U + E_1\ \Delta V \tag{3.7}$$

$$\Delta I_{out} = C_1\ \Delta X_1 + D_1\ \Delta U + Y_1\ \Delta V \tag{3.8}$$

Equation (3.8) is combined with the admittance matrix relationship ($\Delta I = Y\ \Delta V$) of the network, which is to be modeled using conventional model, to obtain the bus voltages in terms of state variables and inputs. The result is then substituted in Equation (3.7) to obtain the overall state space model ($\Delta\dot{X} = A\ \Delta X + B\ \Delta U$).

A computer algorithm to implement the proposed hybrid model is described in Appendix D.

3.3 Validation of Proposed Model

The New England 39 bus test system [29] with some modifications is used to validate the proposed method. The modified test system is shown in Figure 3.2. Bus 38 is kept as an infinite bus and therefore, generator 38 is modeled as a voltage source. Two HVDC in-feeds are connected at busbars 22 and 23 instead of generators 35 and 36. These two HVDC systems along with two capacitor banks provide the same active and reactive power provided by the generators in the original system. CIGRE benchmark HVDC test system [27] with modified current orders are used to model the HVDC in-feeds. The test system details are given in Appendix A.

3.3.1 Small Signal Models of Test System

The following three linearized small signal models are used for comparisons.

Model-1: Conventional Model [admittance matrix representation for AC network and standard dynamic model of synchronous machine used in stability studies]

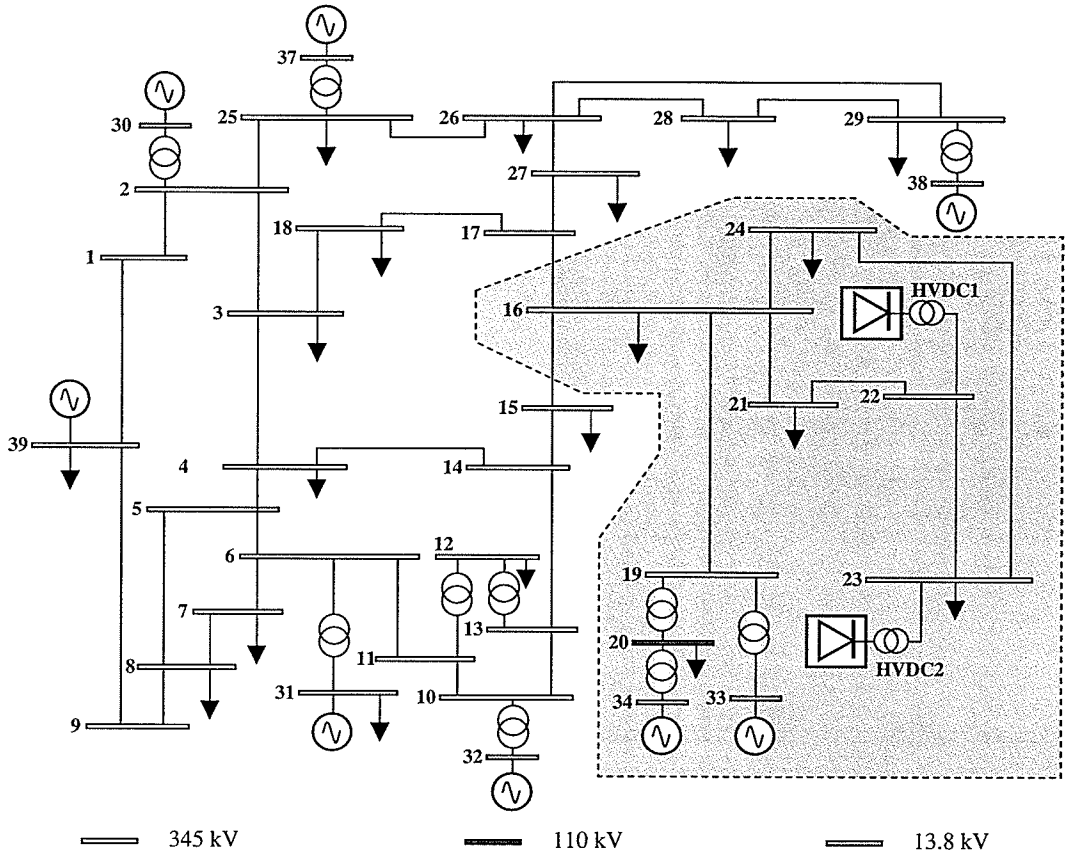

Figure 3.2: 39 bus test system with two HVDC in-feeds

Model-2: Small signal model including network dynamics of entire network [dynamic phasor representation for AC network and synchronous machine models with stator winding differential equations included]

Model-3: *Proposed Hybrid Model* [the area highlighted in Figure 3.2 is modeled including network dynamics (as in Model-2) and the rest is modeled using conventional model (Model-1)]

The three linearized models of the dynamic devices are obtained as described in Chapter 2. The generators in Model-1 are modeled using 6^{th} order generator model

Table 3.1: State Variables in Small Signal Models

System	State Variables		
	Model-1	Model-2	Model-3
HVDC1- Controllers & DC line	5	5	5
HVDC1- PLLs	4	4	4
HVDC1- AC filters	0	24	24
HVDC2- Controllers & DC line	5	5	5
HVDC2- PLLs	4	4	4
HVDC2- AC filters	0	24	24
Generators 33 & 34	28	32	32
Generators 30,31,32,37 & 39	70	80	70
AC network- highlighted area	0	42	42
AC network- other areas	0	138	0
Total state variables	116	358	210

and the generators in Model-2 are modeled including stator dynamics (8^{th} order). In Model-3, generators 33 and 34 are modeled using 8^{th} order model and the rest is modeled using 6^{th} order model. The linearized models of AC4A exciter [37] and non-elastic water column hydro turbine and governor system [38] are combined with the generator models.

In the linearized HVDC models, constant current controllers are included at the rectifier ends and constant DC voltage controllers are used at the inverter ends.

The state variables in the systems are summarized in Table 3.1. Model-1 consists of 116 state variables. When the entire system is modeled including the network dynamics (Model-2), the state space model has 358 state variables. This number can be significantly reduced to 210 when the proposed model (Model-3) is used.

Selection of Dynamic Area

The studies have shown that the same results can be obtained as in Model-3 by modeling Buses 21, 22, 23 and 24 in the dynamic area and Bus 16 as the boundary bus

(186 state variables in total). This has been expected since the points of interconnections of HVDC systems (Bus 22 and Bus 23) are around 100 km away from Bus 16 at which the highlighted area is connected to the rest of the systems. This gives an idea how the buses in the dynamic areas should be selected. In order to obtain accurate results, a considerable distance from the dynamic devices with the high frequency interactions should be modeled in the dynamic area.

The increment in number of state variables in this example from conventional model to the hybrid model is 116 to 210, which appears to be significant. It should be noted that in this example a significant portion of the network is included in the dynamic network. In practice, for a large network, the dynamic part of the network model is a small proportion of the entire network and therefore, the relative increment in number of state variables will be much smaller. For example, consider a mid size power system with 3000 buses, 3000 branches and 100 generators. The conventional model may contain around 1400 state variables if the generators, exciters and turbine-governor units are modeled. If there is one area with multi-HVDC in-feeds and 20 transmission lines are to be included in the dynamic area, this may add at most 150 state variables, making 1550 state variables in total (10.7% increase in state variables). This does not make a significant computation burden.

3.3.2 Validations Using Time Domain Simulations

Small signal responses of the models 1, 2 and 3 are obtained for the disturbances applied at the inputs and the results are compared with the detailed EMT simulation results obtained using PSCAD/EMTDC.

A step of magnitude of +5% and duration of 0.3s was applied to the rectifier current controller input in HVDC1. The initial transients of the rectifier side DC

currents and the inverter side DC currents obtained using the small signal models are compared with those of PSCAD/EMTDC in Figure 3.3 and Figure 3.4 respectively. Note that the scales of the y-axes of the sub figures (a) and (b) are different. Since the perturbation was applied at HVDC1, much larger changes in the HVDC1 DC currents can be observed compared to those of HVDC2.

The results obtained using Model-2 match well with PSCAD/EMTDC results. The proposed model (Model-3) also gives results close to the results of Model-2 and PSCAD/EMTDC. The results obtained using the conventional model (Model-1) are quite different from the others. Much more differences can be observed in HVDC2 currents since the changes in HVDC2 are due to the changes in AC network voltages and currents which are caused by the current injections of HVDC1, in which the disturbance is applied.

As far as electromechanical oscillations are concerned, all the small signal models give accurate results. This is evident in the generator speed comparisons given in Figure 3.5. Therefore, the proposed technique can be used for electromechanical oscillation studies as well.

Accuracy of the models at high frequencies was further verified by applying a 5%, 200Hz sinusoidal change to the HVDC1 rectifier side AC source voltage. The changes in rectifier side DC currents of HVDC1 and HVDC2 are compared in Figure 3.6. The model with AC network dynamics of entire system (Model-2) and the proposed hybrid model (Model-3) give the same results, which show a very good agreement with the PSCAD results. The conventional model (Model-1) is not accurate at this frequency.

In conclusion, the proposed model gives accurate results for HVDC high frequency oscillations as well as for electromechanical oscillations. The accuracy of the model

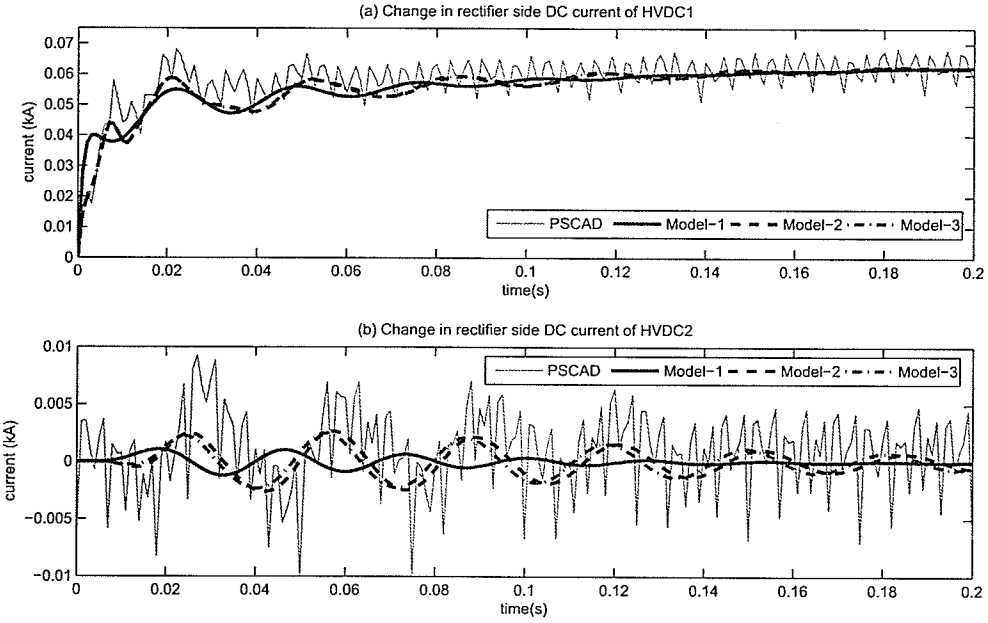

Figure 3.3: Initial changes in rectifier side DC currents for a 5%, 0.3s step on the current controller input in HVDC1

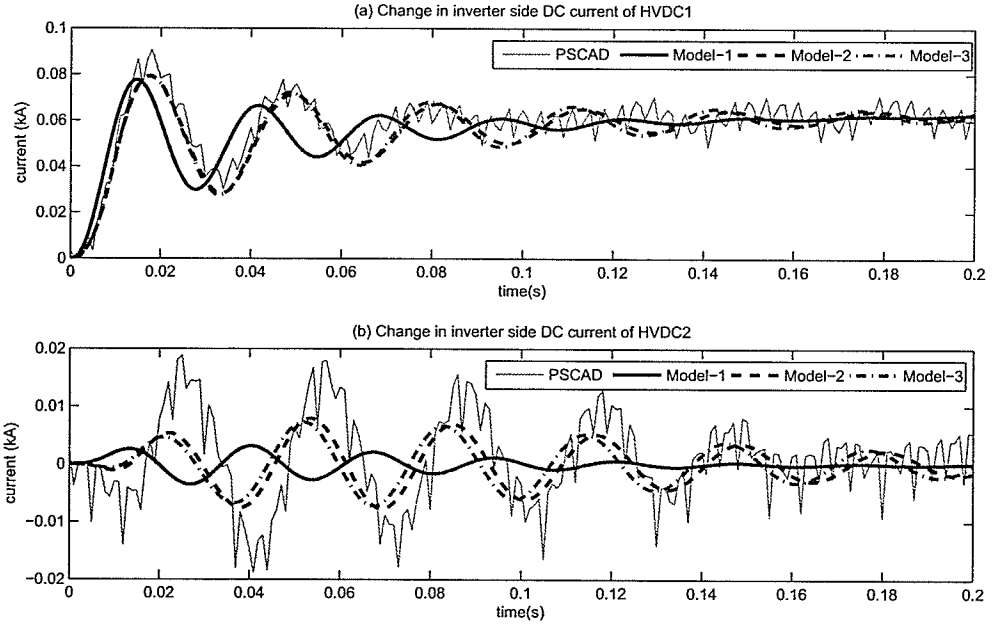

Figure 3.4: Initial changes in inverter side DC currents for a 5%, 0.3s step on the current controller input in HVDC1

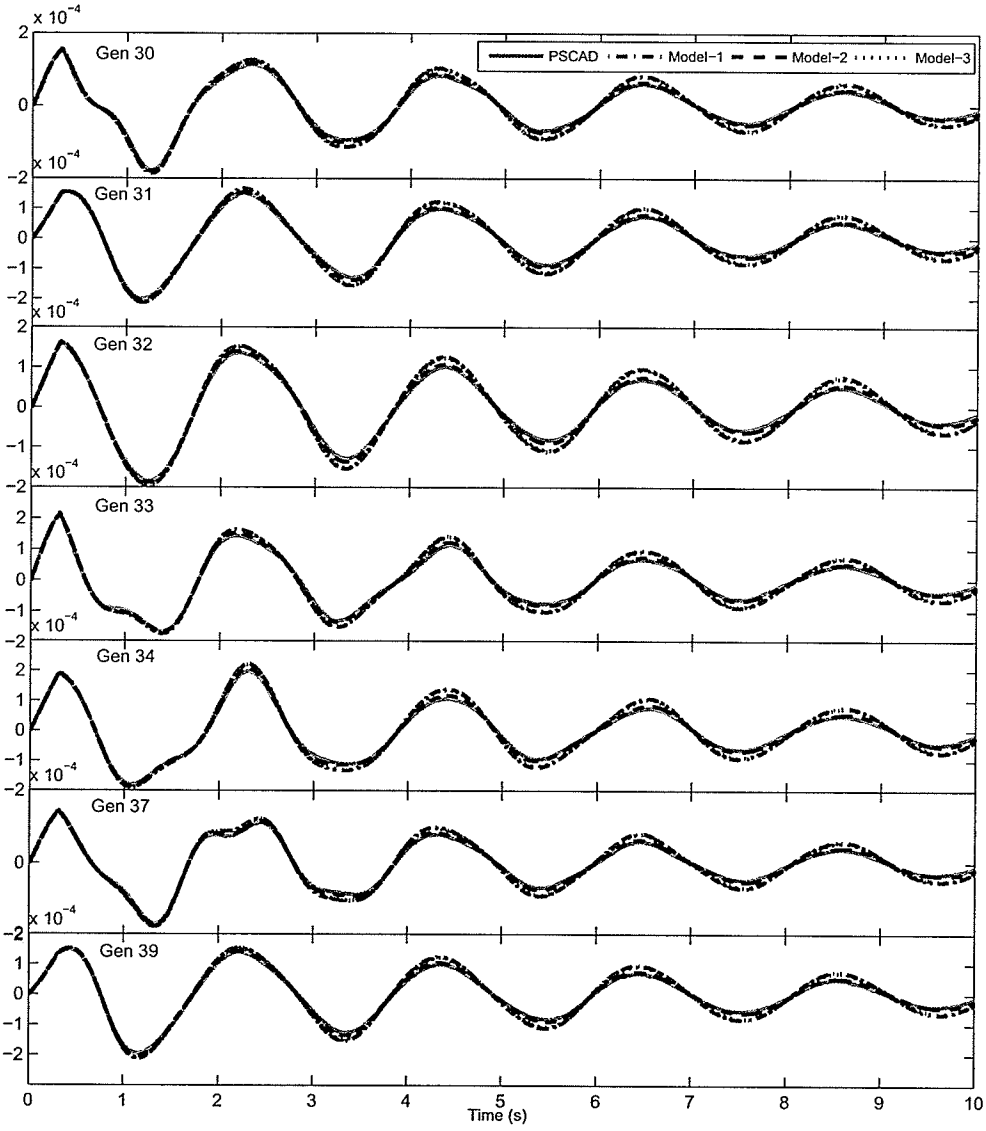

Figure 3.5: Changes in generator rotor speeds (in pu) for a 5%, 0.3s step on the current controller input in HVDC1

is further investigated in Chapters 5 and 6 while analyzing HVDC interactions using modal analysis.

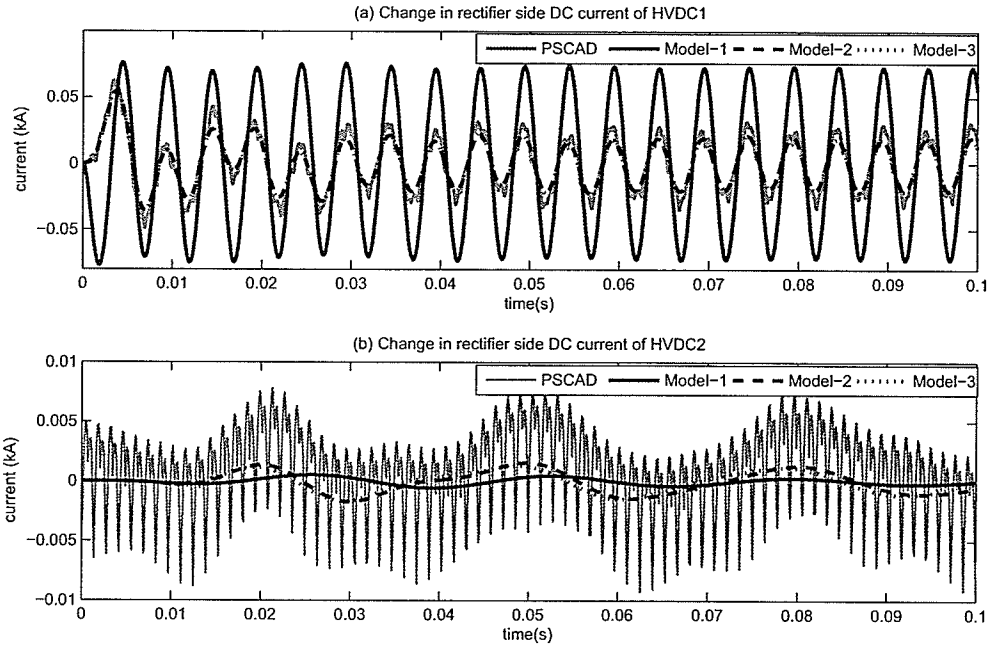

Figure 3.6: Changes in rectifier side DC currents for a 10%, 200Hz 200Hz sinusoidal change of the HVDC1 rectifier side AC source voltage

3.4 Concluding Remarks

A computationally efficient small signal stability model suitable for studying HVDC interactions has been proposed in this chapter. The required accuracy and the computation efficiency have been achieved using a hybrid AC network model that allows the parts of the transmission network in the vicinity of HVDC converters or any other dynamic devices to be modeled with their dynamics and the remaining parts to be modeled as constant admittances. The time responses of the proposed model have been validated against an electromagnetic transient simulation program (PSCAD/EMTDC). The constant admittance transmission network model (Model-1) produces inaccurate time responses. When the entire network is modeled with its dynamics (Model-2) the time response closely agrees with the PSCAD/EMTDC simulation. However, for large networks, the dynamic representation of the entire

transmission network leads to large computation burden due to the large system matrix. The proposed model (Model-3), which is a hybrid of the above two, gives time responses that are almost identical to those obtained for Model-2. The proposed hybrid modeling approach would be useful for studying subsynchronous frequency range interactions in power systems.

Chapter 4

Small Signal Stability Assessment of Power Systems

4.1 Introduction

Small signal stability is concerned with the ability of power systems to maintain the synchronism under small disturbances [17]. This type of stability is analyzed by applying Lyapunov's first stability criteria [18] to the linearized state space model of the power system.

Chapters 2 and 3 described the linearized models of the power systems. The local stability around the operating point, at which the system is linearized, is analyzed using the eigenvalue analysis of the system matrix of the linearized state space model. This chapter briefly describes the small signal stability and eigenvalue (modal) analysis of power systems. More details can be found in [15] (power system aspects) and in [40] (linear control theory).

4.2 Stability of Linearized Systems

The linearized state space model of a dynamical system is given in Equation (4.1).

$$\Delta\dot{X} = A\ \Delta X + B\ \Delta U \tag{4.1}$$

Where, ΔX is the vector of state variables and ΔU is the vector of inputs in the system.

The eigenvalues of the system matrix (A) are obtained by solving Equation (4.2).

$$det(A - \lambda I) = 0 \tag{4.2}$$

If the system has 'n' state variables, Equation 4.2 has 'n' independent solutions $(\lambda_1, \lambda_2, ..., \lambda_n)$. These solutions are the eigenvalues of the system.

The local stability (*stability in the small*) of the system at the operating point, where the system is linearized, is determined using Lyapunov's first theorem [18]. The criterion is summarized in [15] as follows.

- "When the eigenvalues have negative real parts, the original system is asymptotically stable."
- "When at least one of the eigenvalues has a positive real part, the original system is unstable."
- "When the eigenvalues have real parts equal to zero, it is not possible on the basis of the first approximation to say anything in the general."

This stability criterion is interpreted as the stability of the modes of the system as described in the following section.

4.3 Modes and Modal Characteristics

The modes of the system are identified using eigenvalues and the modal characteristics are analyzed using eigenvectors. Some important concepts are summarized in this section.

4.3.1 Modes

If there are no changes in the system inputs, the state space model of the system can be rewritten as in Equation (4.3). This is the free motion of the system.

$$\Delta \dot{X} = A\ \Delta X \tag{4.3}$$

The rate of change of each state variable is a linear combination of all the state variables of the system. These cross couplings of the state variables can be eliminated by using the transformation given by,

$$\Delta X = \Phi Z \tag{4.4}$$

Where, Φ is right eigenvector matrix of the system matrix (A).

After the transformation, the state space model becomes

$$\dot{Z} = \Lambda Z \tag{4.5}$$

Λ is a diagonal matrix with the eigenvalues as the diagonal elements. Therefore, the rate of change of i^{th} variable is given by,

$$\dot{z}_i = \lambda_i z_i \tag{4.6}$$

The transformation produces 'n' independent variables. These variables are called the modes of the dynamical system. The modes describe the dynamic behavior of the system. The time response of i^{th} mode is given by Equation (4.7).

$$z_i(t) = z_i(0)e^{\lambda_i t} \tag{4.7}$$

The time dependent characteristic of i^{th} mode is given by $e^{\lambda_i t}$. Therefore, the modes and their stability is described by the eigenvalues as follows.

- A real eigenvalue corresponds to an aperiodic (non-oscillatory) mode. If the eigenvalue is negative the mode is a decaying mode and if it is positive, the mode is unstable (aperiodic instability).

- A complex conjugate pair of eigenvalues corresponds to an oscillatory mode. If the eigenvalue pair is, $\lambda = \sigma \pm j\omega$,

  The frequency of oscillation is given by,

$$f = \frac{\omega}{2\pi} \tag{4.8}$$

  The damping ratio is given by,

$$\zeta = -\frac{\sigma}{\sqrt{\sigma^2 + \omega^2}} \tag{4.9}$$

  If the real part of the eigenvalues is negative (i.e. damping ratio is positive), the mode is stable. The magnitude of the damping ratio determines the rate of decay of the amplitude of the oscillation.

4.3.2 Mode Shapes (Right Eigenvectors)

The right eigenvector of a particular mode gives the mode shape, which shows the relative phasors of the state variables when that mode is excited. The right eigenvector (Φ_i) of i^{th} mode is given by,

$$A\Phi_i = \lambda_i \Phi_i \tag{4.10}$$

Assume, only i^{th} mode of the system is excited. Then, the state variables are given by,

$$\begin{pmatrix} \Delta X_1 \\ \Delta X_2 \\ \vdots \\ \Delta X_3 \end{pmatrix} = \begin{pmatrix} \phi_{i1} \\ \phi_{i2} \\ \vdots \\ \phi_{i3} \end{pmatrix} z_i \tag{4.11}$$

$\phi_{i1}, \phi_{i2}, \ldots, \phi_{in}$ are the elements of i^{th} right eigenvector (Φ_i).

The magnitudes of the elements of Φ_i give the relative activities of the state variables in i^{th} mode and the phase angles give the phase displacement of the state variables with regards to the mode. Since the units and scaling of the state variables are different, the magnitudes of the elements cannot be compared against each other. Therefore, only the phase angles of the mode shapes are considered in this thesis while analyzing HVDC interactions.

4.3.3 Left Eigenvectors

The left eigenvector (Ψ_i) of i^{th} mode is given by,

$$\Psi_i A = \lambda_i \Psi_i \tag{4.12}$$

Assume, only i^{th} mode of the system is excited. The mode is given by,

$$z_i = \psi_{i1}\Delta X_1 + \psi_{i2}\Delta X_2 + \cdots + \psi_{in}\Delta X_n \tag{4.13}$$

$\psi_{i1}, \psi_{i2}, \ldots, \psi_{in}$ are the elements of i^{th} right eigenvector (Ψ_i).

The elements of Φ_i are the weights of the state variable to the i^{th} mode.

4.3.4 Participation Factors

The participation factors [41][42], which are independent of the units and scaling of the state variables are used to measure the relative participation (magnitude) of the state variables in a mode. The participation factors are obtained from the multiplications of the elements of the right eigenvector and the left eigenvector.

The participation factor (p_{ki}) is given by,

$$p_{ki} = \phi_{ki}\psi_{ik} \tag{4.14}$$

Where, ϕ_{ki} is the k^{th} element of i^{th} right eigenvector (a column vector) and ψ_{ik} is the k^{th} element of i^{th} left eigenvector (a raw vector).

p_{ki} is the relative participation of the k^{th} state variable in the i^{th} mode. All the participation factors of the i^{th} mode are arranged in a vector to obtain the participation vector as given in Equation (4.15).

$$p_i = \begin{pmatrix} p_{1i} \\ p_{2i} \\ \vdots \\ p_{ni} \end{pmatrix} \tag{4.15}$$

The elements of p_i are dimensionless and the sum of the elements is 1. Therefore, the participation factors (elements) can be used as an index to compare the relative participation of the state variables in that mode. Since the participation factors of an oscillatory mode are complex numbers, the magnitudes of the participation factors are used for the comparisons. In this thesis, the magnitude of the highest participant is considered as 100% and other participations are scaled accordingly.

The participation factor matrix of the system is, $P = [p_1, p_2, \ldots, p_n]$. This matrix gives the participation of the state variables in all the modes of the system.

4.3.5 Mode Controllability and Observability

The decoupled forms of the state equations are given by,

$$\dot{Z} = \Lambda\ Z + \Psi B\ \Delta U \tag{4.16}$$

$$\Delta Y = C\Phi\ Z + D\ \Delta U \tag{4.17}$$

Where, right eigenvector matrix, $\Phi = [\Phi_1, \Phi_2, \ldots, \Phi_n]$ and

left eigenvector matrix, $\Psi = [\Psi_1^T, \Psi_2^T, \ldots, \Psi_n^T]^T$.

In Equation (4.16), the element of $[\Psi B]$ corresponding to a particular mode and an input determines whether the mode can be controlled through that input. If the element is zero, the mode cannot be controlled (uncontrollable). Therefore, $[\Psi B]$ is

referred to as the *mode controllability matrix.*

The system response at an output (Y) can be obtained by Equation (4.17). The element of $[C\Phi]$ corresponding to a particular mode and an output determines whether the mode can be observed in that output. If the element is zero, the mode cannot be observed (unobservable). Therefore, $[C\Phi]$ is referred to as the *mode observability matrix.*

4.4 Summary: Modal Analysis Used in The Thesis

The modal analysis technique used in the thesis is summarized below.

- The aperiodic and oscillatory modes are identified using eigenvalues and stability of the modes are evaluated. The frequency and the damping of the oscillatory modes are obtained using Equations (4.8) and (4.9).

- The relative participation of the state variables in the modes are obtained using participation factors. The interactions among the state variables of different dynamical systems are identified using these participations.

- The phase angles of the mode shapes are used to identify the relative action of the state variables in a particular mode.

  If two state variables have almost the same phase angle (around 0^o phase displacement) in the mode shapes of a particular mode, the two state variables are said to be "*oscillating together*" in that mode.

  If two state variables have almost 180^o phase displacement in the mode shapes

of a particular mode, the two state variables are said to be "*oscillating against each other*" in that mode.

- Observability and controllability matrices are used to identify the inputs and the outputs for the controllers, which are utilized to improve the damping of some lightly damped modes.

Chapter 5

HVDC Interactions in Power Systems

5.1 Introduction

The HVDC interactions in power systems are analyzed using the small signal stability assessment described in Chapter 4. The following interactions in power systems are discussed in this chapter.

- Multi-in-feed HVDC interactions - Interactions among the controllers and DC lines of different HVDC links connected to a power system in a close proximity.
- HVDC-generator electromechanical interactions - Interactions between an HVDC link and a generator connected to a power system in a close proximity.

These HVDC interactions are analyzed in detail using two case studies: a small multi-in-feed test system (Case Study-1) and a large power system (Case Study-2). In Case Study-2, the proposed hybrid AC network model (Chapter 3) is also used to

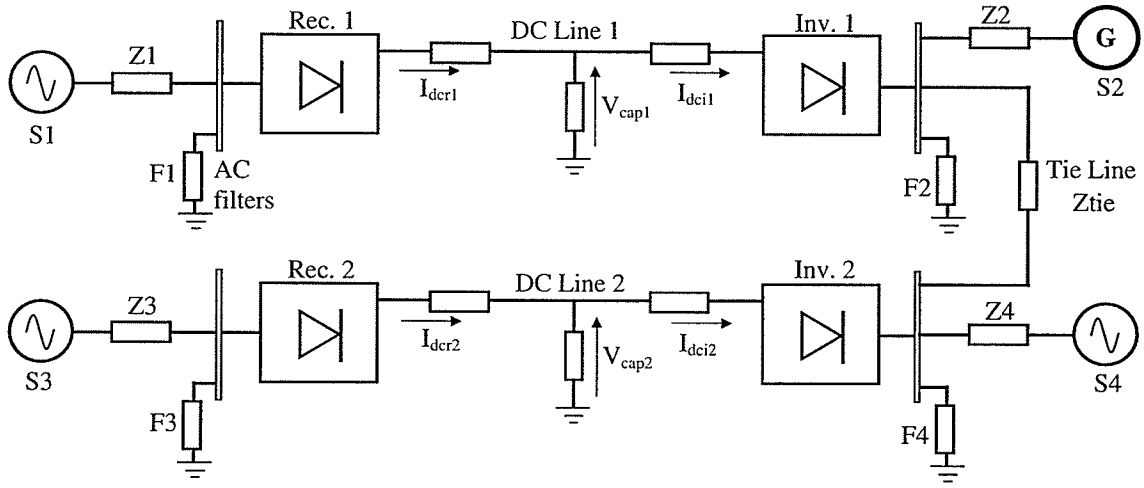

Figure 5.1: Multi-in-feed HVDC test system (redrawn - same as Figure 2.14)

analyze the interactions and the performance of the model is compared against the detailed model.

In addition to these interactions, the HVDC-generator-turbine torsional interactions (subsynchronous oscillations) are analyzed in Chapter 6.

5.2 Case Study-1: Multi-in-feed HVDC Interactions

The multi-in-feed HVDC test system shown in Figure 2.14 of Chapter 2 is used to analyze the interactions. For the clarity of the readers, the test system is redrawn in Figure 5.1. There are two HVDC in-feeds (HVDC1 and HVDC2) connected through a tie-line and one generator (S2) is connected close to HVDC1.

5.2.1 Small Signal Model of Test System

The linearized model of the test system is obtained as described in Chapter 2. The rectifier current controller, the inverter extinction angle controller and the PLOs are included in the HVDC models. The dynamic AC network model is used to model the

Table 5.1: Major Participations of Some Selected Modes in Multi-in-feed Test System

Mode	Freq. (Hz)	D (%)	Major Participants
1	148.1	3.1	$I_{Z2}(100\%)$, $F2(80\%)$, $I_{Z4}(70\%)$, $F4(70\%)$
2	104.8	30.4	$F4(100\%)$, $F2(50\%)$, $I_{tie}(40\%)$
3	75.9	10.9	$I_{dcr1}(100\%)$, $I_{Z1}(70\%)$, $I_{dcr2}(60\%)$, $F1(50\%)$
4	74.9	10.4	$I_{dcr2}(100\%)$, $I_{Z3}(70\%)$, $I_{dcr1}(60\%)$, $F3(50\%)$
5	66.0	17.6	$I_{dci1}(100\%)$, $F2(80\%)$, $I_{Z2}(60\%)$, $I_{dci2}(60\%)$, $F4(40\%)$, $I_{Z4}(40\%)$
6	34.0	20.2	$V_{cap2}(100\%)$, $I_{dci2}(80\%)$, $V_{cap1}(60\%)$, $I_{dci1}(50\%)$
7	17.9	30.9	$V_{cap1}(100\%)$, $X_{\alpha r1}(70\%)$, $I_{Z2}(70\%)$, $V_{cap2}(60\%)$
8	17.0	72.7	$X_{\alpha r1}(100\%)$, $I_{dcr1}(70\%)$, $V_{cap1}(70\%)$, $X_{\alpha r2}(60\%)$
9	7.0	93.7	$X_{\alpha r2}(100\%)$, $X_{\alpha r1}(60\%)$, $I_{dcr2}(50\%)$, $I_{dcr1}(30\%)$
10	1.2	4.6	$\delta(100\%)$, $\phi_d(100\%)$, $\omega(90\%)$, $I_{Z2}(40\%)$

network. The synchronous machine is modeled using an 8^{th} order model including stator winding dynamics. The exciter and governor models are also included in the generator model. The entire system consists of 96 state variables. Most of the state variables are associated with the AC network and 9 state variables of each HVDC system and 16 state variables of the generator are also included. Some important modes of the system are given in Table 5.1. In the participations, Fn $(n = 1..4)$ represents the state variables of n^{th} AC filter and I_{Zn} $(n = 1..4)$ represents the currents of n^{th} source impedance. The numbers shown within parentheses are the scaled participations. Since the AC filters and impedances involve a large number of state variables, the rounded value of the highest participant of them is presented in

the table.

The oscillatory modes given in Table 5.1 are used to identify the interactions. The modes are categorized into AC network interactions, DC line resonance interactions and controller interactions based on the highest participants.

5.2.2 AC Network Interactions

Modes 1 to 5 show the AC network interactions. Inspection of major participants shown in Table 5.1 reveals that, Mode 1 is the most critical mode in the system in which the inverter side AC network and filter state variables participate the most. There are minor contributions of the inverter side DC currents and the generator stator flux components in this mode. Mode 2 shows the interactions among the inverter side filters and the tie line. The interactions among the DC currents, the AC network and the filters are given by modes 3,4 and 5.

5.2.3 DC Line Resonances

Modes 6 and 7 in Table 5.1 are due to the inductor-capacitor resonances of the DC lines. The participation of all 88 state variables in Mode 6 is illustrated in Figure 5.2. Note that in Figure 5.2, the state variables of HVDC systems are arranged in the order [$X_{\alpha r}$, $X_{\alpha i}$, I_{dcr}, I_{dci}, V_{cap} and four PLO variables]. The mid-point capacitor voltage (100%) and the inverter side DC current (80%) of HVDC2 participate the most in this mode. There are significant contributions from the mid point DC voltage (60%) and the inverter side DC current (50%) of HVDC1 as well. The mode shapes of mode 6 illustrated in Figure 5.3 show that the relevant state variables of HVDC1 and HVDC2 are almost 180° out of phase with each other. For example, I_{dcr1} of HVDC1 and I_{dcr2} of HVDC2 are almost 180° apart. Therefore, the relevant state variables of

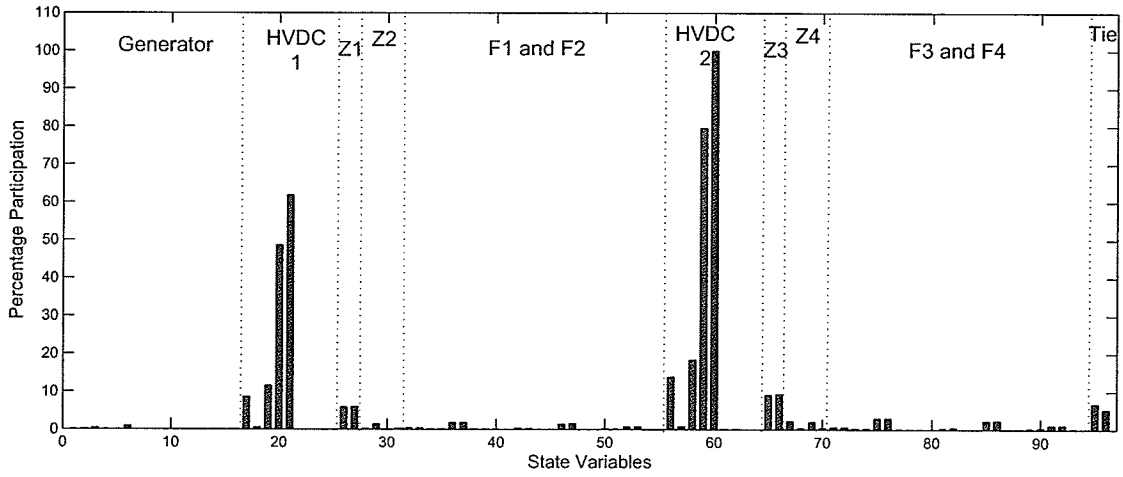

Figure 5.2: Participation of state variables in mode 6 of Model-1 (Table 5.1). Note that, the state variables of HVDC systems are arranged in the order [$X_{\alpha r}$, $X_{\alpha i}$, I_{dcr}, I_{dci}, V_{cap} and four PLO variables].

HVDC1 and HVDC2 "oscillate against each other" in this mode.

The major contributor for Mode 7 is HVDC1. The mode shapes (Figure 5.3) show that the angle between the relevant state variables of HVDC1 and HVDC2 is small. Therefore, the relevant state variables of HVDC1 and HVDC2 "oscillate together" in this mode.

5.2.4 Controller Interactions

The controller state variables $X_{\alpha r1}$ and $X_{\alpha r2}$ participate most in modes 8 and 9 as in Table 5.1. Therefore these modes are identified as controller modes. The major contributor for Mode 8 is HVDC1. The mode shapes (Figure 5.3) show that HVDC1 and HVDC2 oscillate together in this mode. The participation of state variables in Mode 9 is illustrated in Figure 5.4. The major contributor in this mode is the rectifier current controller state variable of HVDC2 ($X_{\alpha r2}$ - 100%). The participation of the rectifier current controller state variable of HVDC1 ($X_{\alpha r1}$) is 60%. In addition to

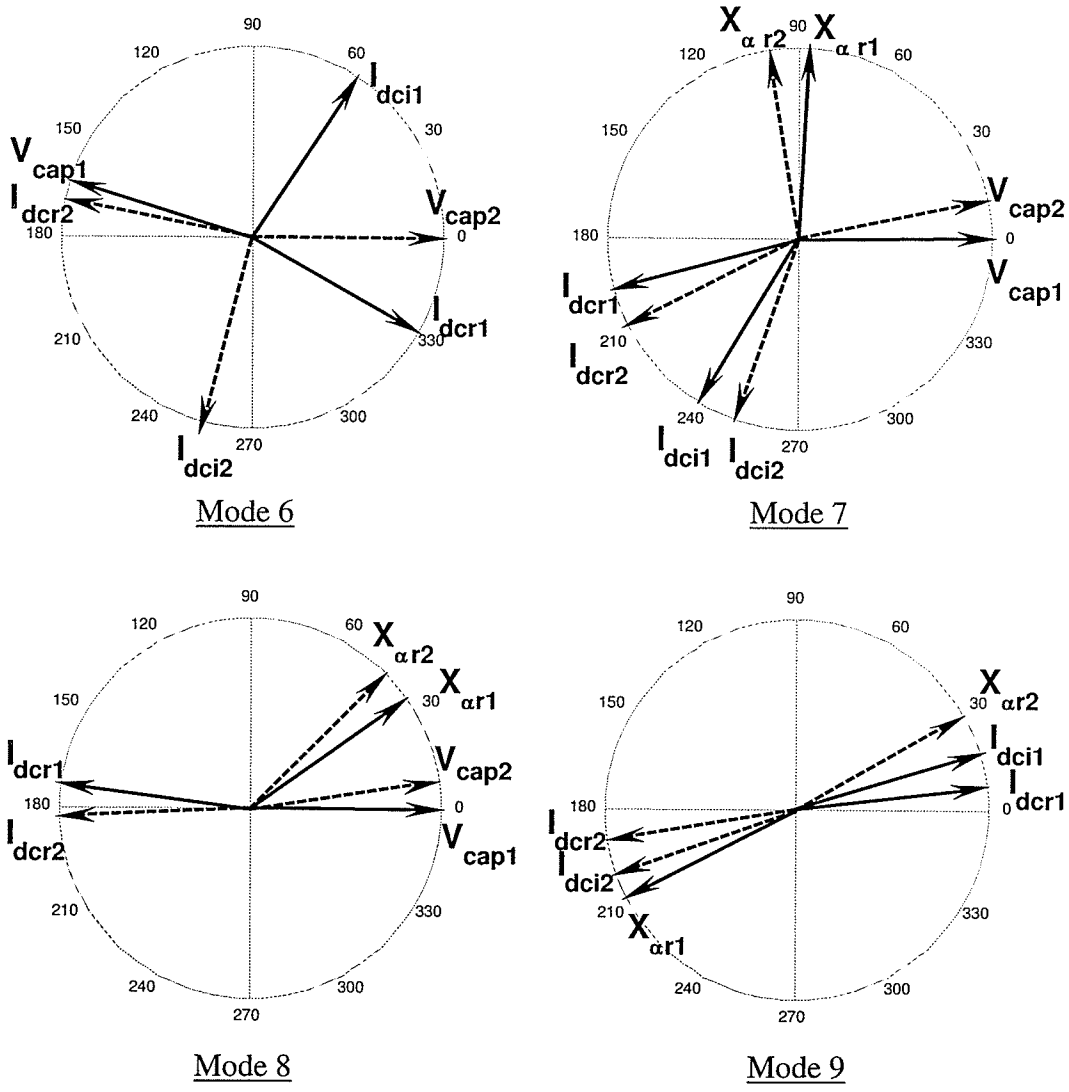

Figure 5.3: Mode shapes of major participants - Modes 6,7,8 and 9 (Table 5.1)

those, the rectifier side DC currents of HVDC2 (50%) and HVDC1 (30%), and the inverter side DC currents of HVDC2 (20%) and HVDC1 (10%) participate in this mode. The mode shapes of the major participants illustrated in Figure 5.3 reveal that HVDC1 and HVDC2 state variables oscillate against each other in this mode. In this test system, the controller modes are highly damped and therefore, can hardly be observed in the responses.

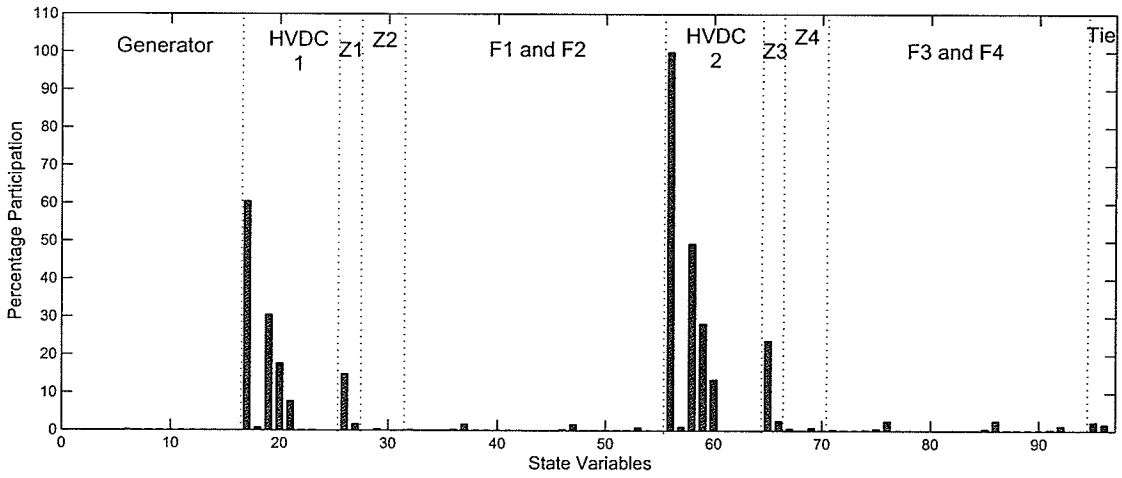

Figure 5.4: Participation of state variables in mode 9 of Model-1 (Table 5.1). Note that, the state variables of HVDC systems are arranged in the order [$X_{\alpha r}$, $X_{\alpha i}$, I_{dcr}, I_{dci}, V_{cap} and four PLO variables].

5.2.5 Effect of Tie Line Impedance

The interaction between HVDC1 and HVDC2 depends on the tie line impedance (i.e. how tightly the HVDC systems are coupled). If the tie line impedance is high, the interactions between the two HVDC lines diminish. For example, when the tie line impedance is 5 times larger, the participation in the similar DC line resonance mode corresponding to Mode 6 is as shown in Figure 5.5 and the participation in the similar controller mode corresponding to Mode 9 is as shown in Figure 5.6. It can be seen that, the contributions of HVDC1 in these modes are negligible. The participations of the corresponding modes of Modes 7, 8 also show that the interactions between the HVDC systems are negligible when the tie line impedance is increased.

5.2.6 Effect of Current Controller

It is found from the above analysis that the rectifier current controller significantly contributes to the DC line resonance and controller modes. The current controller

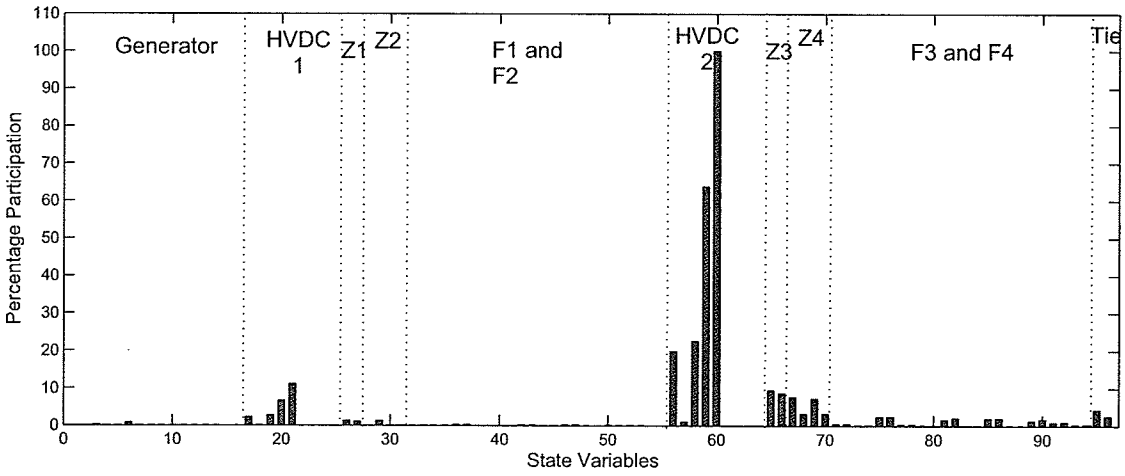

Figure 5.5: Participation of state variables in the similar mode corresponding to mode 6 (Table 5.1) when the tie line impedance is increased by 5 times

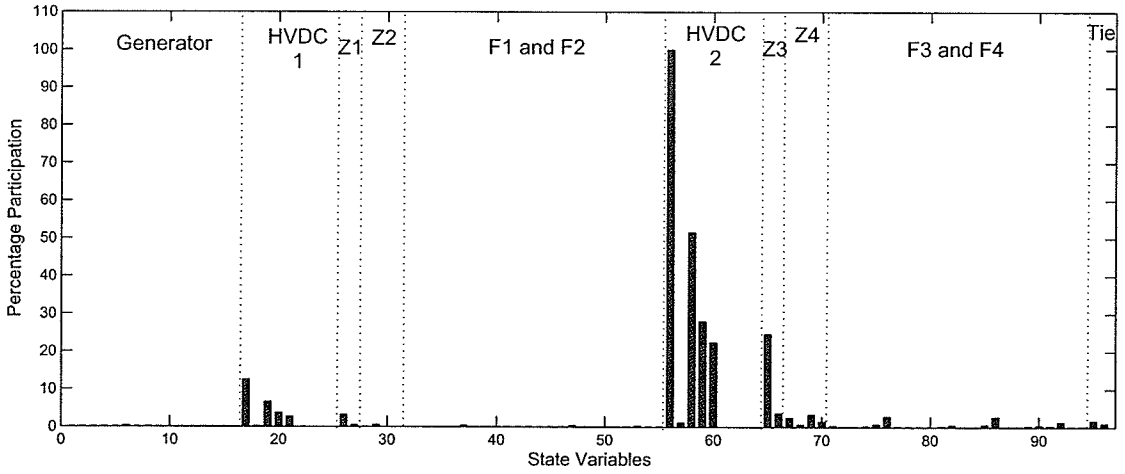

Figure 5.6: Participation of state variables in the similar mode corresponding to mode 9 (Table 5.1) when the tie line impedance is increased by 5 times

contributions are further analyzed by changing the rectifier PI controller input gain (G) of HVDC1 in the range of 0.2 to 10. The polar plot of modes 6 to 10 are given in Figure 5.7. The frequency and damping of Mode 6 (a DC resonance mode) show minor changes when the gain is changed. In modes 7,8 and 9, the frequency and

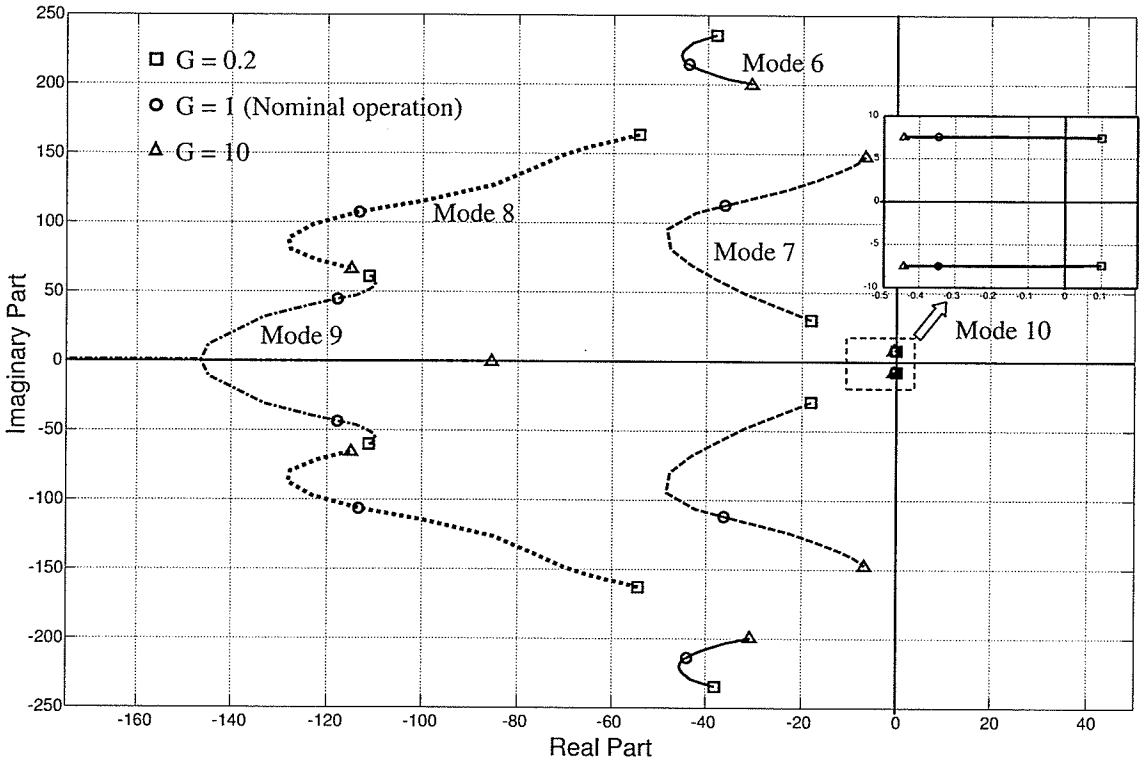

Figure 5.7: Polar plot of modes 6,7,8,9 and 10 - HVDC1 rectifier PI controller input gain is changed from 0.2 to 10

damping change in a wide range. For example, Mode 7 has around 5% damping when the gain is 10. Mode 9 becomes aperiodic as the gain increases to 1.3.

Especially, the electro-mechanical mode (Mode 10) becomes unstable as the gain decreases to 0.2. This instability can be seen in the comparisons of small signal model results and PSCAD/EMTDC results shown in Figure 5.8. This comparison further confirms the accuracy of the small signal model in predicting small signal stability of the system.

This analysis shows that the current controller action affects the performance of the electromechanical mode. This gives an indication that the damping of some electromechanical oscillations can be controlled through HVDC. This controlling mechanism is briefly described in the following section.

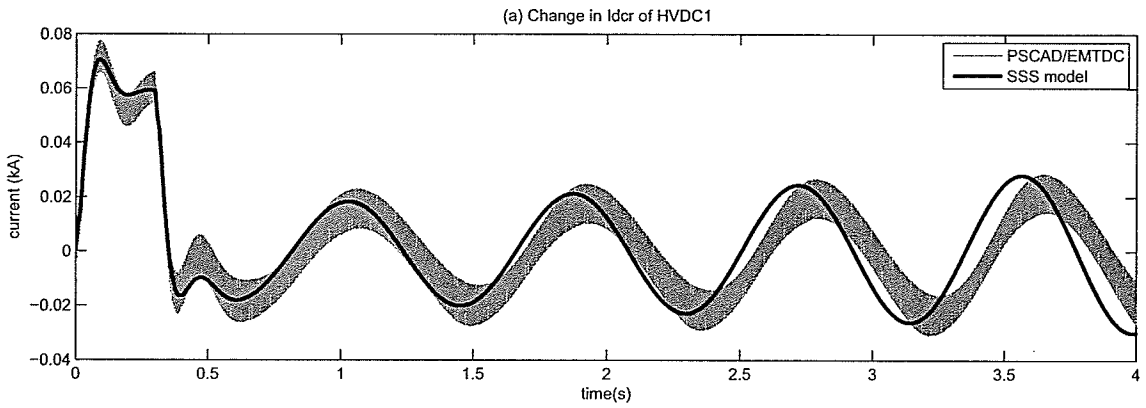

Figure 5.8: Change in rectifier side DC current of HVDC1 for a 5%, 0.3s step on the current controller input in HVDC1, when the HVDC1 rectifier PI controller input gain is 0.2

5.2.7 HVDC Controllers For Electromechanical Oscillations

The damping of some local and inter-area modes of the power systems can be controlled through the HVDC. These controllers are called HVDC damping controllers or HVDC modulation controllers and the implementation aspects have been readily discussed in the literature [6][4][43].

The damping controller can be applied at the rectifier current controller (current modulation) or at the inverter extinction angle controller as an auxiliary controller. For example, the rectifier damping controller modifies the current reference such that the damping of some electromechanical modes are improved. A remote signal (eg: rotor speed of a generator) or a local signal can be used as the input. According to [4], the frequency deviations of the converter terminals can be used as a local input.

For the completeness of the analysis, the designing aspects of the HVDC damping controller to improve the damping of Mode 10 are briefly discussed. The generator rotor speed is used as the input. The communication delays between the generator station and the converter station are ignored.

The controller is attached at the current reference of the rectifier current controller. The same procedure, which is followed to tune power system stabilizers (PSS) [44] can be employed to design the damping controller as well. The phase lag between the rectifier current controller input and the generator electrical torque is obtained from the frequency response analysis while keeping the generator rotor locked. It is found that the phase lag is 175^o. This phase lag has to be compensated using a phase lead block. Since the phase lag is close to 180^o, the inverted signal of the controller output can be added to the current reference without using a lead-lag block. Therefore, only a washout filter and a gain block are used as the damping controller and the controller output is subtracted from the current reference.

When the controller gain is 50 and the washout filter time constant is 5s, the damping of the electromechanical mode (Mode 10) improves to 40%. The changes in the rotor speed are compared in Figure 5.9, for a 5%, 0.3s step change on the current controller input of HVDC1. The stability enhancement of the generator can be observed clearly in Figure 5.9. In addition to that, this demonstrate the accuracy of the small signal model in designing controllers. It is important to track the damping of the other modes in the system while changing the damping controller gain to improve the generator stability. However, for the given controller parameters, the damping of the DC line resonance modes and the controller modes does not change much from the values given in Table 5.1.

5.2.8 Summary of Analysis

The analysis shows that the rectifier current controllers and the DC lines significantly contribute to the multi-HVDC interactions. The inverter extinction angle controller does not participate significantly in these modes. Although the HVDC systems are

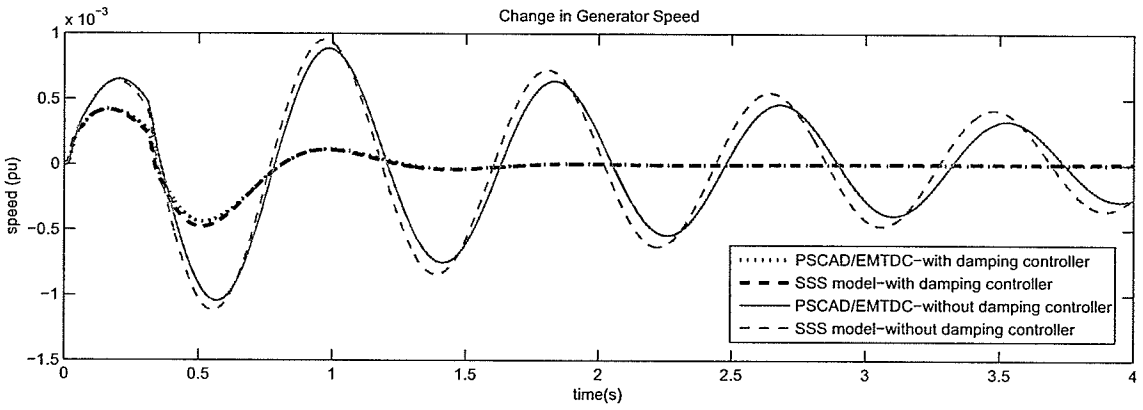

Figure 5.9: Change in generator speed for a 5%, 0.3s step on the current controller input in HVDC1, when the HVDC damping controller gain is 50.

identical, the network is not symmetrical. HVDC1 is electrically closer to the synchronous generator than HVDC2 because of the tie line. Therefore, the modes associated with the two HVDC systems are different. The strong tie line makes both of the HVDC systems to participate in these modes. The interactions between HVDC1 and HVDC2 diminish as the tie line impedance increases. The rectifier current controller action influences the behavior of the HVDC associated modes and the electromechanical modes. Especially, HVDC damping controllers can be used to improve the damping of the electromechanical modes.

In this case study, the HVDC interactions were analyzed for a simple test system in which the entire AC network was modeled using the dynamic network model. However, for a large power system, the entire network dynamics cannot be modeled and the proposed hybrid AC network model has to be used. The following study (Case Study-2) demonstrate the abilities of the hybrid model in analyzing the HVDC interactions.

5.3 Case Study-2:

HVDC Interactions in Large Power Systems

In this study, the HVDC interactions are analyzed in a larger power system using the hybrid model. Especially, the modal analysis results are compared with the conventional model (Y matrix representation of AC network) and the detail model, which includes the AC network dynamics of the entire network. This will demonstrate the accuracy of the proposed hybrid model in analyzing HVDC interactions.

The modified New England 39 bus test system shown in Figure 3.2 of Chapter 3 is used to analyze the interactions. The three small signal models described in Section 3.3.1 are used for the comparisons of the results. For the clarity of the readers, the models are redescribed below.

Model-1: Conventional Model [admittance matrix representation for AC network and standard dynamic model of synchronous machine used in stability studies]

Model-2: Small signal model including network dynamics of entire network [dynamic phasor representation for AC network and synchronous machine models including stator winding differential equations]

Model-3: *Proposed Hybrid Model* [the area highlighted in Figure 3.2 is modeled including network dynamics (as in Model-2) and the rest is modeled using conventional model (Model-1)]

The modes and modal characteristics are analyzed using small signal stability assessment as done in Case Study-1. Some of the modes are analyzed in the following sections.

Table 5.2: HVDC Interaction Modes of Test System

#	Model-1		Model-2		Model-3	
	f (Hz)	D (%)	f (Hz)	D (%)	f (Hz)	D (%)
Mode-a	37.4	11.2%	30.9	6.7%	31.7	6.2%
Mode-b	37.1	19.7%	33.1	13.3%	33.1	13.4%

5.3.1 HVDC Interaction Modes

The oscillatory modes associated with HVDC systems are tabulated in Table 5.2. There are two DC line resonance modes in which the DC line currents and the voltages participate the most.

The participations of the HVDC1 and HVDC2 state variables in Mode-a and Mode-b are illustrated in Figure 5.10 and Figure 5.11 respectively. The first 9 state variables belong to HVDC1 and the rest belong to HVDC2. The state variables in each HVDC system are arranged in the order of [$X_{\alpha r}$, $X_{\alpha i}$, I_{dcr}, I_{dci}, V_{cap} and four PLO variables]. The phase angles of the mode shapes of Mode-a and Mode-b are illustrated in Figure 5.12. The phasors "1a to 1e" represent the state variables of HVDC1 in the order of [$X_{\alpha r}$, $X_{\alpha i}$, I_{dcr}, I_{dci}, V_{cap}] and the phasors "2a to 2e" represent the same state variables of HVDC2.

Comparisons

Model-2 which includes the AC network dynamics of entire network can be used as a benchmark to analyze the interactions. Model-2 gives Mode-a at 30.9 Hz with 6.7% damping (Table 5.2). The mid-point DC voltage (100%) and the inverter side DC current (100%) of HVDC1 participate the most in this mode (Figure 5.10). There are significant contributions of the mid-point DC voltage (80%) and the inverter side DC current (80%) of HVDC2 as well. The mode shapes of Mode-a illustrated

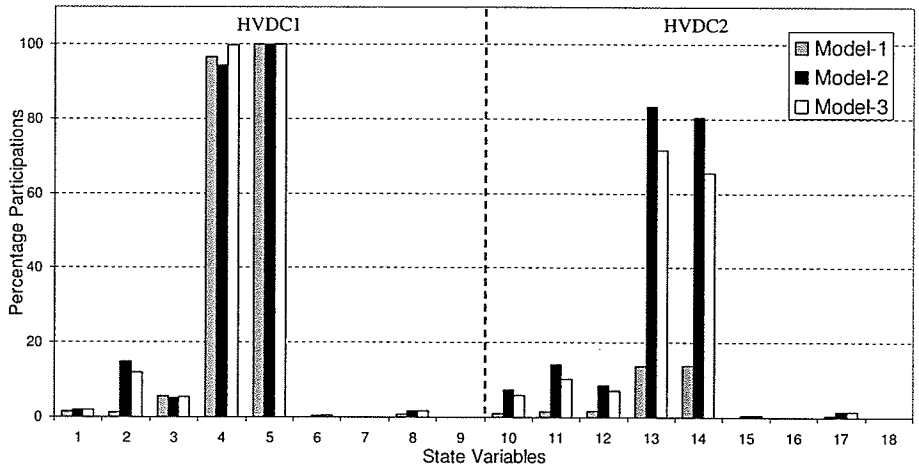

Figure 5.10: Participations of HVDC1 and HVDC2 state variables in Mode-a

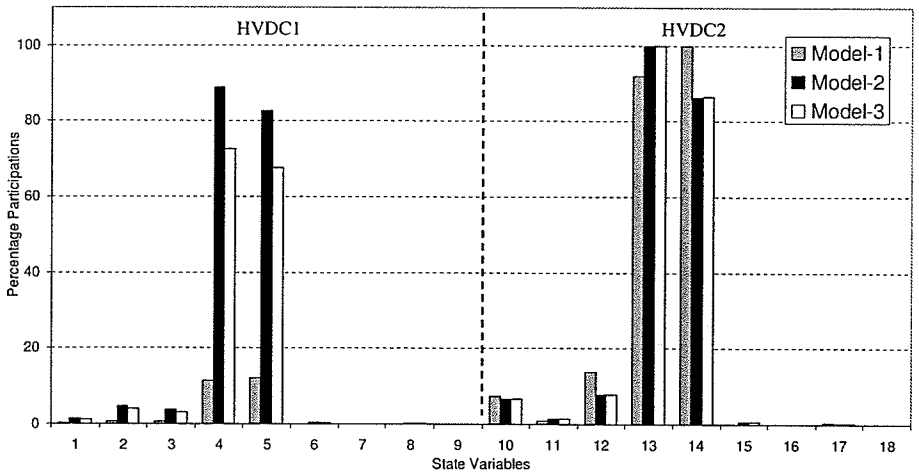

Figure 5.11: Participations of HVDC1 and HVDC2 state variables in Mode-b

in Figure 5.12 show that the angle between the relevant state variables of HVDC1 and HVDC2 is small. For example, the angle between the mid-point DC voltage of HVDC1 ("1e") and the mid-point DC voltage of HVDC2 ("2e") is around 20°. Therefore, the relevant state variables of HVDC1 and HVDC2 oscillate together in this mode. According to Model-2, Mode-b is at 33.1 Hz with 13.3% damping. HVDC2 is the highest participant in this mode (Figure 5.11). The inverter side DC current

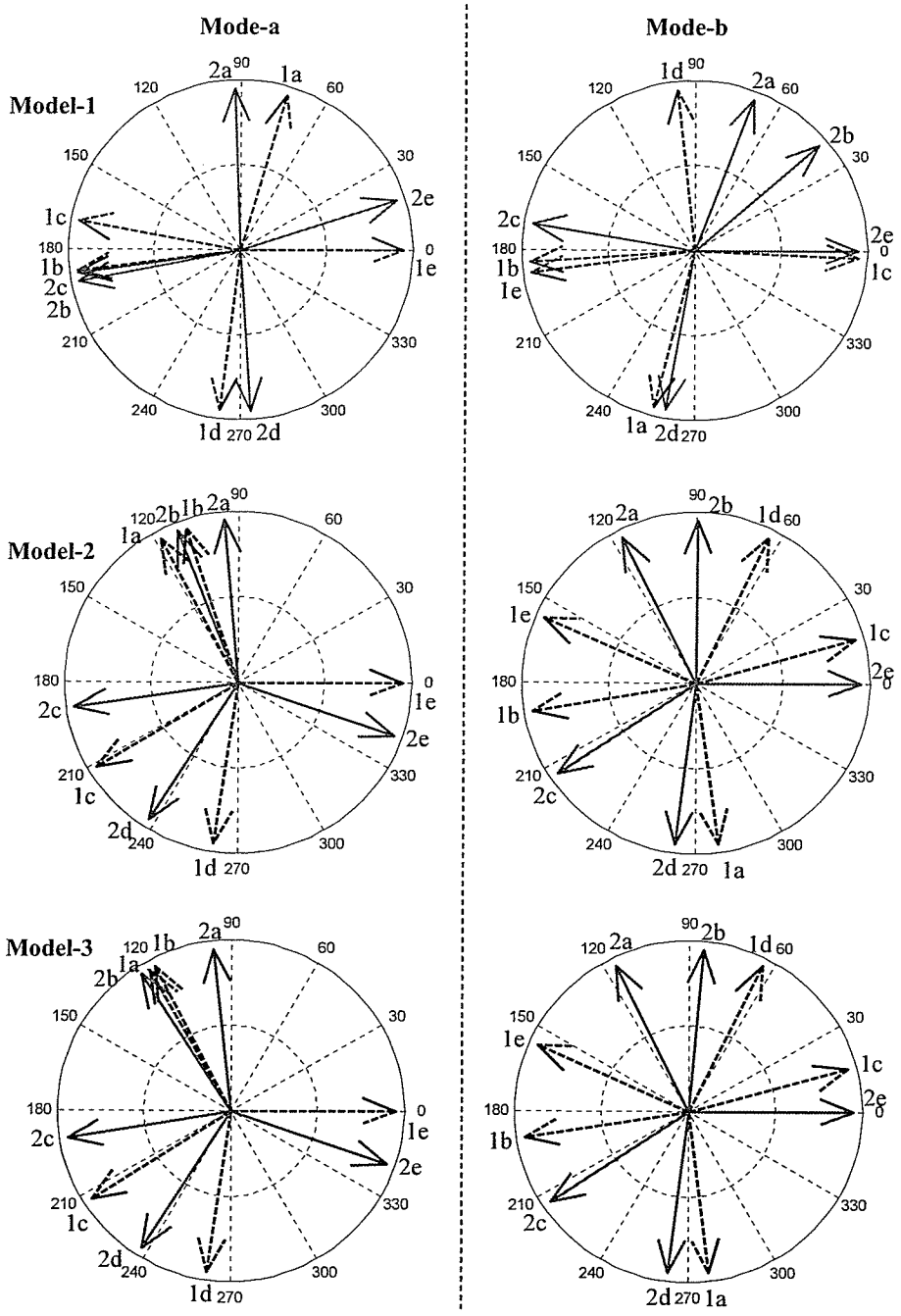

Figure 5.12: Modeshapes of HVDC interaction modes

(100%) and the mid-point DC voltage (90%) participate the most. The inverter side DC current (90%) and the mid-point DC voltage (80%) of HVDC1 also participate

in this mode. The mode shapes (Figure 5.12) show that the relevant state variables of HVDC1 and HVDC2 are almost 180^o out of phase with each other. Therefore, the relevant state variables of HVDC1 and HVDC2 oscillate against each other in this mode.

The frequencies and the damping of Mode-a and Mode-b obtained using conventional model (Model-1) are significantly different from those of Model-2 (Table 5.2). Much higher differences can be observed in the participations. For example, in Mode-a, Model-1 shows that participations of the mid-point DC voltage and the inverter side DC current of HVDC1 are 10%. However, the correct participations given by Model-2 are around 80% (Figure 5.10). Some considerable changes of the mode shapes can also be noticed in Model-1 compared to Model-2 (Figure 5.12).

The proposed hybrid model (Model-3) gives close results to those of Model-2. The frequencies and the damping of Mode-a and Mode-b are closely matched with Model-2 (Table 5.2). The participations also show close matches. For example, in Mode-a, participations of the mid-point DC voltage and the inverter side DC current of HVDC1 and HVDC2 are (100%, 100%) and (70%, 70%). These values match well with the values found using Model-2. The accuracy of the proposed model can be further verified by observing the mode shapes (Figure 5.12). Model-2 and Model-3 show similar mode shapes for the HVDC interaction modes. The conventional model (Model-1) results are much different from those results.

5.3.2 Electromechanical Modes

The electromechanical modes of the system are tabulated in Table 5.3. All the small signal stability models give similar results for the frequency and the damping of the modes. The participation factors and the mode shapes also show the same results.

Table 5.3: Electromechanical Modes of Test System

#	Model-1		Model-2		Model-3		Generator
	f (Hz)	D(%)	f (Hz)	D(%)	f (Hz)	D(%)	Participation
mode-1	1.51	5.8	1.51	5.8	1.51	5.8	30,37
mode-2	1.27	4.9	1.27	5.0	1.27	5.0	37,30,39
mode-3	1.19	5.3	1.19	5.3	1.19	5.3	32,31
mode-4	1.17	6.2	1.17	6.2	1.17	6.2	33,34
mode-5	1.09	4.8	1.09	4.9	1.09	4.8	39,31,32
mode-6	0.91	5.5	0.91	5.6	0.91	5.6	34,33-39,31
mode-7	0.48	4.1	0.47	4.5	0.47	4.3	All

Modes 1 to 5 are local oscillatory modes, in which some generators oscillate against some other generators in the same area. Mode-6 is an inter-area mode, in which generators 33 and 34 oscillate against generators 31 and 39. In mode-7, all the generators in the system oscillate together.

5.3.3 Summary of Analysis

The proposed hybrid model and the other two models have been compared against each other in the frequency domain using modal analysis. All three models produce similar modal information for low frequency electromechanical oscillation modes. However, for the high frequency HVDC interactions, the conventional model (Model-1) does not produce correct modal information produced by Model-2, in which the entire network is modeled with its dynamics. The proposed hybrid model (Model-3) produces modal information consistent with Model-2.

5.4 Concluding Remarks

Multi-in-feed HVDC interactions have been analyzed using the eigenvalues and eigenvectors obtained from the linearized state space model. This analysis has shown that

there are several modes where the state variables associated with HVDC converter terminals interact with each other. The rectifier current controllers and the DC line state variables participate the most in these modes. If the HVDC in-feeds are tightly connected in the AC side, they strongly interact with each other. These interactions diminish as the resultant AC impedance between HVDC terminals is increased. Further, the rectifier current controller gain affects the HVDC interaction modes and the electromechanical modes. Especially, the stability of some of the electromechanical modes can be improved using an auxiliary controller attached to the rectifier current controller.

In Case Study-2, the proposed hybrid model has been employed to analyze the HVDC interactions. The analysis has shown that the proposed hybrid model produces modal information consistent with the detailed model, in which the entire network is modeled including dynamics. Unlike the detailed model, the hybrid model can be used to model large power systems efficiently. Therefore, the proposed hybrid model can be used to analyze high frequency interactions of the HVDC systems as well as electromechanical oscillations of large power systems.

Chapter 6

HVDC-Generator-Turbine Torsional Interactions

6.1 Introduction

Small signal stability assessment techniques described in Chapter 4 can be employed to analyze subsynchronous oscillations in generator-turbine units [15]. When linearized models are used to study the damping of low frequency electromechanical oscillations in power systems, the transmission network is modeled using the bus admittance matrix and the generator stator winding dynamics are ignored. However, the frequencies associated with torsional oscillations are much higher than those of electromechanical oscillations. Therefore, simplified network models and generator models are not adequate. The dynamic representation of the transmission network and the modeling of stator dynamics of the generators described in Chapter 2 are required to analyze torsional interactions accurately. In Appendix E, these modeling techniques are used to analyze the generator-turbine torsional interactions with the AC network in the IEEE first benchmark model [39].

HVDC systems can also interact with the torsional oscillations of the generator-turbine units, if they are tightly coupled in the AC system [7][8][9]. These interactions may occur between the rectifier current/power controller and the multi-mass rotor-turbine systems of the generators and they may even lead to the torsional instabilities. These HVDC-generator turbine torsional interactions are investigated in this chapter using a simple test system. Small signal stability assessment is used for the analysis and the validations are carried out using the EMT simulations. The investigations are extended to larger power systems in the latter part, using the hybrid small signal stability model described in Chapter 3.

6.2 HVDC-Generator-Turbine Torsional Interactions Analysis Using a Small Test System

The CIGRE benchmark HVDC test system [27] with some modifications is used to analyze subsynchronous oscillations. The test system is shown in Figure 6.1. A synchronous generator is connected at the rectifier side AC bus to supply half of the P-Q requirement of the rectifier. The generator-turbine parameters are as given in the IEEE first benchmark model for computer simulation of subsynchronous resonance [39]. Since a static exciter is used, the exciter mass is not included in the analysis. The effective short circuit ratios (ESCR) without the synchronous generator are kept around 4.4 at the rectifier and the inverter ends.

6.2.1 Linearized Model

The linearized model is obtained as described in Chapter 2. Following details are included in the linearized model.

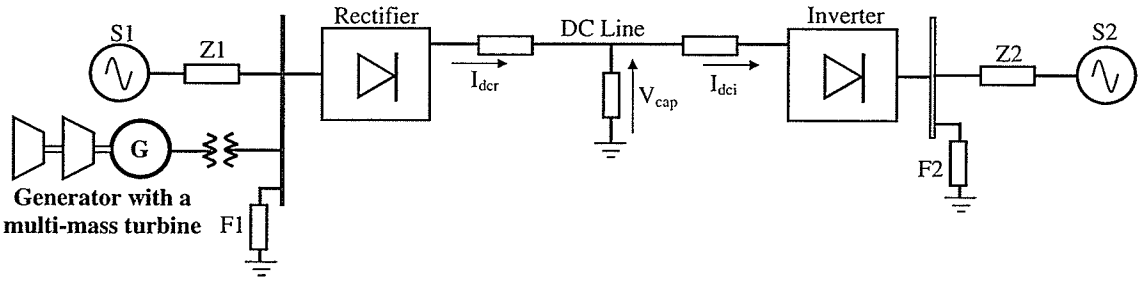

Figure 6.1: Test system used to analyze HVDC-generator turbine interactions

- Synchronous generator model including stator dynamics (8^{th} order) is used. An exciter model (AC4A) is also included with the generator model.
- A four-mass turbine model (HP, IP, LPA and LPB) as described in [39].
- HVDC system with linearized converter models, DC transmission system, rectifier current controller and inverter extinction angle controller are used.
- The dynamic AC network model is used.

The accuracy of the linearized models are evaluated using time domain simulations. Small perturbation simulations obtained using the linearized model are compared with EMT simulation results obtained using PSCAD/EMTDC.

A pulse of magnitude of +10% and duration of 10ms was applied to the rectifier current controller input. The change in rectifier side DC current is shown in Figure 6.2. All the high frequency oscillations except higher order system harmonics match with the PSCAD/EMTDC results. Figure 6.3 shows changes in the generator speed. Small signal model results show a close match with the PSCAD/EMTDC results for the subsynchronous frequencies embedded in the generator speed. These comparisons verify that the linearized model with the level of details considered above accurately represents the subsynchronous oscillations in the system. Therefore, the linear state

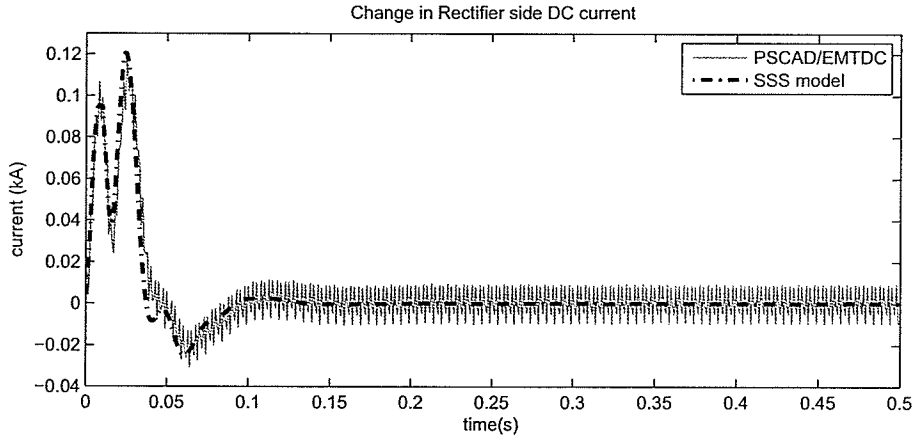

Figure 6.2: Changes in rectifier side DC currents for a 10%, 10ms pulse on the rectifier current controller input

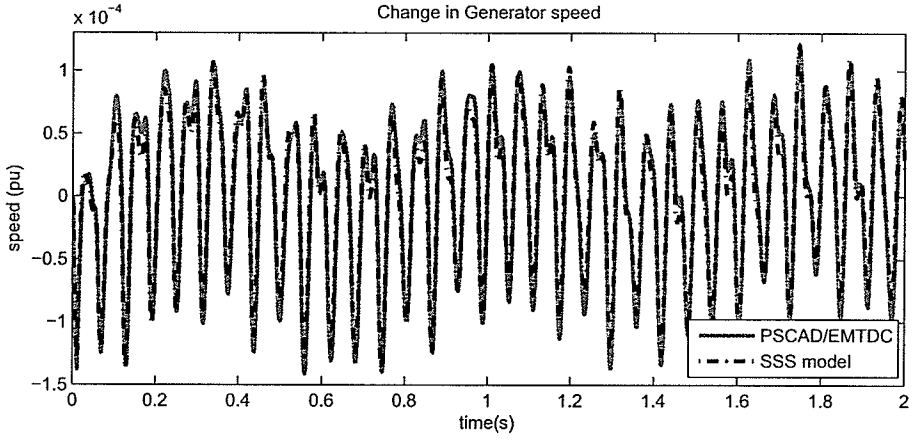

Figure 6.3: Changes in generator rotor speed (in pu) for a 10%, 10ms pulse on the rectifier current controller

space model can be used to analyze these oscillations using small signal stability assessment.

6.2.2 Modal Analysis of Test System

The small signal model of the test system consists of 60 state variables: generator-turbine system (19), HVDC system (9) and AC network including filters (32). Some

important modes obtained under nominal operating conditions are shown in Table 6.1. The generator-turbine system shows 4 torsional oscillation modes (Modes 1 to 4). The frequencies of oscillations are 16.33, 25.6, 32.53 and 47.46Hz respectively. Although the mechanical damping of multi-mass system is ignored, these modes show very low damping caused by the electrical torque. The participation factors and the phase angles of the mode shapes of the multi-mass speed terms (ω_{gen}, ω_{LPB}, ω_{LPA}, ω_{IP}, ω_{HP}) in these torsional modes are shown in Table 6.2. The participation of the highest participant is considered as 100% and the angle of the mode shape of the highest participant is considered as the reference (0^o).

All the mass units participate in Mode-1, in which the generator mass is the main participant. Mode shapes show that the generator and LPB masses oscillate against the other three turbine masses in this mode. The HP turbine is the main participant of Mode-2 and all other mass units also contribute to this mode. LPA and LPB turbines oscillate against the generator and IP and HP turbines in this mode. The LPB turbine oscillates against the generator and LPA turbine in Mode-3. HP and IP turbine participations in this mode are minor. Mode-4 shows the interactions of IP and HP turbines. IP turbine oscillate against HP turbine in this mode. The LPB turbine and the generator do not contribute to this mode. It is noticed that there are no significant participations of the state variables of the HVDC system in these torsional modes under the given conditions.

Mode 5 and 6 in Table 6.1 show the interactions of the HVDC system. The rectifier current controller state variable and the DC line state variables participate the most in these modes. There are some minor participations of the generator speed as well. These modes are also in subsynchronous frequency range (10.33 and 42.32Hz). However, these modes are well damped.

Table 6.1: Some important modes of the test system

Mode	Freq. (Hz)	D (%)	Major Participant
1	16.33	0.0781	Gen-Turbine (SSO)
2	25.60	0.00975	Gen-Turbine (SSO)
3	32.53	0.0102	Gen-Turbine (SSO)
4	47.46	0.000003	Gen-Turbine (SSO)
5	10.33	51.9	Rectifier Current Controller
6	42.32	22.7	DC line
7	1.36	3.2	Generator (Electromechanical)

Table 6.2: Participations and mode shapes of multi-mass speed terms in torsional modes

Mode	Participations (%) and Mode shapes (Deg.)				
	ω_{gen}	ω_{LPB}	ω_{LPA}	ω_{IP}	ω_{HP}
1	**100**∠0	**16**∠0	**70**∠180	**43**∠180	**48**∠180
2	**25**∠0	**8**∠180	**50**∠180	**20**∠0	**100**∠0
3	**41**∠180	**100**∠0	**23**∠180	**0**∠180	**7**∠0
4	**0**∠180	**0**∠0	**7**∠180	**100**∠0	**37**∠180

The electromechanical mode of the system is given by Mode 7. The frequency of oscillation is 1.36Hz and the mode has 3.2% damping.

6.2.3 HVDC-Generator-Turbine Torsional Interactions

Under the given conditions, the test system does not show any interactions between the HVDC system and generator-turbine system. However, there might be some interactions if the operating conditions are changed or the controller parameters are changed. In order to demonstrate this, the analysis was carried out by changing the rectifier current controller proportional and integral gains. It was observed that, if there is a slightly damped HVDC controller mode, in which the frequency is close to a torsional mode of the generator-turbine system, the two systems interact strongly even causing instabilities. When the rectifier current controller proportional gain is

Table 6.3: Participating modes in torsional interactions when controller gains are adjusted

Mode	Freq. (Hz)	D (%)	Major Participants
A	16.24	-0.03	HVDC-Generator-Turbine
B	16.36	1.05	HVDC-Generator-Turbine

0.11 and the integral time constant is 0.0045s, the controller mode (Mode 5) gets close to Mode 1 (torsional mode) in frequency and the resultant torsional mode becomes unstable. The resultant modes close to Mode 1 are shown in Table 6.3. The participation factors (%) of multi-mass speed terms (ω_{gen}, ω_{LPB}, ω_{LPA}, ω_{IP}, ω_{HP}) and HVDC state variables [rectifier current controller state variable ($X_{\alpha,r}$), inverter extinction angle controller state variable ($X_{\alpha,i}$), rectifier side DC current (I_{dcr}), inverter side DC current (I_{dci}) and midpoint capacitor voltage (V_{cap})] in these modes are illustrated in Figure 6.4.

Mode-A is negatively damped and the frequency is at 16.24 Hz. The state variables of the generator-turbine system and the HVDC system strongly interact with each other in this mode (Figure 6.4). The HVDC system state variables: $X_{\alpha,r}$(100%), I_{dci}(60%) and I_{dcr}(30%) and the generator-turbine system state variables: ω_{gen}(70%), ω_{LPA}(50%), ω_{IP}(30%) and ω_{HP}(30%) are the major participants.

The HVDC state variables participate the most in slightly damped Mode-B (Figure 6.4). The frequency is at 16.36 Hz and the damping is 1.05 %. The HVDC system state variables: $X_{\alpha,r}$(100%), I_{dci}(60%) and I_{dcr}(30%) are the major participants. There are some participations of the multi-mass speed terms as well [ω_{gen}(20%) and ω_{LPA}(20%)].

The comparisons of the change in rectifier side DC current and the change in generator speed for the perturbation mentioned earlier are shown in Figures 6.5 and

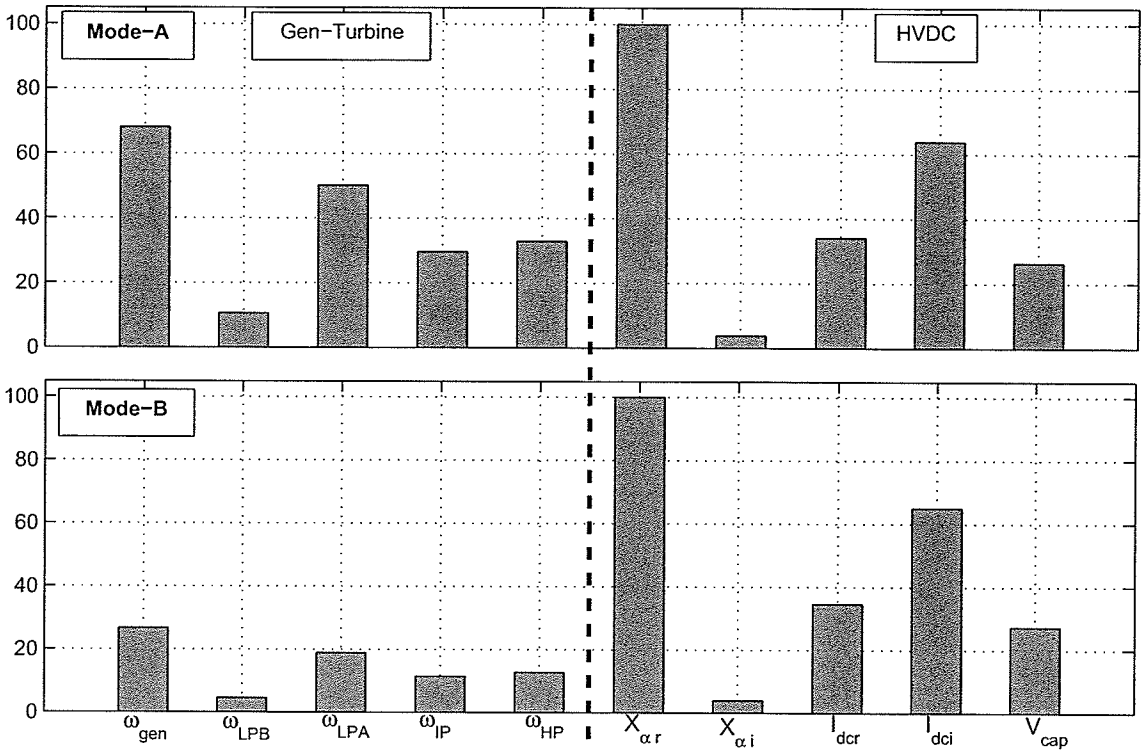

Figure 6.4: Participation factors (%) of multi-mass speed terms and HVDC state variables in Modes A and B

6.6 respectively. Mode-A can be observed in the unstable oscillations of the generator speed (Figure 6.6) and Mode-B can be observed in the rectifier side DC current (Figure 6.5). The close match with the PSCAD/EMTDC results further demonstrate the accuracy of the small signal model in identifying the torsional interactions.

If the AC network dynamics are ignored (admittance matrix model), the small signal model shows inaccurate results. In that model, Mode-A is at 16.3Hz with +0.07% damping. According to this, the torsional mode is stable. Furthermore, Mode-B is at 18.4Hz and it has +4.7% damping. These results are significantly different from the results presented in the above analysis. Therefore, the admittance matrix representation is not adequate to analyze torsional interactions accurately.

It was found using the small signal model that there is a similar torsional instability

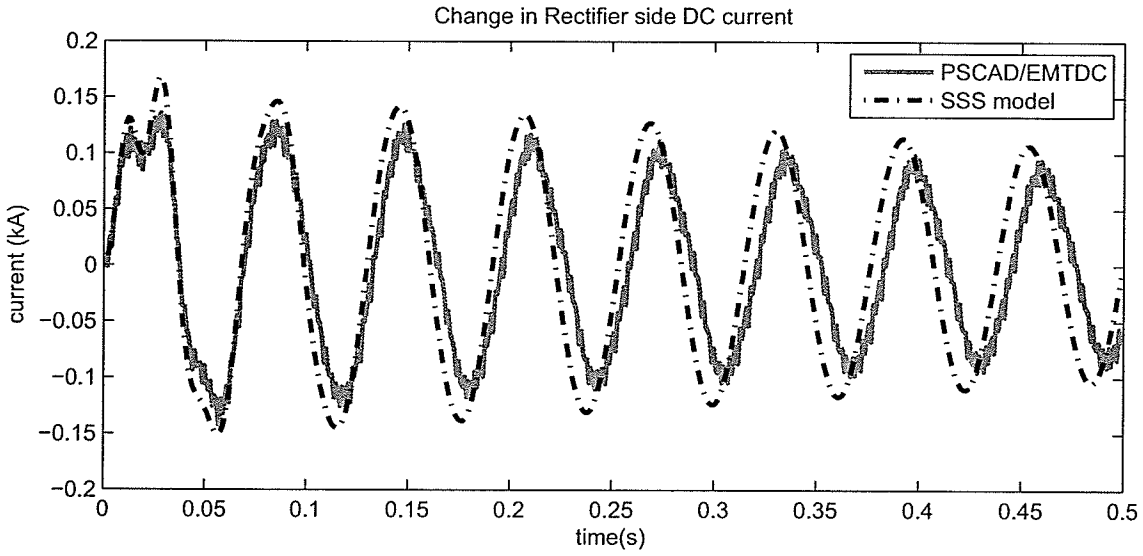

Figure 6.5: Changes in rectifier side DC currents for a 10%, 10ms pulse on the rectifier current controller input (when current controller gains are adjusted)

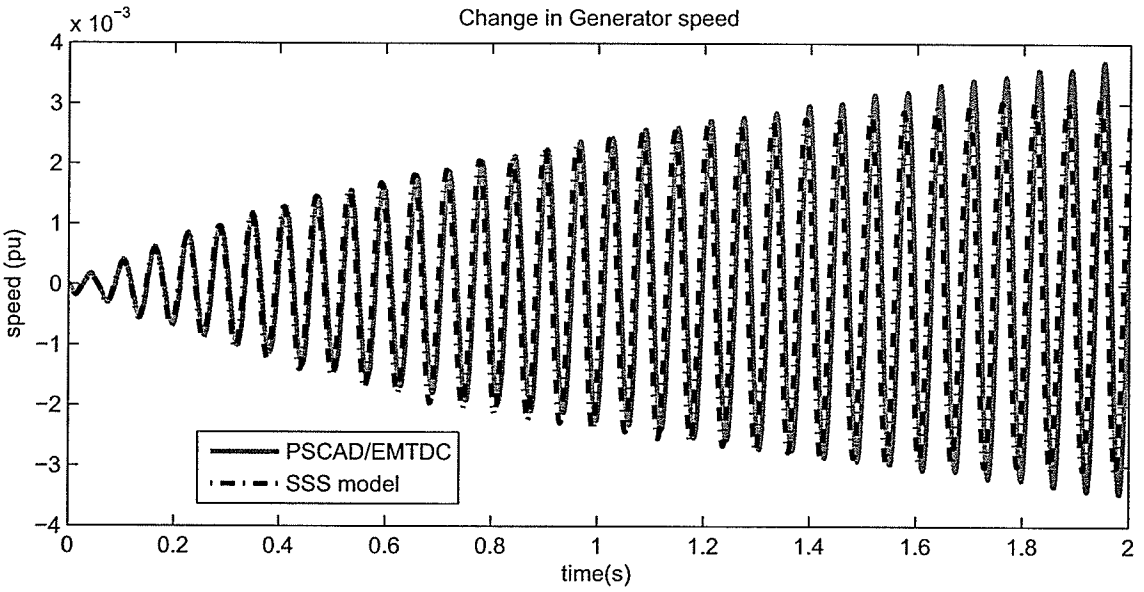

Figure 6.6: Changes in generator rotor speed (in pu) for a 10%, 10ms pulse on the rectifier current controller (when current controller gains are adjusted)

in the generator-turbine system when the rectifier current controller proportional gain is 2.8571 and the integral time constant is 0.0012s. This produces a controller mode

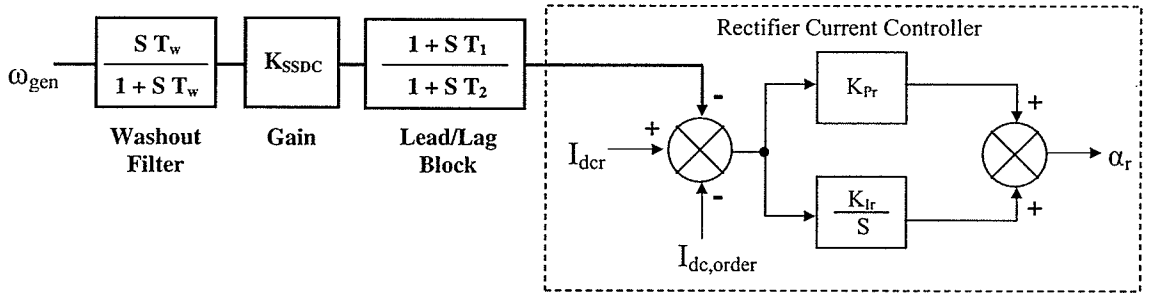

Figure 6.7: Subsynchronous damping controller attached to the rectifier current controller

close to Mode 2 ($\approx 25Hz$) and causes instability in the torsional mode.

In conclusion, the HVDC-generator-turbine interactions may happen if there is a slightly damped HVDC controller mode in which the frequency is close to a torsional frequency in the system. These conditions may even lead to torsional instabilities. The small signal stability assessment can be employed to identify the conditions for these torsional instabilities.

6.2.4 Design of SSDC Using Small Signal Stability Assessment

The same procedure, which is followed to tune power system stabilizers (PSS) [44] can be employed to design subsynchronous damping controllers (SSDCs) attached to the HVDC system. The torsional modes in the generator-turbine system can be controlled through the rectifier current controller input as shown in Figure 6.7. A lead-lag block, a gain block and a washout filter are included in the controller.

The controllability of the modes can be analyzed using the mode controllability indices as described in Chapter 4. For the above mentioned test system under nominal conditions, the magnitudes of the controllability indices obtained between four

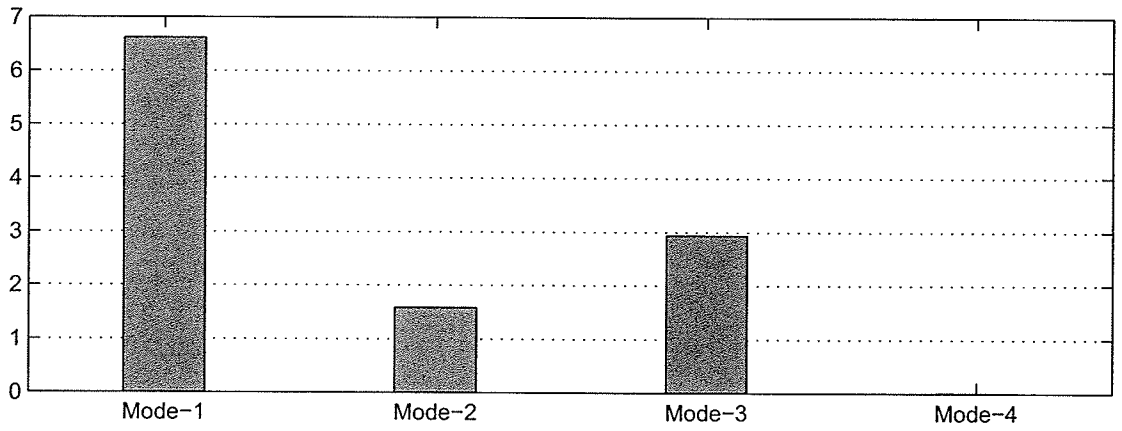

Figure 6.8: Controllability of torsional modes through rectifier current controller input

torsional modes (Table 6.1) and the current controller inputs are illustrated in Figure 6.8. Mode-1 (16.33Hz) is the most controllable mode among the torsional modes. Modes 2 and 3 are also controllable using the current controller input. However, Mode-4 (47.46Hz) cannot be controlled using the current controller input.

The first three torsional modes can be observed in the generator speed (Table 6.2) and therefore, the speed can be used as an input to the SSDC.

In order to provide positive damping at required frequency range, the SSDC should have an appropriate phase characteristic to compensate the phase lag/lead between the current controller input and the electrical torque of the generator. The frequency response for the transfer function between the current controller input and the electrical torque is obtained while keeping the generator rotor angle constant (this can be done by increasing the inertia to a very large value [44]). The phase characteristics of the test system obtained as described, is shown in Figure 6.9. The transfer function shows a phase lag of 10^o to 20^o in the range of frequencies corresponding to Modes 1, 2 and 3. At the frequency of Mode-4, the system shows a phase lead of around 50^o. We are not concerned about this mode because it is neither observable in generator

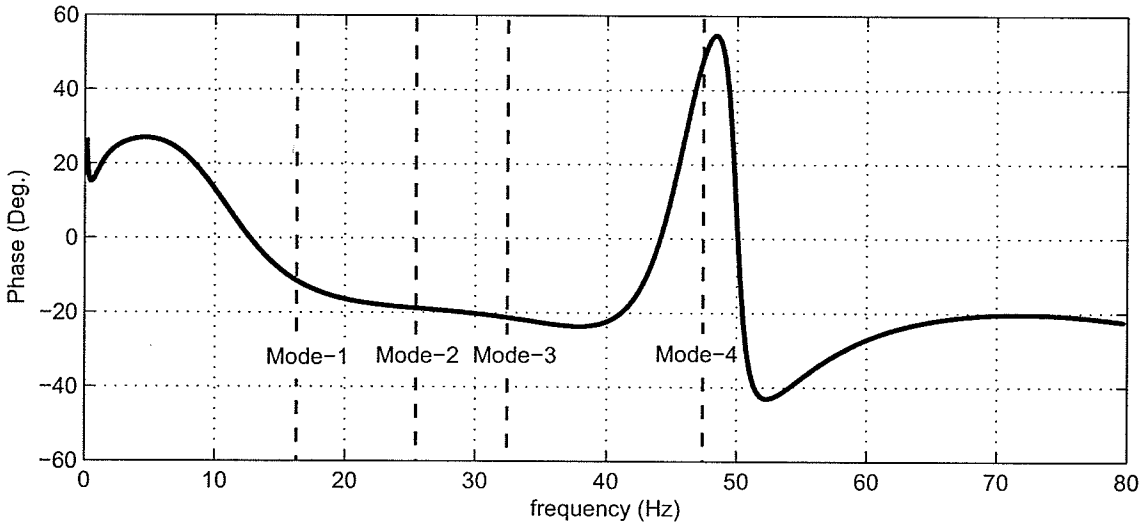

Figure 6.9: Phase plot of frequency response between generator electrical torque and rectifier current controller input

speed nor controllable through the current controller input.

One lead-lag block with a phase lead of 10^o at 25 Hz ($T_1 = 0.0076s$, $T_2 = 0.0053s$) is used to compensate the phase lag in the corresponding frequency range. A washout filter ($T_w = 20s$) is also included to block the steady (DC) changes in the speed [44].

The SSDC gain is adjusted to improve the damping of torsional modes, while keeping the damping of other modes at appropriate levels. Figure 6.10 shows the damping versus SSDC gain characteristics obtained for the torsional modes and the other modes in the range of 0 to 200 of SSDC gain. As the gain increases the damping of Mode-1 increases significantly. Around 5% damping can be obtained when the gain is 100. The damping of Modes 2 and 3 also increases as the gain increases. There is no improvement in Mode-4, since it is uncontrollable through the SSDC. The decrements in damping of HVDC system modes (Mode 5 and 6) are comparatively small and the damping factors are at acceptable levels. The SSDC helps to improve the damping of electromechanical mode (Mode-7) as well. Around 18% damping can be obtained

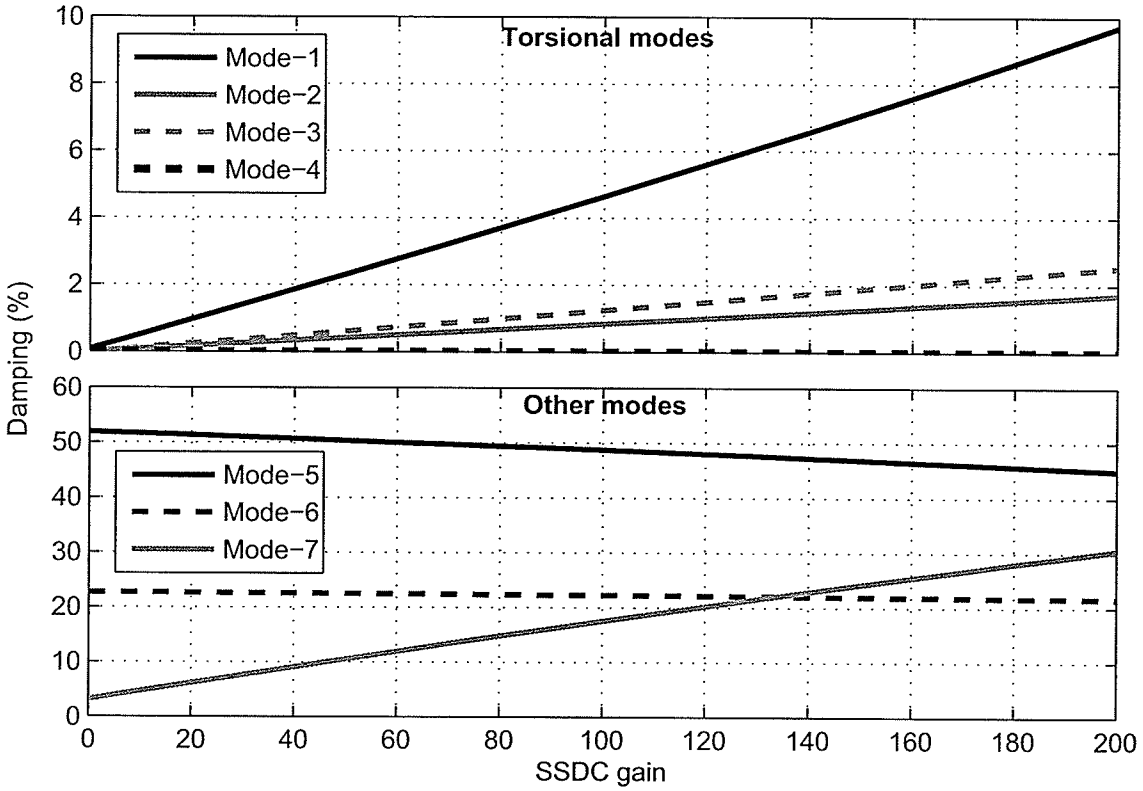

Figure 6.10: Changes in mode dampings with SSDC gain

when the gain is 100.

Based on the above observations, the SSDC gain is set at 100, in order to obtain 5% damping in the first torsional mode (Mode-1). Furthermore, this does not cause any adverse effect on the other modes. Small perturbation simulations are used to demonstrate the performance of the developed SSDC in damping the oscillations in the generator-turbine unit. For the pre-described perturbation, the changes in rectifier side DC current and the generator speed are compared in Figures 6.11 and 6.12 respectively. Some oscillations in the rectifier side DC current can be observed due to the introduction of SSDC. However, the oscillations die down fast. A good improvement in the generator speed compared to the case without SSDC (Figure 6.3) can be observed . The torsional oscillations decay within 2s when the SSDC is

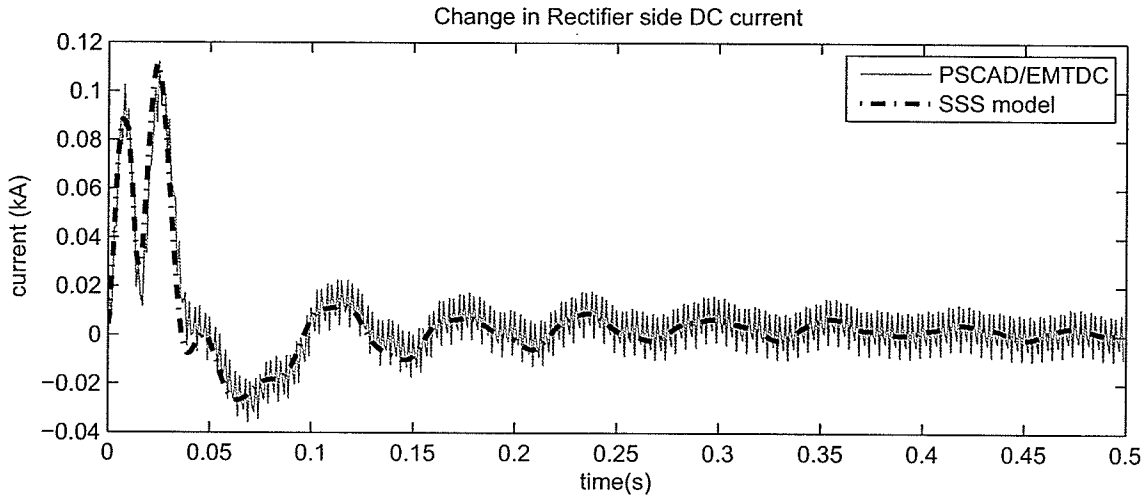

Figure 6.11: Changes in rectifier side DC currents for a 10%, 10ms pulse on the rectifier current controller input (when SSDC is connected at rectifier)

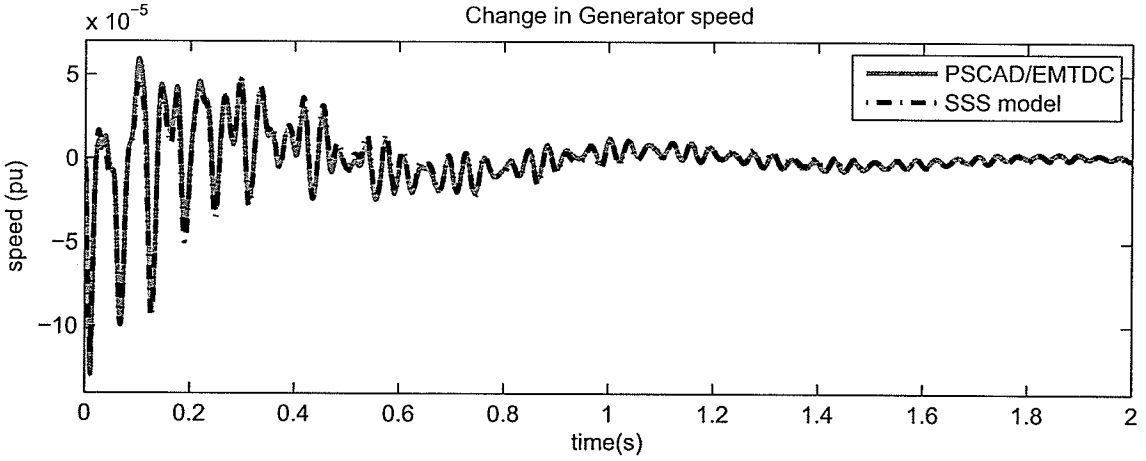

Figure 6.12: Changes in generator rotor speed (in pu) for a 10%, 10ms pulse on the rectifier current controller (when SSDC is connected at rectifier)

introduced.

The idea of this example was to demonstrate the basic concepts of designing SSDCs using small signal stability assessment. However, the performance of the SSDC has to be tested under different operating conditions such as different DC power output levels and under different transient conditions. The limits to the controller

have to be enforced accordingly.

This analysis further confirms the accuracy of the small signal model. As shown in Figures 6.11 and 6.12, the small signal model gives accurate results as in PSCAD/EMTDC. Therefore, a small signal stability model which includes the AC network dynamics and synchronous generator stator dynamics, is adequate for analyzing subsynchronous oscillations and for designing controllers to mitigate them.

6.3 HVDC-Generator-Turbine Torsional Interactions Analysis in Large Power Systems

The HVDC-generator torsional interactions in large power system can also be studies as in the above section using the hybrid small signal model proposed in Chapter 3. In this section, the New England 39 bus test system [29] with some modifications is used to demonstrate the performances of the hybrid model in analyzing torsional interactions. This test system is a modified version of the 39 bus test system used in Chapter 3 (Figure 3.2). The modified test system is shown in Figure 6.13. The generator 36 is inserted back at bus 23 instead of HVDC2. A multi-mass turbine model is attached to the generator 36. The turbine parameters are as given in the IEEE first benchmark model [39]. Note that, the HVDC infeed and the generator-turbine multi-mass unit are in the close proximity (around 35Km apart) in the test system. The test system details are given in Appendix A.

6.3.1 Modal Analysis of Test System

The hybrid small signal model of the test system consists of 195 state variables: generator-turbine multi mass system (16), HVDC system (9), AC network including

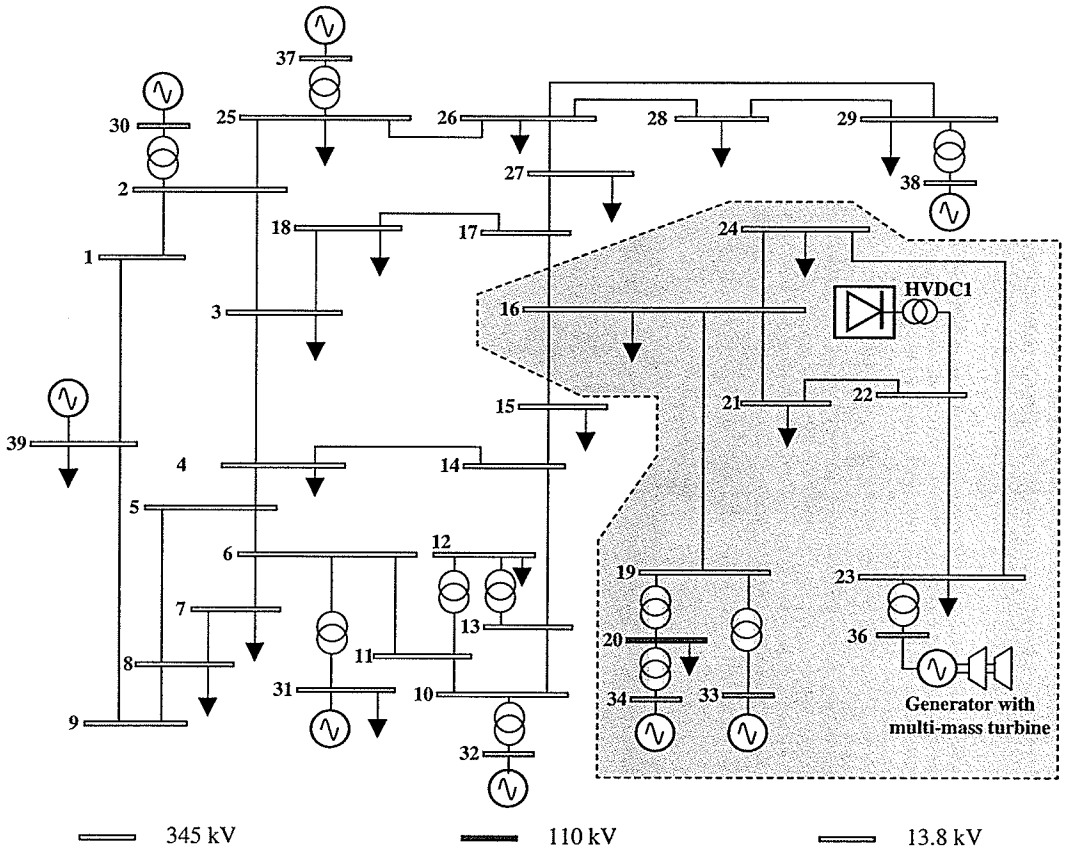

Figure 6.13: 39 bus test system used to analyze HVDC-generator turbine torsional interactions

filters (68), generators in the dynamic area (32) and the other generators in the admittance matrix model (70). Some important modes obtained under nominal operating conditions are shown in Table 6.4.

The generator-turbine system shows 4 torsional oscillation modes (Modes 1 to 4). Since the same turbine data are used, these modes are similar to the torsional modes obtained for the small test system used in Section 6.2 (Table 6.1). Mode 5 shows the DC line resonance mode of the HVDC system. Since this test system is similar to the 39 bus test system used in Chapters 3 and 5(Figure 3.2), the electromechanical modes 6, 7, 8, 9, 10, 12 and 13 are similar to those obtained in Chapter 5 (Table

Table 6.4: Some important modes of the 39 bus test system used to analyze HVDC-generator-turbine torsional interactions

Mode	frequency(Hz)	Damping (%)	Major Participants
Torsional Modes			
1	12.07	1.33e-2	Gen36,LPA,HP,IP
2	23.99	3.36e-4	HP,LPB,IP,LPA,Gen36
3	30.12	2.62e-4	LPB,LPA,HP,Gen36
4	47.46	3.11e-8	IP,HP
HVDC Interaction Modes			
5	32.59	11.19	Vcap, Idci,Idcr
Electromechanical Modes			
6	1.51	5.81	Gen 30,37
7	1.27	4.96	Gen 37,30,39
8	1.19	5.32	Gen 32,31,33
9	1.17	6.02	Gen 33,34,31,32
10	1.09	4.78	Gen 39,31,32
11	0.94	5.17	Gen 34,36,33
12	0.89	4.39	Gen 34,39,36
13	0.43	3.26	Gen 34,33,36

5.3). There are some contributions of newly introduced generator 36 in modes 12 and 13. Further, a new electromechanical mode (Mode 11) appears after introduction of generator 36. Generators 33 and 34 oscillate against generator 36 in this mode (a local mode).

6.3.2 HVDC-Generator-Turbine Torsional Interactions

Under the given conditions, the test system does not show any interactions between the HVDC system and generator-turbine system. The interactions were analyzed as in Section 6.2.3 by changing the rectifier current controller proportional and integral gains. According to the conclusions of the analysis in Section 6.2.3, the two systems might interact if there is a slightly damped HVDC controller mode in which the frequency is close to one of the torsional modes. However, this system does not

show any interaction or instability when the controller mode is close to Mode-1 or Mode-2 in frequency. There are few reasons for the two systems not to interact under these conditions. One is, the multi-mass generator-turbine unit is connected at the inverter side of the HVDC system and therefore, the generator and the rectifier current controller are electrically far apart. The other reason is, the controller modes are well damped (more than 80%) at these frequencies and therefore, these modes hardly be observed at the generator.

6.3.3 Control of Torsional Modes Through HVDC

As described in Section 6.2.4, the damping of the torsional modes can be improved through the HVDC controllers. The same procedure was followed for this test system as well. The SSDC can be added either at the rectifier current controller or at the inverter DC voltage controller in this test system. These possibilities are briefly analyzed using the hybrid small signal model in the following sections. Further, the accuracy of the analysis is demonstrated using the time domain simulation comparisons.

SSDC at Rectifier Current Controller

The SSDC at the rectifier current controller can be designed as described in Section 6.2.4. The controllability indices show that Mode-1 and Mode-2 are the most controllable torsional modes at the rectifier current controller input and Mode-3 shows a little controllability. Mode-4 cannot be controlled at that input. Since generator 36 speed participates in Mode-1, Mode-2 and Mode-3 (Table 6.4), the speed is used as the input to the SSDC. The frequency response analysis shows around 180^o phase lead between the rectifier current controller input and the generator 36 electrical torque in

the frequency range of 0-30Hz. This phase lead can be compensated using an inverted signal of the generator speed. Therefore, only a gain block is used as the SSDC for the simplicity of the analysis. However, good phase compensations and washout filters would be required for better accuracy.

When the SSDC gain (K_{SSDC}) is 400, Mode-1 shows 2.1% damping and Mode-2 damping is improved to 0.21%. Mode-3 has 0.08% damping. Mode-4 does not show any improvement. The performance of the SSDC has been evaluated in Figure 6.14. Figure 6.14(a) shows the time domain comparisons of the change in generator 36 speed for a 10%, 10ms pulse applied on the rectifier current controller input, when the SSDC is not connected. The dominating 12 Hz mode (Mode-1) can be observed in the generator speed. When the SSDC is connected at the rectifier current controller, Figure 6.14(b) shows the time domain comparisons of the change in generator 36 speed for the same disturbance. The 12 Hz mode can be observed in the first second and it decays rapidly. The low damped 30 Hz mode (Mode-3) can be observed in the latter part. The results are validated using PSCAD/EMTDC simulation results in these figures.

When designing SSDCs in large power systems, it is important to investigate the effect of SSDC on the electromechanical modes and the other modes of the system as well. In this test system, there is no significant improvement or decrement in the damping of the electromechanical modes 6, 7, 8, 9 and 10 due to the insertion of the SSDC at the rectifier current controller. The damping of the modes in which the generator 36 participates are significantly improved after insertion of the SSDC at the rectifier current controller. The damping of Mode-10 improves from 5.17% to 6.47%. Mode-11 has 12.26% damping after insertion of the SSDC. Especially, the most critical electromechanical mode (Mode-12), in which all the generators oscillate together, is

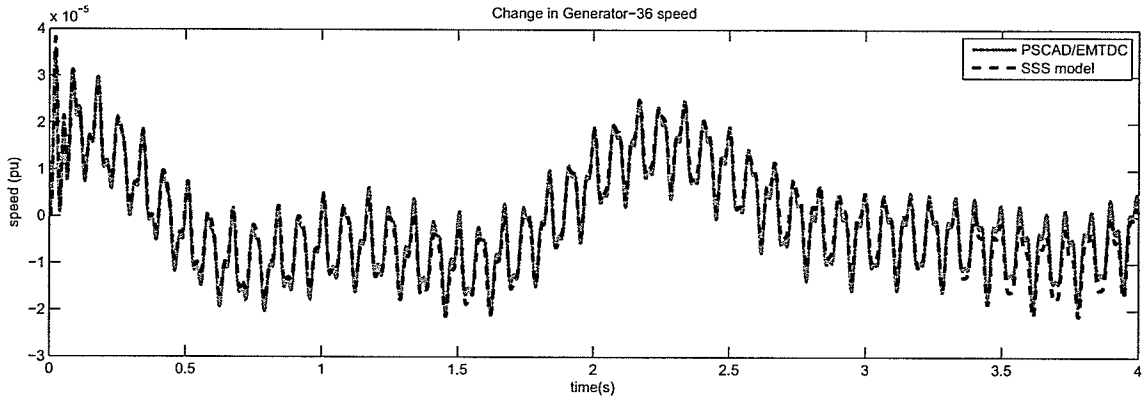

(a) Change in generator-36 speed when there is no SSDC

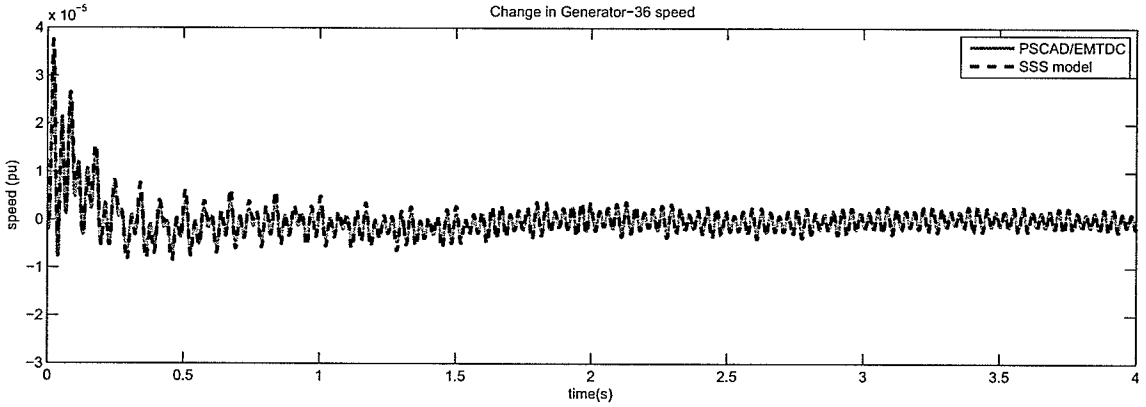

(b) Change in generator-36 speed when SSDC connected at rectifier current controller ($K_{SSDC} = 400$)

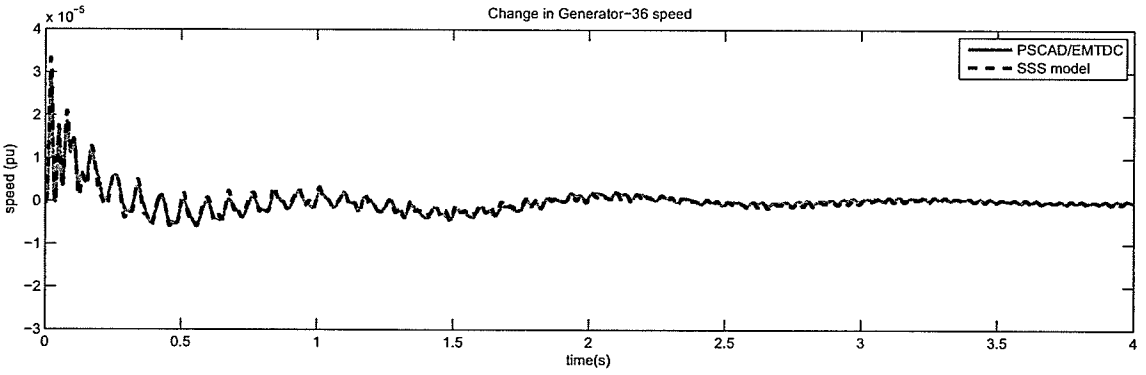

(c) Change in generator-36 speed when SSDC connected at inverter DC voltage controller ($K_{SSDC} = 400$)

Figure 6.14: Change in generator-36 speed (in pu) for a 10%, 10ms pulse on the rectifier current controller input

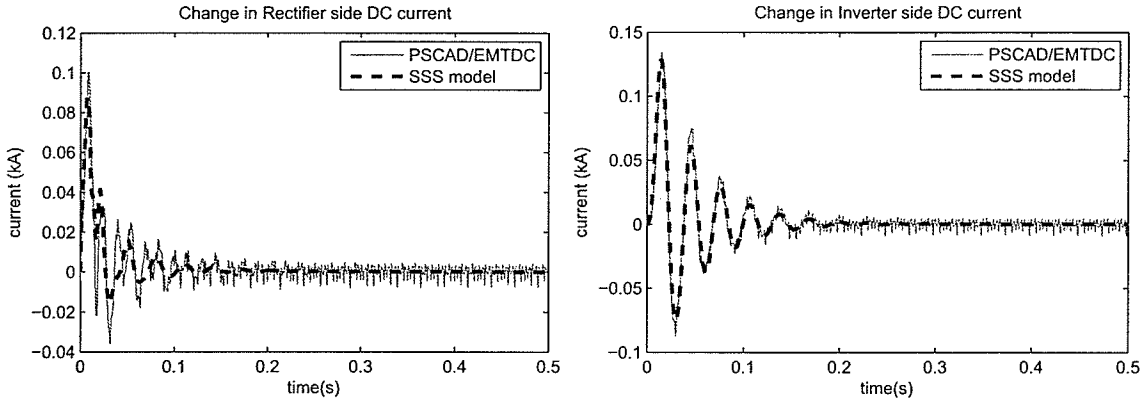

(a) Changes in DC side currents of HVDC system when there is no SSDC

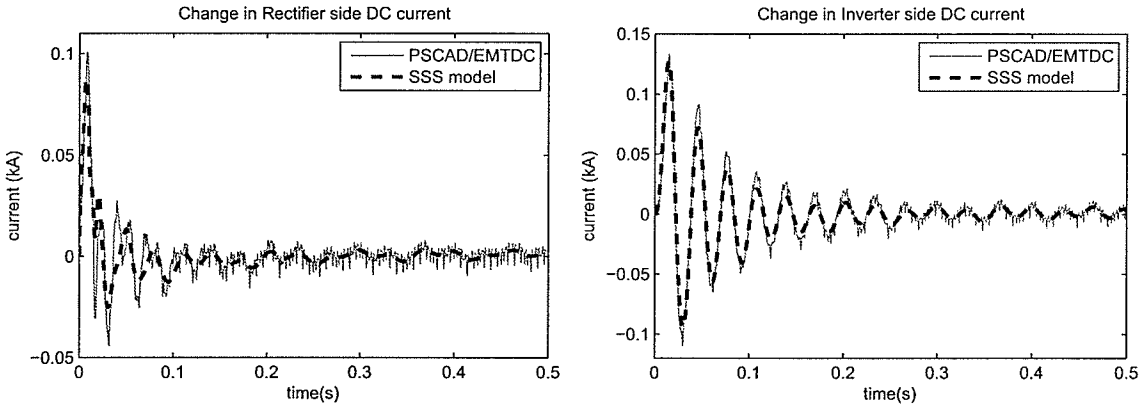

(b) Changes in DC side currents of HVDC system when SSDC connected at rectifier current controller ($K_{SSDC} = 400$)

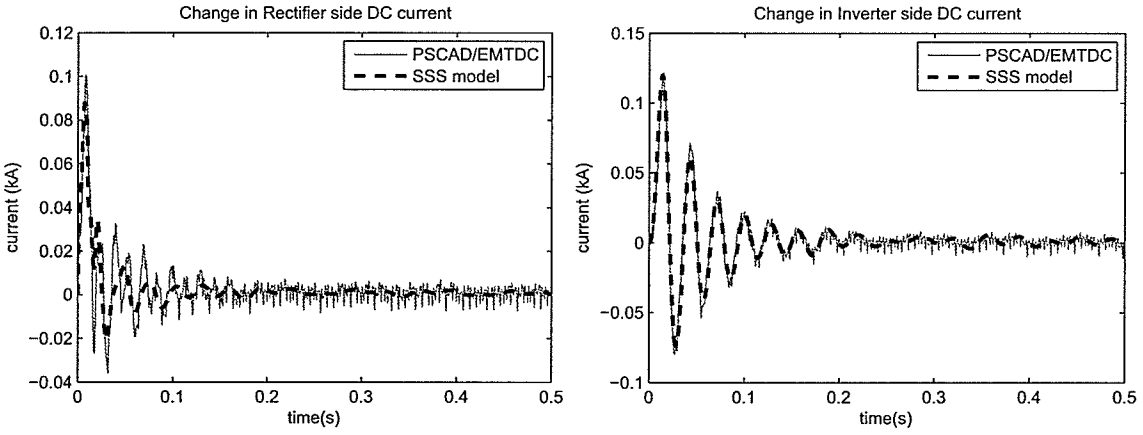

(c) Changes in DC side currents of HVDC system when SSDC connected at inverter DC voltage controller ($K_{SSDC} = 400$)

Figure 6.15: Changes in DC side currents of HVDC system for a 10%, 10ms pulse on the rectifier current controller input

largely affected and the mode becomes aperiodic as the SSDC gain increases to 400. This mode has only 3% damping before insertion of the SSDC and the resultant aperiodic modes after insertion of the SSDC are well stable (eigenvalues are close to -5). Therefore, the insertion of the SSDC at the rectifier current controller is positively impacted on the stability of the electromechanical modes.

Further, the SSDC has some impact on the HVDC interaction mode (Mode-5). The damping of Mode-5 decreases as the SSDC gain increases. When the gain is 400, Mode-5 has 8.9% damping. However, this decrement is not significant and therefore, the effect of the SSDC on the HVDC system is negligible. The changes in DC side currents for the pre-described perturbation are compared in Figure 6.15. Figure 6.15(a) shows the DC currents without SSDC and Figure 6.15(b) shows the DC currents with the SSDC at the rectifier current controller. There is no significant difference in the currents with and without SSDC. When the SSDC is inserted, some oscillations resulted due to torsional frequencies can be observed in the latter part of the simulation (Figure 6.15(b)).

SSDC at Inverter DC Voltage Controller

A SSDC can be inserted at the inverter DC voltage controller using the same procedure described in Section 6.2.4. The controllability indices show that Mode-1 , Mode-2 and Mode-3 are controllable at the inverter DC voltage controller input and Mode-4 cannot be controlled at that input. Modes 1, 2 and 3 can be observed in the generator-36 speed and therefore it is used as the input to the SSDC. The frequency response analysis shows around 20^o-40^o phase lead between inverter DC voltage controller input and the generator 36 electrical torque in the frequency range of 0-30Hz. For the simplicity, a phase compensation for this phase lead is not included and only

a gain block is used as the SSDC. A phase compensator and a washout filter would be required for better accuracy.

When the SSDC gain (K_{SSDC}) is 400, Mode-1 shows 1.81% damping and Mode-2 damping is improved to 0.21%. Mode-3 has 0.32% damping. Mode-4 does not show any improvement. Compared to the SSDC at rectifier current controller, the SSDC at inverter DC voltage controller provides more damping for Mode-3. This can be observed in the time domain responses shown in Figure 6.14. As mentioned in the above section, the low damped 30 Hz mode (Mode-3) can be observed in the latter part (close to 4s) of the change in generator 36 speed obtained when the SSDC is at the rectifier current controller (Figure 6.14(b)). When the SSDC is connected at the inverter DC voltage controller, Figure 6.14(c) shows the time domain comparisons of the change in generator 36 speed for the same disturbance. The 30 Hz mode (Mode-3) decays well in this case and cannot be observed in the latter part. Therefore, in this case, the SSDC at inverter DC voltage controller shows better performances compared to the SSDC at the rectifier current controller. The reason is that the inverter is electrically more closer to generator 36 than the rectifier in this test system.

As far as electromechanical oscillations are concerned, this SSDC is also positively impacted the stability of those modes. Major improvements can be observed in Modes 12 and 13. Mode 12 damping is improved to 7.03% and the frequency does not change significantly. Mode 13 is at 0.28Hz with 81.15% damping.

There is negligible impact of the SSDC on the HVDC interaction mode (Mode-5). The damping of Mode-5 is at 9%. When the SSDC connected at the inverter DC voltage controller, the changes in the DC currents for the pre-described disturbance are shown in Figure 6.15(c). This comparison verifies that the impact on the HVDC system is negligible.

6.3.4 Importance of The Hybrid Model

This analysis demonstrate that both low frequency electromechanical oscillations and subsynchronous frequency oscillations can be accurately analyzed using the proposed hybrid small signal stability model. If this model was not available, the subsynchronous interactions have to be analyzed for a small portion of the power system modeled in details either using a small signal model with the entire network dynamics included or using an EMT program. Especially, when designing subsynchronous damping controllers, the above analysis shows that some inter-area electromechanical modes of the power system may be severely affected (eg: Mode-13 in Table 6.4). These inter-area electromechanical modes cannot be analyzed using the small portion of the power system modeled. For this, the entire power system has to be analyzed using a conventional small signal stability program or a transient stability program. If there is some adverse effect on the electromechanical modes, the controller parameters have to be readjusted. Therefore, the detailed model of the small portion of the power system and the conventional small signal model or the transient stability model of the entire power system have to be repeatedly used to obtain the optimal values of the controller parameters. The proposed model would avoid these difficulties and helps to obtain more reliable results.

6.4 Concluding Remarks

A linearized model of a power system with dynamic phasor representation of the transmission network and the stator winding dynamics modeled for the generators is adequate to analyze HVDC-generator-turbine torsional interactions. The HVDC-generator-turbine torsional interactions may occur if there is a slightly damped HVDC controller mode, in which the frequency is close to a torsional mode of the generator-

turbine system. These interactions may even lead to torsional instabilities. This has been demonstrated using electromagnetic transient simulations. A damping controller has been introduced to the HVDC system to damp out the torsional oscillations. The design procedure has been discussed using small signal stability assessment.

In large power systems these subsynchronous oscillations can be analyzed using proposed hybrid small signal stability model. The performance of the hybrid model has been evaluated for the 39-bus test system in designing subsynchronous damping controllers at the HVDC system. The analysis has shown that the damping controller can be introduced either at the rectifier current controller or at the inverter DC voltage controller. Further, the analysis has shown that the controllers may affect the stability of the electromechanical modes as well. The hybrid model has facilitated to accurately analyze both subsynchronous modes and electromechanical modes of the system at the same time.

Chapter 7

Conclusions

7.1 General Conclusions

A small signal stability model suitable for studying HVDC interactions of large power systems has been proposed in this thesis. The modeling requirements for the power systems with HVDC lines have been analyzed. Comparisons of small signal model simulations against EMT type simulations have been used to conclude that the dynamic network representation of the AC network and the stator winding dynamics modeled for the generators are essential to produce meaningful results from a small signal analysis. However, it is not practical to include the dynamics of the entire AC network of a large power system. To overcome this, a hybrid AC network model that allows the parts of the transmission network in the vicinity of HVDC converters or any other dynamic devices to be modeled with their dynamics and the remaining parts to be modeled as constant admittances has been proposed. The hybrid small signal model produces the same results as in the model including the dynamics of the entire AC network. The comparisons with the EMT type simulations have been further confirmed the accuracy of the proposed model. The proposed model and the

model including the dynamics of the entire network have been used in this thesis to accurately analyze multi-in-feed HVDC interactions, HVDC-generator electromechanical interactions and the HVDC-generator-turbine torsional interactions in power systems.

The linearized models of the dynamic devices in power systems and their adequacy in analyzing interactions up to 200Hz have been discussed in Chapter 2. A current injection model of an HVDC system, which can be easily combined with the current injection models of the other dynamic devices, has been proposed in this chapter. The linearized converter models, the HVDC controllers, the phase locked oscillators and the DC transmission system have been included with their dynamics. The dynamic phasor representation has been used to model the AC network and the stator winding dynamics have been included in the synchronous generator model. The models have been validated using time and frequency responses of the EMT simulations.

Chapter 3 describes the proposed hybrid small signal model. Formation of the model has been discussed using examples. The model has been validated using time domain comparisons with the EMT type simulations.

In Chapter 5, multi-in-feed HVDC interactions have been analyzed using the eigenvalues and eigenvectors obtained from the linearized state space model. This analysis has shown that there are several modes where the state variables associated with HVDC converter terminals interact with each other. The rectifier current controllers and the DC line state variables participate the most in these modes. If the HVDC in-feeds are tightly connected in the AC side, they strongly interact with each other. These interactions diminish as the resultant AC impedance between HVDC terminals is increased. In addition to the interactions between the HVDC lines, the electromechanical oscillations of the generators may also be affected by the HVDC systems.

The rectifier current controller parameters affect the stability of the electromechanical modes and some modes become unstable when the controller parameters are adjusted to certain values. Further, the stability of the modes can also be improved using the auxiliary damping/modulation controllers at the rectifier. The design of the controllers has been discussed briefly.

The HVDC-generator-turbine torsional interactions have been analyzed in Chapter 6 using small signal stability assessment. The model including the dynamics of the entire AC network and the proposed hybrid small signal model has been used. The interactions can be accurately identified using the small signal stability assessment. The HVDC-generator-turbine torsional interactions may occur if there is a slightly damped HVDC controller mode, in which the frequency is close to a torsional mode of the generator-turbine system. These interactions may even lead to torsional instabilities. These observations have been verified using EMT type simulations. Further, the possibilities of controlling the torsional modes through HVDC controllers have been investigated. The subsynchronous damping controllers (SSDC) can be included at the rectifier or the inverter controllers to improve the stability of the torsional modes. In addition to these modes, the SSDCs may affect the stability of the widely spread inter-area electromechanical modes as well. The effect of SSDCs on these modes can not be analyzed using a small portion of a power system, which has been modeled in detail. The proposed hybrid model enables the analysis of both of the interactions simultaneously.

This thesis shows the importance of conducting a small signal interaction study for any proposed multi-HVDC system or HVDC-generator-turbine system with torsional oscillations to ascertain whether such interactions exist and if so, whether they pose a threat to the operation of the power system. The modeling procedure including the

hybrid small signal model proposed in this thesis can be used for such studies.

7.2 Contributions

The main contributions of the work presented in this thesis are as follows.

- Evaluated the adequacy of the linearized models of the power systems in analyzing high frequency interactions up to 200Hz. A current injection model of the linearized HVDC system has been developed and it has been combined with the dynamic phasor model of the AC network to analyze the high frequency HVDC interactions on power systems accurately.

- Proposed and validated a hybrid small signal model of power systems, which can be used to analyze low frequency electromechanical oscillations as well as high frequency interactions (up to 200Hz) in large power systems. The dynamic phasor model, which is used to model the areas with high frequency interactions, is combined with the admittance matrix representation of the rest of the power system to obtain the hybrid model.

- Evaluated the capabilities of small signal stability assessment technique in identifying high frequency interactions such as HVDC interactions.

- Proposed a methodology to quantitatively analyze interactions between the HVDC terminals in multi-in-feed HVDC systems, using a small signal stability model. The interactions among the DC lines (DC line resonance modes) and the interactions among the HVDC controllers (HVDC controller modes) can be identified. The stability of these modes can be evaluated under different operating conditions and/or under different controller parameters.

- Proposed to use the small signal stability assessment to analyze HVDC-generator-turbine torsional interactions. The conditions to be satisfied for the torsional interactions between the generator-turbine units and the HVDC systems has been identified using this methodology. Furthermore, the design and the performance of the subsynchronous damping controllers attached to the HVDC systems has been investigated using the same technique.

These contributions have led to the following publications;

- C. Karawita and U.D. Annakkage, "Multi-In-Feed HVDC Interaction Studies Using Small Signal Stability Assessment", *IEEE Transactions on Power Delivery*, Vol.24, No. 2, April 2009.

- C. Karawita and U.D. Annakkage, "A Hybrid Network Model for Small Signal Stability Analysis of Power Systems", submitted to review in *IEEE Transactions on Power Systems.*

- C. Karawita and U.D. Annakkage, "HVDC-Generator Torsional Interaction Studies Using A Linearized Model With Dynamic Network Representation", Accepted to present in I*nternational Conference on Power Systems Transients (IPST)*, June 3-6 2009, Kyoto, Japan.

- C. Karawita, U.D. Annakkage and D. Muthumuni, "Verification of PSCAD simulation results using small signal stability analysis", *Pulse-Manitoba HVDC Research Center Newsletter*, Winter 2007.

- J.R. Lucas, U.D. Annakkage, C. Karawita, R.P. Jayasinghe, D. Muthumuni, "Inclusion of Small Signal Stability Assessment to Electromagnetic Transient Programs", *Fourth IASTED Asian Conference on Power and Energy Systems, Langkawi, Malaysia*, April 2008.

7.3 Suggestions for Future Research

The work presented in this thesis has focused on the analysis of HVDC interactions using small signal stability assessment. In order to analyze these high frequency interactions accurately, suitable small signal models have been developed and they have been validated against EMT type simulations. Ultimately, a hybrid small signal model suitable for large power systems has been proposed. The interactions among the HVDC terminals in multi-in-feed HVDC systems, HVDC-generator electromechanical oscillations and the HVDC-generator-turbine torsional interactions have been analyzed using the developed small signal models.

The proposed small signal model can be used to analyze the interactions of the other dynamic devices in the power systems as well. Further research can be carried out to investigate the interactions of some important devices mentioned below.

- Multi-terminal HVDC links are gaining further popularity in modern power systems. The same methodology used to develop the linearized model of the two-terminal HVDC system can be used and the interactions among the terminals can be analyzed using the small signal stability assessment. Further investigations are required to be performed to identify these interactions.

- The dynamics of the FACTS devices can be added into the small signal models developed in this thesis. Especially, voltage source converter (VSC) type HVDC links have been proposed to be widely used in modern power systems. Apart from that, SVCs, STATCOMs and UPFCs are used in power systems. Fast controllers are used in these devices and these controllers may produce high frequency interactions. The methodology described in this thesis can be used to analyze these interactions as well. Although the linearized models of these

devices are readily available, further investigations are required to identify the interactions between different dynamic devices in power system. The proposed hybrid small signal model can be used for this.

- Nowadays, wind turbines are used to generate electric power all over the world. Various technologies are used to generate the power. Doubly-fed induction generators, permanent magnet generators and induction generators with back to back converters are some of the generating mechanisms. These devices with their controllers may produce high frequency interactions, which can not be analyzed using the conventional small signal models. The linearized models of these devices can be added into the small signal models described in this thesis and further studies are required to investigate these interactions.

The hybrid small signal model proposed in this thesis can be easily incorporated with the commercial software packages designed for the conventional small signal stability assessment. This would be useful to analyze the interactions described in this thesis and the other interaction studies suggested in this section.

Appendix A

Test Systems Data

A.1 CIGRE Benchmark HVDC Test System

Converter Data

$B_r = 2$	$B_i = 2$	$X_{cr} = 0.18pu$	$X_{ci} = 0.18pu$
$V_{ac,r} = 345kV\angle 0^o$	$V_{ac,i} = 230kV\angle 0^o$	$T_r = 1.6163$	$T_i = 1.0993$
$I_{dc,order} = 2kA$	$\gamma_{order} = 15^o$	$\alpha_r = 15^o$	$\alpha_i = 141.8^o$

DC Line Data

$R_{dc} = 5\Omega$	$L_{dc} = 1.1963H$	$C = 26\mu F$

HVDC Controller Data

$K_{Pr} = 1.0989$	$K_{Ir} = 91.575$	$K_{Pi} = 0.7506$	$K_{Ii} = 18.3824$

Phase Lock Oscillators

$K_{PPr} = 10$	$K_{IPr} = 50$	$K_{PPi} = 10$	$K_{IPi} = 50$

All the AC filters and the line impedances are kept as in [27].

A.2 Multi-in-feed HVDC Test System

The test system is shown in Figure 2.14 of Chapter 2.

A.2.1 AC voltage Sources

Sources were kept at the following values.

Source	Voltage (kV)	Angle (Deg.)
S1 & S3	314.14	11.4
S4	211.60	0.0

A.2.2 HVDC systems

HVDC1 and HVDC2 were at 500MW, 500kV(DC). For both of the HVDC systems,

$B_r = 2$	$B_i = 2$	$T_r = 1.6163$
$X_{cr} = 0.18pu$	$X_{ci} = 0.18pu$	$R_{dc} = 5\Omega$
$L_{dc} = 1.1963H$	$C = 26\mu F$	$I_{dc,ord} = 1kA$
$\gamma_{ord} = 15^o$	$K_{Pr} = 1.0989$	$K_{Ir} = 91.575$
$K_{Pi} = 0.7506$	$K_{Ii} = 18.3824$	$V_{AC,r} = 345kV\angle 0^o$

Following quantities were individually selected for the HVDC systems.

$T_{i1} = 1.2094$	$T_{i2} = 1.1539$
$V_{ac,i1} = 253.05kV\angle 36.18^o$	$V_{ac,i2} = 241.43kV\angle 22.99^o$

The PLO parameters are as in Section A.1.

All the AC filters in the system was kept as in [27]. The inductances and the resistances in the source impedances were decreased from the original values by factor of 1.3.

The tie line has a resistance of 2.4285Ω and an inductance of $51.347mH$.

A.2.3 Generator at S2

500MVA, 22kV generator with a 230kV/22kV transformer were included at S2 . The transformer reactance was included in the source impedance. The generator parameters are given below.

$V_t = 1.05$	$\delta_t = 43.12^o$	$P_t = 0.8$	$Q_t = -0.51$
$L_d = 1.4$	$L'_d = 0.3$	$L''_d = 0.2$	$R_a = 0$
$L_q = 1.35$	$L'_q = 0.6$	$L''_q = 0.2$	$L_l = 0.1$
$T'_{do} = 6$	$T'_{qo} = 1$	$T''_{do} = 0.05$	$T''_{qo} = 0.05$
$H = 3$	$K_d = 0$		

AC4A exciter parameters are as follows.

$K_A = 30$	$T_A = 0.05$	$T_B = 10$	$T_C = 1$	$T_r = 0.002$

The governor and turbine parameters are given below.

$R_p = 0.04$	$T_p = 0.05$	$Q = 5$	$T_g = 0.2$	$R_t = 0.8$
$T_R = 2$	$q_{NL} = 0.05$	$T_w = 2$	$f_p = 0.02$	$D = 0.5$

A.3 New England 39 Bus System

A.3.1 Power Flow - AC Bus Data

Bus				Voltage	
Number	Name	Base kV	Type	Magnitude	Angle
1	LOAD 1 345.	345	Load Bus	1.0474	1.6114
2	LOAD 2 345.	345	Load Bus	1.0487	4.2917
3	LOAD 3 345.	345	Load Bus	1.0302	1.4456
4	LOAD 4 345.	345	Load Bus	1.0039	0.4357
5	LOAD 5 345.	345	Load Bus	1.0053	1.4296
6	LOAD 6 345.	345	Load Bus	1.0077	2.0913
7	LOAD 7 345.	345	Load Bus	0.9970	-0.0819
8	LOAD 8 345.	345	Load Bus	0.9960	-0.5730
9	LOAD 9 345.	345	Load Bus	1.0282	-0.2732
10	LOAD 10 345.	345	Load Bus	1.0172	4.6144
11	LOAD 11 345.	345	Load Bus	1.0127	3.7571
12	LOAD 12 345.	345	Load Bus	1.0002	3.7979
13	LOAD 13 345.	345	Load Bus	1.0143	3.9440
14	LOAD 14 345.	345	Load Bus	1.0117	2.3858
15	LOAD 15 345.	345	Load Bus	1.0154	2.3070
16	LOAD 16 345.	345	Load Bus	1.0318	3.8559
17	LOAD 17 345.	345	Load Bus	1.0336	2.7425
18	LOAD 18 345.	345	Load Bus	1.0309	1.8201
19	LOAD 19 345.	345	Load Bus	1.0499	9.0207
20	LOAD 20 110.	110	Load Bus	0.9912	8.0288
21	LOAD 21 345.	345	Load Bus	1.0318	6.2629
22	LOAD 22 345.	345	Load Bus	1.0498	10.7117
23	LOAD 23 345.	345	Load Bus	1.0448	10.5134
24	LOAD 24 345.	345	Load Bus	1.0373	3.9755
25	LOAD 25 345.	345	Load Bus	1.0576	5.6819
26	LOAD 26 345.	345	Load Bus	1.0521	4.5178
27	LOAD 27 345.	345	Load Bus	1.0377	2.5488
28	LOAD 28 345.	345	Load Bus	1.0501	8.0296
29	LOAD 29 345.	345	Load Bus	1.0499	10.7889
30	GEN 30 13.8	13.8	Gen. Bus	1.0475	6.7115
31	GEN 31 13.8	13.8	Gen. Bus	0.9820	10.0327
32	GEN 32 13.8	13.8	Gen. Bus	0.9831	12.6104
33	GEN 33 13.8	13.8	Gen. Bus	0.9972	14.2381
34	GEN 34 13.8	13.8	Gen. Bus	1.0123	13.2184
35	GEN 35 13.8	13.8	Gen. Bus	1.0493	15.6735
36	GEN 36 13.8	13.8	Gen. Bus	1.0635	18.3663
37	GEN 37 13.8	13.8	Gen. Bus	1.0278	12.4663
38	GEN 38 13.8	13.8	Gen. Bus	1.0265	17.8522
39	GEN 39 13.8	345	Swing Bus	1.0300	0.0000

A.3.2 Power Flow - Load Data

Bus Number	MW	MVAr
3	322.00	2.40
4	500.00	184.00
7	233.80	84.00
8	522.00	176.00
12	7.50	88.00
15	320.00	153.00
16	329.00	32.30
18	158.00	30.00
20	628.00	103.00
21	274.00	115.00
23	247.50	84.60
24	308.60	-92.20
25	224.00	47.20
26	139.00	17.00
27	281.00	75.50
28	206.00	27.60
29	283.50	26.90
31	9.20	4.60
39	1104.00	250.00

A.3.3 Power Flow - Generator Data

Bus Number	MW	MVAr
30	250.00	146.14
31	520.28	198.13
32	650.00	205.10
33	632.00	109.89
34	508.00	165.76
35	650.00	212.39
36	560.00	101.16
37	540.00	0.43
38	830.00	22.84
39	1000.52	88.21

A.3.4 Power Flow - Line Data

From Bus Number	To Bus Number	Series		Charging	
		Resistance	Reactance	Conductance	Susceptance
1	2	0.00350	0.04110	0.00000	0.69870
1	39	0.00100	0.02500	0.00000	0.75000
2	3	0.00130	0.01510	0.00000	0.25720
2	25	0.00700	0.00860	0.00000	0.14600
3	4	0.00130	0.02130	0.00000	0.22140
3	18	0.00110	0.01330	0.00000	0.21380
4	5	0.00080	0.01280	0.00000	0.13420
4	14	0.00080	0.01290	0.00000	0.13820
5	6	0.00020	0.00260	0.00000	0.04340
5	8	0.00080	0.01120	0.00000	0.14760
6	7	0.00060	0.00920	0.00000	0.11300
6	11	0.00070	0.00820	0.00000	0.13890
7	8	0.00040	0.00460	0.00000	0.07800
8	9	0.00230	0.03630	0.00000	0.38040
9	39	0.00100	0.02500	0.00000	1.20000
10	11	0.00040	0.00430	0.00000	0.07290
10	13	0.00040	0.00430	0.00000	0.07290
13	14	0.00090	0.01010	0.00000	0.17230
14	15	0.00180	0.02170	0.00000	0.36600
15	16	0.00090	0.00940	0.00000	0.17100
16	17	0.00070	0.00890	0.00000	0.13420
16	19	0.00160	0.01950	0.00000	0.30400
16	21	0.00080	0.01350	0.00000	0.25480
16	24	0.00030	0.00590	0.00000	0.06800
17	18	0.00070	0.00820	0.00000	0.13190
17	27	0.00130	0.01730	0.00000	0.32160
21	22	0.00080	0.01400	0.00000	0.25650
22	23	0.00060	0.00960	0.00000	0.18460
23	24	0.00220	0.03500	0.00000	0.36100
25	26	0.00320	0.03230	0.00000	0.51300
26	27	0.00140	0.01470	0.00000	0.23960
26	28	0.00430	0.04740	0.00000	0.78020
26	29	0.00570	0.06250	0.00000	1.02900
28	29	0.00140	0.01510	0.00000	0.24900

Per unit values are based on 100MVA rating.

A.3.5 Power Flow - Transformer Data

From Bus Number	To Bus Number	Ratio		Series	
		From	To	Resistance	Reactance
2	30	1.02500	1.00000	0.00000	0.01810
6	31	1.07000	1.00000	0.00000	0.02500
10	32	1.07000	1.00000	0.00000	0.02000
12	11	1.00600	1.00000	0.00160	0.04350
12	13	1.00600	1.00000	0.00160	0.04350
19	20	1.06000	1.00000	0.00070	0.01380
19	33	1.07000	1.00000	0.00070	0.01420
20	34	1.00900	1.00000	0.00090	0.01800
25	37	1.02500	1.00000	0.00060	0.02320
29	38	1.02500	1.00000	0.00080	0.01560

A.3.6 Dynamic Data - Generators

IBUS	T'do	T"do	T'qo	T"qo	H	D	Xd	Xq	X'd	X'q	X"d	Xl	MVA	Rsource
30	10.20	0.02	1.50	0.02	4.20	0	1.00	0.69	0.31	0.30	0.20	0.13	1000	0.0010
31	6.56	0.02	1.50	0.02	3.03	0	2.95	2.82	0.70	1.67	0.53	0.35	1000	0.0010
32	5.70	0.02	1.50	0.02	3.58	0	2.50	2.37	0.53	0.88	0.40	0.30	1000	0.0010
33	5.69	0.02	1.50	0.02	2.86	0	2.62	2.58	0.80	1.43	0.60	0.30	1000	0.0010
34	5.40	0.02	0.44	0.02	2.60	0	6.70	6.20	1.32	1.66	0.99	0.54	1000	0.0010
35	7.30	0.02	0.40	0.02	3.48	0	2.54	2.41	0.50	0.81	0.38	0.22	1000	0.0010
36	5.66	0.02	1.50	0.02	2.64	0	2.95	2.92	0.90	1.67	0.68	0.32	1000	0.0010
37	6.70	0.02	0.41	0.02	2.43	0	2.90	2.80	0.57	0.91	0.43	0.28	1000	0.0010
38	4.79	0.02	1.96	0.02	3.45	0	2.11	2.05	0.57	0.70	0.43	0.30	1000	0.0010
39	5.70	0.02	1.50	0.02	6.13	0	1.46	1.38	0.31	0.51	0.23	0.18	1000	0.0006

A.3.7 Dynamic Data - Exciters (AC4A)

Bus Number	TA	TB	TC	KA	Tr
30	0.05	10	1	6.2	0.002
31	0.06	10	1	5	0.002
32	0.06	10	1	5	0.002
33	0.02	10	1	40	0.002
34	0.02	10	1	5	0.002
35	0.02	10	1	40	0.002
36	0.02	10	1	5	0.002
37	0.02	10	1	40	0.002
39	0.06	10	1	5	0.002

A.3.8 Dynamic Data - Turbines & Governors (HyTur1 and HyGov1)

The Same turbine and governor data were used for all generators. The data are as follows.

$R_p = 0.04$	$T_p = 0.05$	$Q = 5$	$T_g = 0.2$	$R_t = 0.8$
$T_R = 2$	$q_{NL} = 0.05$	$T_w = 2$	$f_p = 0.02$	$D = 0.5$

Appendix B

AC Network Models

B.1 Linearized AC network models-An Example

The formation of the admittance matrix representation and the dynamic phasor model of the AC network is explained using the network shown in Figure B.1.

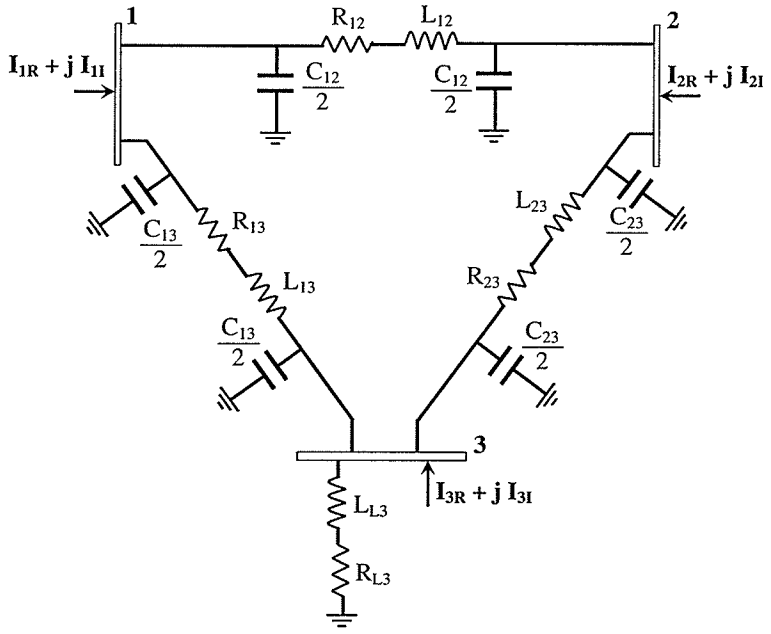

Figure B.1: AC Network Example

B.1.1 Admittance Matrix Representation

The admittances at the fundamental frequency are considered. The π model is used for the transmission lines. The relationship between the changes in current injections at the nodes and the node voltages is given by,

$$\begin{bmatrix} \Delta I_{1R} \\ \Delta I_{1I} \\ \Delta I_{2R} \\ \Delta I_{2I} \\ \Delta I_{3R} \\ \Delta I_{3I} \end{bmatrix} = \begin{bmatrix} g_{11} & -b_{11} & -g_{12} & b_{12} & -g_{13} & b_{13} \\ b_{11} & g_{11} & -b_{12} & -g_{12} & -b_{13} & -g_{13} \\ -g_{12} & b_{12} & g_{22} & -b_{22} & -g_{23} & b_{23} \\ -b_{12} & -g_{12} & b_{22} & g_{22} & -b_{23} & -g_{23} \\ -g_{13} & b_{13} & -g_{23} & b_{23} & g_{33} & -b_{33} \\ -b_{13} & -g_{13} & -b_{23} & -g_{23} & b_{33} & g_{33} \end{bmatrix} \begin{bmatrix} \Delta V_{1R} \\ \Delta V_{1I} \\ \Delta V_{2R} \\ \Delta V_{2I} \\ \Delta V_{3R} \\ \Delta V_{3I} \end{bmatrix} \tag{B.1}$$

In the above equation,

$$g_{11} = g_{12} + g_{13}$$
$$b_{11} = b_{12} + b_{13} + \frac{\omega_0 C_{12}}{2} + \frac{\omega_0 C_{13}}{2}$$
$$g_{22} = g_{12} + g_{23}$$
$$b_{22} = b_{12} + b_{23} + \frac{\omega_0 C_{12}}{2} + \frac{\omega_0 C_{23}}{2}$$
$$g_{33} = g_{13} + g_{23} + g_{L3}$$
$$b_{33} = b_{13} + b_{23} + b_{L3} + \frac{\omega_0 C_{13}}{2} + \frac{\omega_0 C_{23}}{2}$$

where, the conductance and the susceptance between node-m and node-n are given by, $g_{mn} = \Re\{\frac{1}{R_{mn}+j\omega_0 L_{mn}}\}$ and $b_{mn} = \Im\{\frac{1}{R_{mn}+j\omega_0 L_{mn}}\}$ respectively. g_{L3} and b_{L3} are the conductance and the susceptance of the load at bus 3.

B.1.2 Dynamic Phasor Representation

The series R-L components in the circuit shown in Figure B.1 are modeled using equation (2.36) given in Chapter 2. There are four series R-L components (three transmission lines and one load) and therefore 8 state variables are in the system. The state space model is given in equation (B.2).

$$\begin{bmatrix} \Delta\dot{I}_{12R} \\ \Delta\dot{I}_{12I} \\ \Delta\dot{I}_{13R} \\ \Delta\dot{I}_{13I} \\ \Delta\dot{I}_{23R} \\ \Delta\dot{I}_{23I} \\ \Delta\dot{I}_{L3R} \\ \Delta\dot{I}_{L3I} \end{bmatrix} = \begin{bmatrix} \\ A_{net1} \\ \\ \end{bmatrix} \begin{bmatrix} \Delta I_{12R} \\ \Delta I_{12I} \\ \Delta I_{13R} \\ \Delta I_{13I} \\ \Delta I_{23R} \\ \Delta I_{23I} \\ \Delta I_{L3R} \\ \Delta I_{L3I} \end{bmatrix} + \begin{bmatrix} \\ E_{net1} \\ \\ \end{bmatrix} \begin{bmatrix} \Delta V_{1R} \\ \Delta V_{1I} \\ \Delta V_{2R} \\ \Delta V_{2I} \\ \Delta V_{3R} \\ \Delta V_{3I} \end{bmatrix} \tag{B.2}$$

In the above equation,

$$A_{net1} = \begin{bmatrix} \frac{-R_{12}\omega_0}{L_{12}} & \omega_0 & 0 & 0 & 0 & 0 & 0 & 0 \\ -\omega_0 & \frac{-R_{12}\omega_0}{L_{12}} & 0 & 0 & 0 & 0 & 0 & 0 \\ 0 & 0 & \frac{-R_{13}\omega_0}{L_{13}} & \omega_0 & 0 & 0 & 0 & 0 \\ 0 & 0 & -\omega_0 & \frac{-R_{13}\omega_0}{L_{13}} & 0 & 0 & 0 & 0 \\ 0 & 0 & 0 & 0 & \frac{-R_{23}\omega_0}{L_{23}} & \omega_0 & 0 & 0 \\ 0 & 0 & 0 & 0 & -\omega_0 & \frac{-R_{23}\omega_0}{L_{23}} & 0 & 0 \\ 0 & 0 & 0 & 0 & 0 & 0 & \frac{-R_{L3}\omega_0}{L_{L3}} & \omega_0 \\ 0 & 0 & 0 & 0 & 0 & 0 & -\omega_0 & \frac{-R_{23}\omega_0}{L_{23}} \end{bmatrix}$$

and

$$E_{net1} = \begin{bmatrix} \frac{\omega_0}{L_{12}} & 0 & \frac{-\omega_0}{L_{12}} & 0 & 0 & 0 \\ 0 & \frac{\omega_0}{L_{12}} & 0 & \frac{-\omega_0}{L_{12}} & 0 & 0 \\ \frac{\omega_0}{L_{13}} & 0 & 0 & 0 & \frac{-\omega_0}{L_{13}} & 0 \\ 0 & \frac{\omega_0}{L_{13}} & 0 & 0 & 0 & \frac{-\omega_0}{L_{13}} \\ 0 & 0 & \frac{\omega_0}{L_{23}} & 0 & \frac{-\omega_0}{L_{23}} & 0 \\ 0 & 0 & 0 & \frac{\omega_0}{L_{23}} & 0 & \frac{-\omega_0}{L_{23}} \\ 0 & 0 & 0 & 0 & \frac{\omega_0}{L_{23}} & 0 \\ 0 & 0 & 0 & 0 & 0 & \frac{\omega_0}{L_{L3}} \end{bmatrix}$$

All the capacitances of the transmission lines are added together at the bus bars to find the total capacitances at the bus bars. For example, Bus1 total capacitance is the capacitances of the lines 1-2 and 1-3 ($\frac{C_{12}}{2} + \frac{C_{13}}{2}$) connected to it. All the bus voltages are modeled as state variables. The linearized models of the bus capacitances are obtained using equation (2.39). The state space model of the bus voltages are given by equation (B.3).

$$\begin{bmatrix} \Delta\dot{V}_{1R} \\ \Delta\dot{V}_{1I} \\ \Delta\dot{V}_{2R} \\ \Delta\dot{V}_{2I} \\ \Delta\dot{V}_{3R} \\ \Delta\dot{V}_{3I} \end{bmatrix} = \begin{bmatrix} \quad \\ A_{net2} \\ \quad \end{bmatrix} \begin{bmatrix} \Delta V_{1R} \\ \Delta V_{1I} \\ \Delta V_{2R} \\ \Delta V_{2I} \\ \Delta V_{3R} \\ \Delta V_{3I} \end{bmatrix} + \begin{bmatrix} \quad \\ C_{net2} \\ \quad \end{bmatrix} \begin{bmatrix} \Delta I_{12R} \\ \Delta I_{12I} \\ \Delta I_{13R} \\ \Delta I_{13I} \\ \Delta I_{23R} \\ \Delta I_{23I} \\ \Delta I_{L3R} \\ \Delta I_{L3I} \end{bmatrix} + \begin{bmatrix} \quad \\ D_{net2} \\ \quad \end{bmatrix} \begin{bmatrix} \Delta I_{1R} \\ \Delta I_{1I} \\ \Delta I_{2R} \\ \Delta I_{2I} \\ \Delta I_{3R} \\ \Delta I_{3I} \end{bmatrix} \quad \text{(B.3)}$$

In the above equation,

$$A_{net2} = \begin{bmatrix} 0 & \omega_0 & 0 & 0 & 0 & 0 \\ -\omega_0 & 0 & 0 & 0 & 0 & 0 \\ 0 & 0 & 0 & \omega_0 & 0 & 0 \\ 0 & 0 & -\omega_0 & 0 & 0 & 0 \\ 0 & 0 & 0 & 0 & 0 & \omega_0 \\ 0 & 0 & 0 & 0 & -\omega_0 & 0 \end{bmatrix}, \; C_{net2} = \begin{bmatrix} \frac{-\omega_0}{C_1} & 0 & \frac{-\omega_0}{C_1} & 0 & 0 & 0 & 0 & 0 \\ 0 & \frac{-\omega_0}{C_1} & 0 & \frac{-\omega_0}{C_1} & 0 & 0 & 0 & 0 \\ \frac{\omega_0}{C_2} & 0 & 0 & 0 & \frac{-\omega_0}{C_2} & 0 & 0 & 0 \\ 0 & \frac{\omega_0}{C_2} & 0 & 0 & 0 & \frac{-\omega_0}{C_2} & 0 & 0 \\ 0 & 0 & \frac{\omega_0}{C_3} & 0 & \frac{\omega_0}{C_3} & 0 & \frac{-\omega_0}{C_3} & 0 \\ 0 & 0 & 0 & \frac{\omega_0}{C_3} & 0 & \frac{\omega_0}{C_3} & 0 & \frac{-\omega_0}{C_3} \end{bmatrix}$$

and

$$D_{net2} = \begin{bmatrix} \frac{\omega_0}{C_1} & 0 & 0 & 0 & 0 & 0 \\ 0 & \frac{\omega_0}{C_1} & 0 & 0 & 0 & 0 \\ 0 & 0 & \frac{\omega_0}{C_2} & 0 & 0 & 0 \\ 0 & 0 & 0 & \frac{\omega_0}{C_2} & 0 & 0 \\ 0 & 0 & 0 & 0 & \frac{\omega_0}{C_3} & 0 \\ 0 & 0 & 0 & 0 & 0 & \frac{\omega_0}{C_3} \end{bmatrix}$$

where, $C_1 = \frac{C_{12}+C_{13}}{2}$, $C_2 = \frac{C_{12}+C_{23}}{2}$ and $C_3 = \frac{C_{13}+C_{23}}{2}$. All the R-L-C values are in pu.

The overall state space model of the AC network given in equation (B.4) is obtained by combining equations (B.2) and (B.3) together.

$$[\Delta \dot{X}_{ACnet}] = [A_{ACnet}]\ [\Delta X_{ACnet}] + [D_{ACnet}]\ [\Delta I_{inj}] \tag{B.4}$$

$[\Delta I_{inj}]$ is the change in current injections of the dynamic devices at the bus bars. This state space model of the network can be easily combined with the current injection models of the dynamic devices to eliminate $[\Delta I_{inj}]$ terms.

Appendix C

Generator, Exciter And Governor-Turbine Models

C.1 Linearized Generator Models

The conventional round rotor (6^{th} order) and salient pole (5^{th} order) models are used when the admittance matrix is used to represent the AC network. Two additional differential equations for the stator flux components in d-q axes are added to the synchronous machine model, when the AC network is represented using a dynamic phasor model. Therefore, an 8^{th} order model is used for round rotor type and a 7^{th} order model is used for salient pole type. These linearized models are summarized in the following sections.

C.1.1 Conventional Generator Model

The round rotor type (6^{th} order) generator model is formulated in the following text. The model can be easily simplified to the salient pole model by removing the second damper winding in the q-axis. The d-q axes are selected according to the convention

given in [15]. The standard notations given in [15] are used. The steady state relationships and other details can be found in [15]. Only the linearized model is given below.

The changes in the d-q axes currents are given by equations (C.1) and (C.2) respectively. The currents are expressed in terms of the six state variables and the terminal voltage (R-I components with respect to the common reference).

$$\Delta i_d = K_{id1}\Delta\delta + K_{id2}\Delta\omega_r + K_{id3}\Delta\Phi_{fd} + K_{id4}\Delta\Phi_{1d} + K_{id5}\Delta\Phi_{1q} + K_{id6}\Delta\Phi_{2q} + K_{id7}\Delta V_R + K_{id8}\Delta V_I \quad \text{(C.1)}$$

In the above equation,

$$K_{id1} = \frac{L''_q e_d - R_a e_q}{L''_d L''_q + R_a^2} \qquad K_{id2} = 0$$

$$K_{id3} = \frac{L''_{ad} L''_q}{L_{fd}(L''_d L''_q + R_a^2)} \qquad K_{id4} = \frac{L''_{ad} L''_q}{L_{1d}(L''_d L''_q + R_a^2)}$$

$$K_{id5} = -\frac{L''_{aq} R''_a}{L_{1q}(L''_d L''_q + R_a^2)} \qquad K_{id6} = -\frac{L''_{aq} R''_a}{L_{2q}(L''_d L''_q + R_a^2)}$$

$$K_{id7} = -\frac{L''_q \cos(\delta) + R_a \sin(\delta)}{L''_d L''_q + R_a^2} \qquad K_{id8} = -\frac{L''_q \sin(\delta) - R_a \cos(\delta)}{L''_d L''_q + R_a^2}$$

$$\Delta i_q = K_{iq1}\Delta\delta + K_{iq2}\Delta\omega_r + K_{iq3}\Delta\Phi_{fd} + K_{iq4}\Delta\Phi_{1d} + K_{iq5}\Delta\Phi_{1q} + K_{iq6}\Delta\Phi_{2q} + K_{iq7}\Delta V_R + K_{iq8}\Delta V_I \quad \text{(C.2)}$$

In the above equation,

$$K_{iq1} = \frac{R_a e_d + L''_d e_q}{L''_d L''_q + R_a^2} \qquad K_{iq2} = 0$$

$$K_{iq3} = \frac{L''_{ad} R''_a}{L_{fd}(L''_d L''_q + R_a^2)} \qquad K_{iq4} = \frac{L''_{ad} R''_a}{L_{1d}(L''_d L''_q + R_a^2)}$$

$$K_{iq5} = \frac{L''_{aq} L''_d}{L_{1q}(L''_d L''_q + R_a^2)} \qquad K_{iq6} = \frac{L''_{aq} L''_d}{L_{2q}(L''_d L''_q + R_a^2)}$$

$$K_{iq7} = \frac{L''_d \sin(\delta) - R_a \cos(\delta)}{L''_d L''_q + R_a^2} \qquad K_{iq8} = -\frac{L''_d \cos(\delta) + R_a \sin(\delta)}{L''_d L''_q + R_a^2}$$

The generator state space model is given by equation (C.3). The model is given in the form of ($\Delta \dot{X}_g = A_g\, \Delta X_g + B_g\, \Delta U_g + E_g\, \Delta V_g$). There are six state variables: rotor angle(δ), rotor speed (ω_0), d-axis field winding flux (Φ_{fd}), d-axis damper winding flux (Φ_{1d}), q-axis first damper winding flux (Φ_{1q}) and q-axis second damper winding flux (Φ_{2q}) and two inputs: mechanical torque (T_m) and voltage applied to the field winding (E_{fd}) in the system.

$$\begin{bmatrix} \Delta\dot{\delta} \\ \Delta\dot{\omega}_r \\ \Delta\dot{\Phi}_{fd} \\ \Delta\dot{\Phi}_{1d} \\ \Delta\dot{\Phi}_{1q} \\ \Delta\dot{\Phi}_{2q} \end{bmatrix} = \begin{bmatrix} 0 & ag_{12} & 0 & 0 & 0 & 0 \\ ag_{21} & ag_{22} & ag_{23} & ag_{24} & ag_{25} & ag_{26} \\ ag_{31} & 0 & ag_{33} & ag_{34} & ag_{35} & ag_{36} \\ ag_{41} & 0 & ag_{43} & ag_{44} & ag_{45} & ag_{46} \\ ag_{51} & 0 & ag_{53} & ag_{54} & ag_{55} & ag_{56} \\ ag_{61} & 0 & ag_{63} & ag_{64} & ag_{65} & ag_{66} \end{bmatrix} \begin{bmatrix} \Delta\delta \\ \Delta\omega_r \\ \Delta\Phi_{fd} \\ \Delta\Phi_{1d} \\ \Delta\Phi_{1q} \\ \Delta\Phi_{2q} \end{bmatrix}$$
$$+ \begin{bmatrix} 0 & 0 \\ bg_{21} & 0 \\ 0 & bg_{32} \\ 0 & 0 \\ 0 & 0 \\ 0 & 0 \end{bmatrix} \begin{bmatrix} \Delta T_m \\ \Delta E_{fd} \end{bmatrix} + \begin{bmatrix} 0 & 0 \\ eg_{21} & eg_{22} \\ eg_{31} & eg_{32} \\ eg_{41} & eg_{42} \\ eg_{51} & eg_{52} \\ eg_{61} & eg_{62} \end{bmatrix} \begin{bmatrix} \Delta V_R \\ \Delta V_I \end{bmatrix} \qquad \text{(C.3)}$$

In the above equation,

The parameters of the A_g matrix are given by,

$$ag_{12} = \omega_0$$

$$ag_{21} = -\frac{1}{M}[i_d e_q - i_q e_d + (e_d + 2R_a i_d)K_{id1} + (e_q + 2R_a i_q)K_{iq1}]$$

$$ag_{22} = -\frac{K_d}{M}$$

$$ag_{23} = -\frac{1}{M}[(e_d + 2R_a i_d)K_{id3} + (e_q + 2R_a i_q)K_{iq3}]$$

$$ag_{24} = -\frac{1}{M}[(e_d + 2R_a i_d)K_{id4} + (e_q + 2R_a i_q)K_{iq4}]$$

$$ag_{25} = -\frac{1}{M}[(e_d + 2R_a i_d)K_{id5} + (e_q + 2R_a i_q)K_{iq5}]$$

$$ag_{26} = -\frac{1}{M}[(e_d + 2R_a i_d)K_{id6} + (e_q + 2R_a i_q)K_{iq6}]$$

$$ag_{31} = -\frac{\omega_0 R_{fd} L''_{ad}}{L_{fd}} K_{id1}$$

$$ag_{33} = -\frac{\omega_0 R_{fd} L''_{ad}}{L_{fd}}[\frac{1}{L_{ad}} + \frac{1}{L_{1d}} + K_{id3}]$$

$$ag_{34} = -\frac{\omega_0 R_{fd} L''_{ad}}{L_{fd}}[-\frac{1}{L_{1d}} + K_{id4}]$$

$$ag_{35} = -\frac{\omega_0 R_{fd} L''_{ad}}{L_{fd}} K_{id5}$$

$$ag_{36} = -\frac{\omega_0 R_{fd} L''_{ad}}{L_{fd}} K_{id6}$$

$$ag_{41} = -\frac{\omega_0 R_{1d} L''_{ad}}{L_{1d}} K_{id1}$$

$$ag_{43} = -\frac{\omega_0 R_{1d} L''_{ad}}{L_{1d}}[-\frac{1}{L_{fd}} + K_{id3}]$$

$$ag_{44} = -\frac{\omega_0 R_{1d} L''_{ad}}{L_{1d}}[\frac{1}{L_{ad}} + \frac{1}{L_{fd}} + K_{id4}]$$

$$ag_{45} = -\frac{\omega_0 R_{1d} L''_{ad}}{L_{1d}} K_{id5}$$

$$ag_{46} = -\frac{\omega_0 R_{1d} L''_{ad}}{L_{1d}} K_{id6}$$

$$ag_{51} = -\frac{\omega_0 R_{1q} L''_{aq}}{L_{1q}} K_{iq1}$$

$$ag_{53} = -\frac{\omega_0 R_{1q} L''_{aq}}{L_{1q}} K_{iq3}$$

$$ag_{54} = -\frac{\omega_0 R_{1q} L''_{aq}}{L_{1q}} K_{iq4}$$

$$ag_{55} = -\frac{\omega_0 R_{1q} L''_{aq}}{L_{1q}}[\frac{1}{L_{aq}} + \frac{1}{L_{2q}} + K_{iq5}]$$

$$ag_{56} = -\frac{\omega_0 R_{1q} L''_{aq}}{L_{1q}}[-\frac{1}{L_{2q}} + K_{iq6}]$$

$$ag_{61} = -\frac{\omega_0 R_{2q} L''_{aq}}{L_{2q}} K_{iq1}$$

$$ag_{63} = -\frac{\omega_0 R_{2q} L''_{aq}}{L_{2q}} K_{iq3}$$

$$ag_{64} = -\frac{\omega_0 R_{2q} L''_{aq}}{L_{2q}} K_{iq4}$$
$$ag_{65} = -\frac{\omega_0 R_{2q} L''_{aq}}{L_{2q}} [-\frac{1}{L_{1q}} + K_{iq5}]$$
$$ag_{66} = -\frac{\omega_0 R_{2q} L''_{aq}}{L_{2q}} [\frac{1}{L_{aq}} + \frac{1}{L_{1q}} + K_{iq6}]$$

The parameters of the B_g matrix are given by,

$$bg_{21} = \frac{1}{M}$$
$$bg_{32} = \frac{\omega_0 R_{fd}}{L_{ad}}$$

The parameters of the E_g matrix are given by,

$$eg_{21} = -\frac{1}{M}[I_R + (e_d + 2R_a i_d)K_{id7} + (e_q + 2R_a i_q)K_{iq7}]$$
$$eg_{22} = -\frac{1}{M}[I_I + (e_d + 2R_a i_d)K_{id8} + (e_q + 2R_a i_q)K_{iq8}]$$
$$eg_{31} = -\frac{\omega_0 R_{fd} L''_{ad}}{L_{fd}} K_{id7}$$
$$eg_{32} = -\frac{\omega_0 R_{fd} L''_{ad}}{L_{fd}} K_{id8}$$
$$eg_{41} = -\frac{\omega_0 R_{1d} L''_{ad}}{L_{1d}} K_{id7}$$
$$eg_{42} = -\frac{\omega_0 R_{1d} L''_{ad}}{L_{1d}} K_{id8}$$
$$eg_{51} = -\frac{\omega_0 R_{1q} L''_{aq}}{L_{1q}} K_{iq7}$$
$$eg_{52} = -\frac{\omega_0 R_{1q} L''_{aq}}{L_{1q}} K_{iq8}$$
$$eg_{61} = -\frac{\omega_0 R_{2q} L''_{aq}}{L_{2q}} K_{iq7}$$
$$eg_{62} = -\frac{\omega_0 R_{2q} L''_{aq}}{L_{2q}} K_{iq8}$$

The R-I components of the output current of the generator can be expressed in terms of the state variables and the voltage as given in equation (C.4). The current equation is given in the form of ($\Delta I_g = C_g\ \Delta X_g - Y_g\ \Delta V_g$).

$$\begin{bmatrix} \Delta I_R \\ \Delta I_I \end{bmatrix} = \begin{bmatrix} cg_{11} & 0 & cg_{13} & cg_{14} & cg_{15} & cg_{16} \\ cg_{21} & 0 & cg_{23} & cg_{24} & cg_{25} & cg_{26} \end{bmatrix} \begin{bmatrix} \Delta\delta \\ \Delta\omega_r \\ \Delta\Phi_{fd} \\ \Delta\Phi_{1d} \\ \Delta\Phi_{1q} \\ \Delta\Phi_{2q} \end{bmatrix} - \begin{bmatrix} yg_{11} & yg_{12} \\ yg_{21} & yg_{22} \end{bmatrix} \begin{bmatrix} \Delta V_R \\ \Delta V_I \end{bmatrix} \quad \text{(C.4)}$$

In the above equation,

The parameters of the C_g matrix are given by,

$$cg_{11} = -I_I + \sin(\delta)K_{id1} + \cos(\delta)K_{iq1} \qquad cg_{13} = \sin(\delta)K_{id3} + \cos(\delta)K_{iq3}$$

$$cg_{14} = \sin(\delta)K_{id4} + \cos(\delta)K_{iq4} \qquad cg_{15} = \sin(\delta)K_{id5} + \cos(\delta)K_{iq5}$$

$$cg_{16} = \sin(\delta)K_{id6} + \cos(\delta)K_{iq6} \qquad cg_{21} = I_R - \cos(\delta)K_{id1} + \sin(\delta)K_{iq1}$$

$$cg_{23} = -\cos(\delta)K_{id3} + \sin(\delta)K_{iq3} \qquad cg_{24} = -\cos(\delta)K_{id4} + \sin(\delta)K_{iq4}$$

$$cg_{25} = -\cos(\delta)K_{id5} + \sin(\delta)K_{iq5} \qquad cg_{26} = -\cos(\delta)K_{id6} + \sin(\delta)K_{iq6}$$

The parameters of the Y_g matrix are given by,

$$yg_{11} = -\sin(\delta)K_{id7} - \cos(\delta)K_{iq7} \qquad yg_{12} = -\sin(\delta)K_{id8} - \cos(\delta)K_{iq8}$$

$$yg_{21} = \cos(\delta)K_{id7} - \sin(\delta)K_{iq7} \qquad yg_{22} = \cos(\delta)K_{id8} - \sin(\delta)K_{iq8}$$

C.1.2 Generator Model Including Stator Transients

Two additional differential equations for the stator flux components in d-q axes are added to the synchronous machine model, when the AC network is represented using a dynamic phasor model. Therefore, an 8^{th} order model is used for round rotor

type and a 7^{th} order model is used for salient pole type. The round rotor type (8^{th} order) generator model is formulated in the following text. The model can be easily simplified to the salient pole model by removing the second damper winding in the q-axis.

The changes in the d-q axes currents are given by equations (C.5) and (C.6) respectively.

$$\Delta i_d = K_{id3b}\Delta\Phi_d + K_{id4b}\Delta\Phi_{fd} + K_{id5b}\Delta\Phi_{1d} \tag{C.5}$$

In the above equation,

$K_{id3b} = -\frac{L_{ad}L_{ppd}(L_{fd}+L_{1d})}{L_l L_d L_{fd} L_{1d}} - \frac{1}{L_d}$

$K_{id4b} = \frac{L_{ppd}}{L_l L_{fd}}$

$K_{id5b} = \frac{L_{ppd}}{L_l L_{1d}}$

where, $L_{ppd} = 1/[\frac{1}{L_l} + \frac{1}{L_{ad}} + \frac{1}{L_{fd}} + \frac{1}{L_{1d}}]$.

$$\Delta i_q = K_{iq6b}\Delta\Phi_q + K_{iq7b}\Delta\Phi_{1q} + K_{iq8b}\Delta\Phi_{2q} \tag{C.6}$$

In the above equation,

$K_{iq6b} = -\frac{L_{aq}L_{ppq}(L_{1q}+L_{2q})}{L_l L_q L_{1q} L_{2q}} - \frac{1}{L_q}$

$K_{iq7b} = \frac{L_{ppq}}{L_l L_{1q}}$

$K_{iq8b} = \frac{L_{ppq}}{L_l L_{2q}}$

where, $L_{ppq} = 1/[\frac{1}{L_l} + \frac{1}{L_{aq}} + \frac{1}{L_{1q}} + \frac{1}{L_{2q}}]$.

The generator state space model is given by equation (C.7). The model is given

in the form of ($\Delta\dot{X}_g = A_g\ \Delta X_g + B_g\ \Delta U_g + E_g\ \Delta V_g$). There are eight state variables: rotor angle(δ), rotor speed (ω_0), d-axis stator winding flux (Φ_d), d-axis field winding flux (Φ_{fd}), d-axis damper winding flux (Φ_{1d}), q-axis stator winding flux (Φ_q), q-axis first damper winding flux (Φ_{1q}) and q-axis second damper winding flux (Φ_{2q}) and two inputs: mechanical torque (T_m) and voltage applied to the field winding (E_{fd}) in the system.

$$
\begin{bmatrix} \Delta\dot{\delta} \\ \Delta\dot{\omega}_r \\ \Delta\dot{\Phi}_d \\ \Delta\dot{\Phi}_{fd} \\ \Delta\dot{\Phi}_{1d} \\ \Delta\dot{\Phi}_q \\ \Delta\dot{\Phi}_{1q} \\ \Delta\dot{\Phi}_{2q} \end{bmatrix} =
\begin{bmatrix}
0 & ag_{12b} & 0 & 0 & 0 & 0 & 0 & 0 \\
0 & ag_{22b} & ag_{23b} & ag_{24b} & ag_{25b} & ag_{26b} & ag_{27b} & ag_{28b} \\
ag_{31b} & ag_{32b} & ag_{33b} & ag_{34b} & ag_{35b} & ag_{36b} & 0 & 0 \\
0 & 0 & ag_{43b} & ag_{44b} & ag_{45b} & 0 & 0 & 0 \\
0 & 0 & ag_{53b} & ag_{54b} & ag_{55b} & 0 & 0 & 0 \\
ag_{61b} & ag_{62b} & ag_{63b} & 0 & 0 & ag_{66b} & ag_{67b} & ag_{68b} \\
0 & 0 & 0 & 0 & 0 & ag_{76b} & ag_{77b} & ag_{78b} \\
0 & 0 & 0 & 0 & 0 & ag_{86b} & ag_{87b} & ag_{88b}
\end{bmatrix}
\begin{bmatrix} \Delta\delta \\ \Delta\omega_r \\ \Delta\Phi_d \\ \Delta\Phi_{fd} \\ \Delta\Phi_{1d} \\ \Delta\Phi_q \\ \Delta\Phi_{1q} \\ \Delta\Phi_{2q} \end{bmatrix} +
\begin{bmatrix}
0 & 0 \\
bg_{21b} & 0 \\
0 & 0 \\
0 & bg_{42b} \\
0 & 0 \\
0 & 0 \\
0 & 0 \\
0 & 0
\end{bmatrix}
\begin{bmatrix} \Delta T_m \\ \Delta E_{fd} \end{bmatrix} +
\begin{bmatrix}
0 & 0 \\
0 & 0 \\
eg_{31b} & eg_{32b} \\
0 & 0 \\
0 & 0 \\
eg_{61b} & eg_{62b} \\
0 & 0 \\
0 & 0
\end{bmatrix}
\begin{bmatrix} \Delta V_R \\ \Delta V_I \end{bmatrix} \quad \text{(C.7)}
$$

In the above equation,

The parameters of the A_g matrix are given by,

$$ag_{12b} = \omega_0 \qquad ag_{22b} = -\frac{K_d}{M}$$

$$ag_{23b} = \frac{1}{M}[-i_q + \Phi_q K_{id3b}] \qquad ag_{24b} = \frac{1}{M}[\Phi_q K_{id4b}]$$

$$ag_{25b} = \frac{1}{M}[\Phi_q K_{id5b}] \qquad ag_{26b} = -\frac{1}{M}[-i_d + \Phi_d K_{iq6b}]$$

$$ag_{27b} = -\frac{1}{M}[\Phi_d K_{iq7b}] \qquad ag_{28b} = -\frac{1}{M}[\Phi_d K_{iq8b}]$$

$$ag_{31b} = \omega_0 e_q \qquad ag_{32b} = \omega_0 \Phi_q$$

$$ag_{33b} = \omega_0 R_a K_{id3b} \qquad ag_{34b} = \omega_0 R_a K_{id4b}$$

$$ag_{35b} = \omega_0 R_a K_{id5b} \qquad ag_{36b} = \omega_0$$

$$ag_{43b} = \frac{\omega_0 R_{fd} L_{ppd}}{L_l L_{fd}} \qquad ag_{44b} = -\frac{\omega_0 R_{fd} L_{ppd}}{L_{fd}}[\frac{1}{L_l} + \frac{1}{L_{ad}} + \frac{1}{L_{1d}}]$$

$$ag_{45b} = \frac{\omega_0 R_{fd} L_{ppd}}{L_{fd} L_{1d}} \qquad ag_{53b} = \frac{\omega_0 R_{1d} L_{ppd}}{L_l L_{1d}}$$

$$ag_{54b} = \frac{\omega_0 R_{1d} L_{ppd}}{L_{fd} L_{1d}} \qquad ag_{55b} = -\frac{\omega_0 R_{1d} L_{ppd}}{L_{1d}}[\frac{1}{L_l} + \frac{1}{L_{ad}} + \frac{1}{L_{fd}}]$$

$$ag_{61b} = -\omega_0 e_d \qquad ag_{62b} = -\omega_0 \Phi_d$$

$$ag_{63b} = -\omega_0 \qquad ag_{66b} = \omega_0 R_a K_{iq6b}$$

$$ag_{67b} = \omega_0 R_a K_{iq7b} \qquad ag_{68b} = \omega_0 R_a K_{iq8b}$$

$$ag_{76b} = \frac{\omega_0 R_{1q} L_{ppq}}{L_l L_{1q}} \qquad ag_{77b} = -\frac{\omega_0 R_{1q} L_{ppq}}{L_{1q}}[\frac{1}{L_l} + \frac{1}{L_{aq}} + \frac{1}{L_{2q}}]$$

$$ag_{78b} = \frac{\omega_0 R_{1q} L_{ppq}}{L_{1q} L_{2q}} \qquad ag_{86b} = \frac{\omega_0 R_{2q} L_{ppq}}{L_l L_{1q}}$$

$$ag_{87b} = \frac{\omega_0 R_{2q} L_{ppq}}{L_{1q} L_{2q}} \qquad ag_{88b} = -\frac{\omega_0 R_{2q} L_{ppq}}{L_{2q}}[\frac{1}{L_l} + \frac{1}{L_{aq}} + \frac{1}{L_{1q}}]$$

The parameters of the B_g matrix are given by,

$$bg_{21b} = \frac{1}{M} \qquad bg_{42b} = \frac{\omega_0 R_{fd}}{L_{ad}}$$

The parameters of the E_g matrix are given by,

$$eg_{31b} = \omega_0 \sin(\delta) \qquad eg_{32b} = -\omega_0 \cos(\delta)$$

$$eg_{61} = \omega_0 \cos(\delta) \qquad eg_{62} = \omega_0 \sin(\delta)$$

The R-I components of the output current of the generator can be expressed in terms of the state variables as given in equation (C.8). The current equation is given in the form of ($\Delta I_g = C_g\ \Delta X_g$).

$$\begin{bmatrix} \Delta I_R \\ \Delta I_I \end{bmatrix} = \begin{bmatrix} cg_{11b} & 0 & cg_{13b} & cg_{14b} & cg_{15b} & cg_{16b} & cg_{17b} & cg_{18b} \\ cg_{21b} & 0 & cg_{23b} & cg_{24b} & cg_{25b} & cg_{26b} & cg_{27b} & cg_{28b} \end{bmatrix} \begin{bmatrix} \Delta\delta \\ \Delta\omega_r \\ \Delta\Phi_d \\ \Delta\Phi_{fd} \\ \Delta\Phi_{1d} \\ \Delta\Phi_q \\ \Delta\Phi_{1q} \\ \Delta\Phi_{2q} \end{bmatrix} \tag{C.8}$$

In the above equation,

The parameters of the C_g matrix are given by,

$cg_{11b} = -I_I$

$cg_{13b} = \sin(\delta)K_{id3b}$

$cg_{14b} = \sin(\delta)K_{id4b}$

$cg_{15b} = \sin(\delta)K_{id5b}$

$cg_{16b} = \cos(\delta)K_{iq6b}$

$cg_{17b} = \cos(\delta)K_{iq7b}$

$cg_{18b} = \cos(\delta)K_{iq8b}$

$cg_{21} = I_R$

$cg_{23b} = -\cos(\delta)K_{id3b}$

$cg_{24b} = -\cos(\delta)K_{id4b}$

$cg_{25b} = -\cos(\delta)K_{id5b}$

$cg_{26b} = \sin(\delta)K_{iq6b}$

$cg_{27b} = \sin(\delta)K_{iq7b}$

$cg_{28b} = \sin(\delta)K_{iq8b}$

C.2 Linearized Exciter Model (AC4A)

The alternator supplied controlled rectifier type exciter system (AC4A) given in [37] is used in the analysis. The simplified control block diagram is shown in Figure C.1.

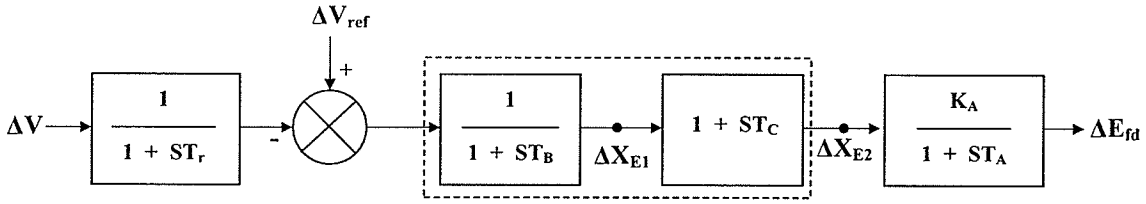

Figure C.1: AC4A exciter control block diagram (simplified as required for small signal stability assessment)

The linearized model consists of three state variables: Field voltage (E_{fd}), X_{E1} and X_{E2}. The linearized model is given in Equation (C.9) in the form of ($\Delta\dot{X}_e = A_e\ \Delta X_e + B_e\ \Delta U_e + E_e\ \Delta V_g$).

$$\begin{bmatrix} \Delta\dot{E}_{fd} \\ \Delta\dot{X}_{E1} \\ \Delta\dot{X}_{E2} \end{bmatrix} = \begin{bmatrix} ae_{11} & ae_{12} & ae_{13} \\ 0 & ae_{22} & ae_{23} \\ 0 & 0 & ae_{33} \end{bmatrix} \begin{bmatrix} \Delta E_{fd} \\ \Delta X_{E1} \\ \Delta X_{E2} \end{bmatrix} + \begin{bmatrix} be_1 \\ be_2 \\ 0 \end{bmatrix} \begin{bmatrix} \Delta V_{ref} \end{bmatrix} + \begin{bmatrix} 0 & 0 \\ 0 & 0 \\ ee_{31} & ee_{32} \end{bmatrix} \begin{bmatrix} \Delta V_R \\ \Delta V_I \end{bmatrix} \quad \text{(C.9)}$$

In the above equation,

The parameters of the A_e matrix are given by,

$ae_{11} = -\frac{1}{T_A}$ $\qquad$ $ae_{12} = \frac{K_A}{T_A}[1 - \frac{T_C}{T_B}]$

$ae_{13} = -\frac{K_A T_C}{T_A T_B}$ $\qquad$ $ae_{22} = -\frac{1}{T_B}$

$ae_{23} = -\frac{1}{T_B}$ $\qquad$ $ae_{33} = -\frac{1}{T_r}$

The parameters of the B_e matrix are given by,

$be_1 = \frac{K_A T_C}{T_A T_B}$ $\qquad$ $be_2 = \frac{1}{T_B}$

The parameters of the E_e matrix are given by,

$ee_{31} = \frac{V_R}{T_r V_l}$ $\qquad$ $ee_{32} = \frac{V_I}{T_r V_l}$

where V_l is the magnitude of the terminal voltage.

C.3 Linearized Governor-Turbine Model

The mechanical-hydraulic governor and the hydro turbine with non-elastic water column (without surge tank) given in [38] are used. The control block diagram is shown in Figure C.2.

The linearized model consists of five state variables, four from the governor (X_{t1}), X_{t2}, X_{t3} and X_{t4}) and the flow rate (q) from the turbine. The linearized model is given in Equation (C.10) in the form of ($\Delta\dot{X}_T = A_T\ \Delta X_T + AA_T\ \Delta\omega_r + B_T\ \Delta U_T$).

$$\begin{bmatrix} \Delta\dot{X}_{t1} \\ \Delta\dot{X}_{t2} \\ \Delta\dot{X}_{t3} \\ \Delta\dot{X}_{t4} \\ \Delta\dot{q} \end{bmatrix} = \begin{bmatrix} at_{11} & at_{12} & 0 & at_{14} & 0 \\ at_{21} & 0 & 0 & 0 & 0 \\ 0 & at_{32} & at_{33} & 0 & 0 \\ 0 & at_{42} & 0 & at_{44} & 0 \\ 0 & 0 & at_{53} & 0 & at_{55} \end{bmatrix} \begin{bmatrix} \Delta X_{t1} \\ \Delta X_{t2} \\ \Delta X_{t3} \\ \Delta X_{t4} \\ \Delta q \end{bmatrix} + \begin{bmatrix} aat_1 \\ 0 \\ 0 \\ 0 \\ 0 \end{bmatrix} \begin{bmatrix} \Delta\omega_r \end{bmatrix} + \begin{bmatrix} bt_1 \\ 0 \\ 0 \\ 0 \\ 0 \end{bmatrix} \begin{bmatrix} \Delta\omega_{ref} \end{bmatrix} \quad \text{(C.10)}$$

In the above equation,

The parameters of the A_T matrix are given by,

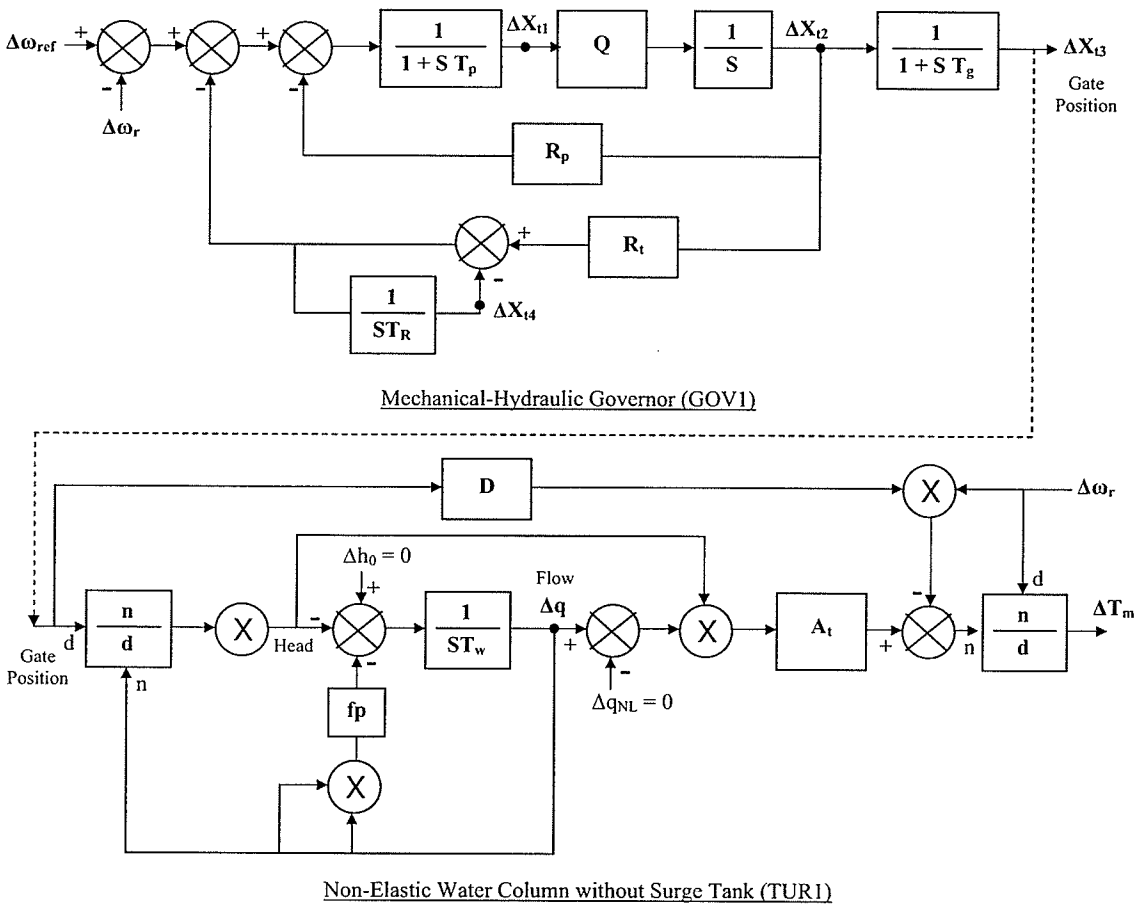

Figure C.2: Governor-turbine control block diagram (simplified as required for small signal stability assessment)

$at_{11} = -\frac{1}{T_p}$ $\quad at_{12} = -\frac{R_t+R_p}{T_p}$

$at_{14} = \frac{1}{T_p}$ $\quad at_{21} = q$

$at_{32} = \frac{1}{T_g}$ $\quad at_{33} = -\frac{1}{T_g}$

$at_{42} = \frac{R_t}{T_R}$ $\quad at_{44} = -\frac{1}{T_R}$

$at_{53} = \frac{2q^2}{T_w G^3}$ $\quad at_{55} = -\frac{2q}{T_w}[\frac{1}{G^2} - f_p]$

where, q is the flow rate and G is the gate position ($\equiv X_{t3}$)

The contributions from the generator speed are given by parameters of AA_T matrix,

$aat_1 = -\frac{1}{T_p}$

The parameters of the B_e matrix are given by,

$bt_1 = \frac{1}{T_p}$

The mechanical torque produced by the turbine is given in equation (C.11).

$$\begin{bmatrix} \Delta T_m \end{bmatrix} = \begin{bmatrix} 0 & 0 & ct_3 & 0 & ct_5 \end{bmatrix} \begin{bmatrix} \Delta X_{t1} \\ \Delta X_{t2} \\ \Delta X_{t3} \\ \Delta X_{t4} \\ \Delta q \end{bmatrix} + \begin{bmatrix} -DG - \frac{A_t q^2}{G^2}[q - q_{NL}] \end{bmatrix} \begin{bmatrix} \Delta \omega_r \end{bmatrix} \quad \text{(C.11)}$$

In the above equation,

$ct_3 = -\frac{2A_t q^2}{G^3}[q - q_{NL}]$ $\qquad$ $ct_5 = \frac{A_t}{G^2}[3q^2 - 2q_{NL}q]$

where, q_{NL} is the no-load flow rate of the turbine.

C.4 State Space Generator Model With Exciter And Governor

The linearized generator model is combined with the exciter and governor models. In summery, the generator model can be written as,

$$\Delta \dot{X}_g = A_g\ \Delta X_g + B_g\ \Delta U_g + E_g\ \Delta V_g \quad \text{(C.12)}$$

$$\Delta I_g = C_g\ \Delta X_g - Y_g\ \Delta V_g \quad \text{(C.13)}$$

This model is equivalent to the conventional generator model given by equations (C.3) and (C.4) and to the detailed generator model given by equations (C.7) and (C.8). In the detailed model, all the elements of Y_g matrix are zero.

C.4.1 Generator-Exciter Combination

The summarized exciter model can be written as,

$$\Delta \dot{X}_e = A_e \ \Delta X_e + B_e \ \Delta V_{ref} + E_e \ \Delta V_g \tag{C.14}$$

This model is equivalent to the exciter model given by equation (C.9).

ΔE_{fd}, which is a state variable of the exciter model (equation (C.14)), is an input to the generator model(equation (C.12)). Therefore, the generator and the exciter are combined through ΔE_{fd}.

C.4.2 Generator-Governor-Turbine Combination

The summarized governor-turbine model can be written as,

$$\Delta \dot{X}_T = A_T \ \Delta X_T + AA_T \ \Delta \omega_r + B_T \ \Delta \omega_{ref} \tag{C.15}$$

$$\Delta T_m = C_T \ \Delta X_T + CC_T \ \Delta \omega_r \tag{C.16}$$

This model is equivalent to the governor-turbine model given by equations (C.10) and (C.11).

ΔT_m, which is the output of the governor-turbine model (equation (C.16)), is an input to the generator model(equation (C.12)). Therefore equations (C.12) and (C.16) are combined together to eliminate ΔT_m terms.

C.4.3 Overall State Space Model

The overall system given in equations (C.17) and (C.18) can be obtained by combining the generator, exciter and governor-turbine modes as mentioned above. The overall system has the exciter voltage reference (ΔV_{ref}) and the governor speed reference ($\Delta\omega_{ref}$) as the inputs. A_G, B_G, E_G, C_G and Y_G are the resultant matrices.

$$\begin{bmatrix} \Delta\dot{X}_g \\ \Delta\dot{X}_e \\ \Delta\dot{X}_T \end{bmatrix} = \begin{bmatrix} A_G \end{bmatrix} \begin{bmatrix} \Delta\dot{X}_g \\ \Delta\dot{X}_e \\ \Delta\dot{X}_T \end{bmatrix} + \begin{bmatrix} B_G \end{bmatrix} \begin{bmatrix} \Delta\omega_r \\ \Delta V_{ref} \end{bmatrix} + \begin{bmatrix} E_G \end{bmatrix} \begin{bmatrix} \Delta V_R \\ \Delta V_I \end{bmatrix} \quad \text{(C.17)}$$

$$\begin{bmatrix} \Delta I_G \end{bmatrix} = \begin{bmatrix} C_G \end{bmatrix} \begin{bmatrix} \Delta\dot{X}_g \\ \Delta\dot{X}_e \\ \Delta\dot{X}_T \end{bmatrix} - \begin{bmatrix} Y_G \end{bmatrix} \begin{bmatrix} \Delta V_R \\ \Delta V_I \end{bmatrix} \quad \text{(C.18)}$$

C.5 Multi Mass Turbine Model

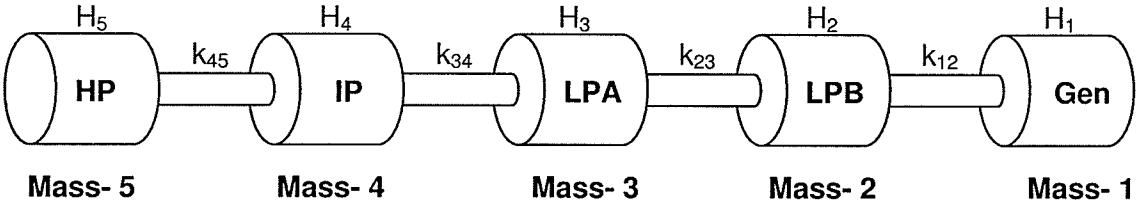

Figure C.3: Multi-mass generator-turbine system

The five-mass generator turbine system shown in Figure C.3 is used in the analysis. The speed and the rotor angle of each mass unit are modeled as state variables. The

dynamic equations of the rotor speed and the angle of each mass unit are given by Equations C.19 and C.20 respectively.

$$2H_i\ \Delta\dot{\omega}_i = k_{i+1,i}(\Delta\delta_{i+1} - \Delta\delta_i) - k_{i,i-1}(\Delta\delta_i - \Delta\delta_{i-1}) - K_{di}\ \Delta\omega_i + \Delta T_i \quad \text{(C.19)}$$

$$\Delta\dot{\delta}_i = \frac{1}{\omega_0}\Delta\omega_i \quad \text{(C.20)}$$

Where, $k_{i,j}$ is the spring constant between i^{th} mass and j^{th} mass and so on. H_i and K_{di} are the inertia constant and the damping coefficient of i^{th} mass respectively. T_i is the torque generated by i^{th} mass.

The dynamic equations of the rotor speed and the angle of each mass unit are combined together to obtain the overall dynamic model of the entire multi-mass system. The entire system has 10 state variables including the generator speed and rotor angle.

Appendix D

An Algorithm For Proposed Hybrid Small Signal Model

The proposed hybrid small signal model can be added into existing small signal stability analysis programs. The flowchart is given in Figure D.1 and the procedure is described as follows.

- The power flow data (Eg: PSS^{TM}E raw data file) and the dynamic data (dynamic data file) are required in conventional small signal programs to create the linearized model of the power system. In this new technique, an additional data file (dynamic representation file) is required to define the dynamic areas. Each dynamic area and the bus numbers in the dynamic area should be defined in this file.

- The data files are read and the data are divided into dynamic area data and conventional model (admittance matrix model) data. The raw data and dynamic data files are created for each dynamic area and for the rest of the system (conventional model).

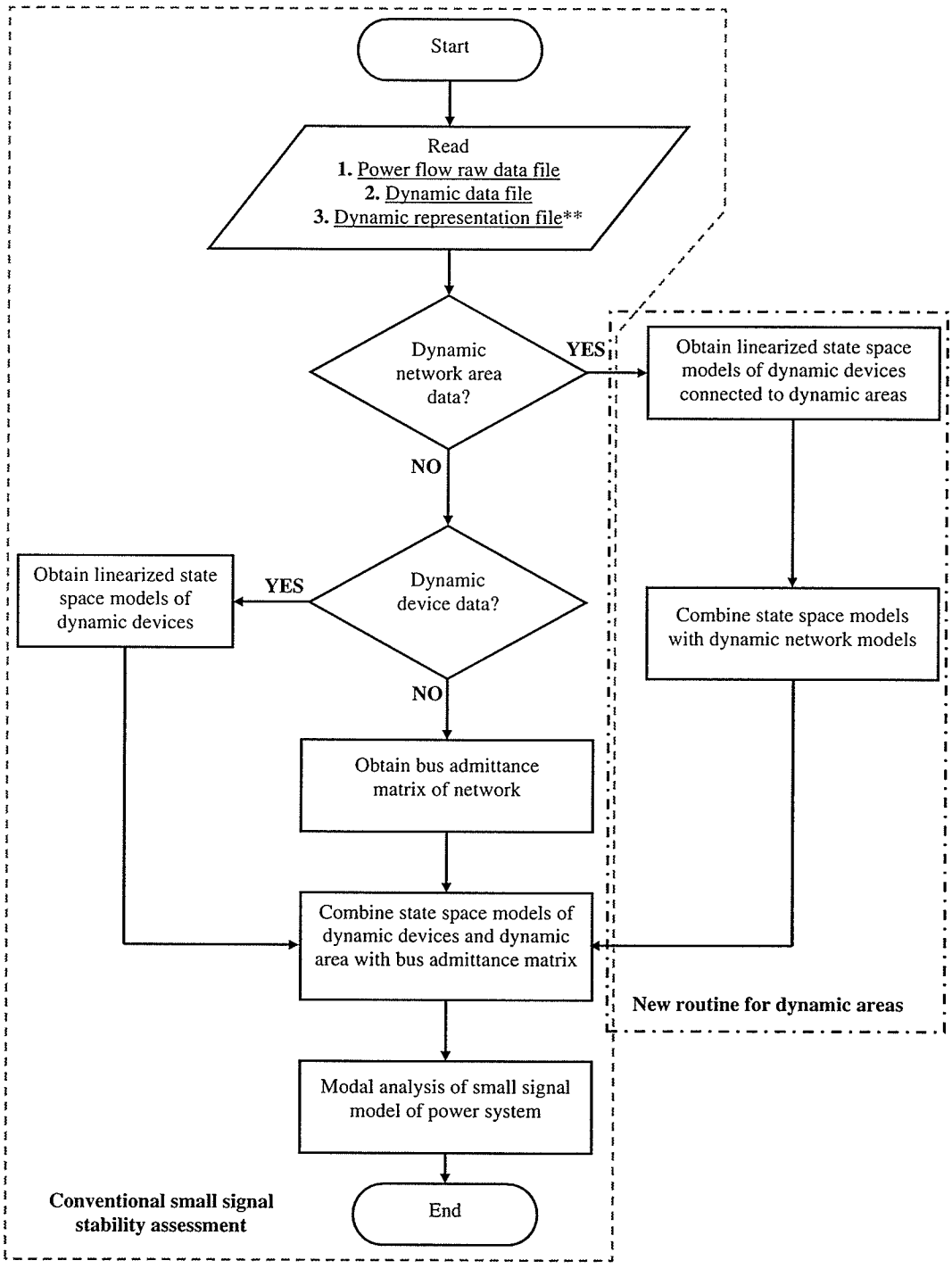

Figure D.1: Flowchart of proposed hybrid small signal model

- For each dynamic area, the dynamic AC network model is created and it is combined with the linearized dynamic models of the dynamic devices in that area to obtain the state space model of the dynamic area (a current injection model to the rest of the system).

- For the rest of the systems, the linearized state space models of the dynamic devices are obtained and the admittance matrix relationship of the AC network is obtained.

- The current injection models of the dynamic areas and the dynamic devices of the rest of the system are combined with the admittance matrix AC network model of the rest of the system to obtain the overall state space model of the system.

- The eigenvalues and the eigenvectors of the system state matrix are obtained and the small signal stability of the system is analyzed. Further, the time and frequency responses can be obtained from the state space model.

Appendix E

Governor-Turbine Torsional Interactions With AC Network

E.1 Test System -IEEE First Benchmark Model

The IEEE first benchmark model for the subsynchronous resonance studies is used to analyze the torsional interactions between the generator-turbine unit and the AC network. The test system is shown in Figure E.1. The generator and the turbine parameters are as in [39]. For the simplicity, an exciter is not included and the exciter mass is not modeled. Under nominal conditions, the following parameters are used for the AC network.

Generator transformer inductance, $L_t = 0.14pu$

Transmission line resistance, $R_l = 0.02pu$

Transmission line total inductance, $L_l = 0.56pu$

Series compensation capacitance (value is changeable), $C = 2.7pu$

(Percentage compensation of the line = 66%)

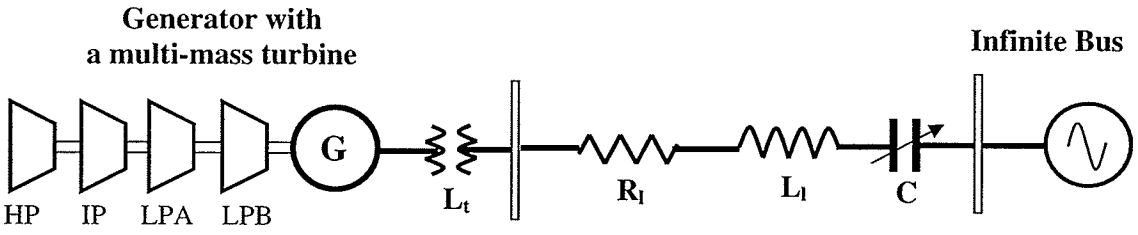

Figure E.1: IEEE first benchmark model for subsynchronous resonance studies - fault reactance is not included

Table E.1: Some important modes of the test system

Mode	Freq. (Hz)	D (%)	Major Participant
1	16.25	-0.11952	Gen,LPA,HP,IP,LPB (SSO)
2	25.43	0.00975	HP,LPB,IP,Gen,LPA (SSO)
3	32.19	-0.000036	LPB,Gen,LPA,HP (SSO)
4	47.45	0.0000001	IP,HP,LPA (SSO)
5	20.62	2.25	AC network
6	1.69	3.2	Generator (Electromechanical)

E.2 Small Signal Stability Model of Test System

The linearized model of the test system consists of 20 state variables: generator & turbine - 16 state variables and AC netwotk - 4 state variables. The modes and the modal characteristics of the system are obtained from the eigenvalue analysis of the linearized model. Some important modes of the system are given in Table E.1.

Modes 1 to 4 are the torsional modes of the generator-turbine unit. Since the mechanical damping of the generator-turbine unit is ignored, the modes show very low damping. Modes 1 and 3 have slightly negative damping under the given conditions.

All the mass units participate in Mode-1, in which the generator mass is the main participant. Mode shapes show that the generator and LPB masses oscillate against the other three turbine masses in this mode. The HP turbine is the main participant of Mode-2 and all other mass units also contribute to this mode. LPA and LPB

turbines oscillate against the generator and IP and HP turbines in this mode. The LPB turbine oscillates against the generator and LPA turbine in Mode-3. HP and IP turbine participations in this mode are minor. Mode-4 shows the interactions of IP and HP turbines. IP turbine oscillate against HP turbine in this mode. The LPB turbine and the generator do not contribute to this mode. There are no significant participations of the state variables of the AC network in the torsional modes under the given conditions.

Mode-5 is a network mode, in which the AC network currents and voltages participates the most. Mode-6 is the electro mechanical mode of the system.

E.3 Generator-Turbine-AC network Torsional Interactions

The torsional interactions between the generator-turbine unit and the AC network depend on the level of series compensation of the transmission line. In order to investigate this, the value of the series capacitor is changed such that the line compensation varies in the range of 5% to 110%. The stability of the modes are evaluated using small signal model derived at each compensation level. Figure E.2 shows the polar plot of the modes obtained when the compensation level is changed. The damping versus compensation level characteristics are shown in Figure E.3.

The frequency of the network mode (Mode-5) changes from 10Hz to 50Hz within the range of compensation levels considered. When the line compensation is decreased from 110%, the network mode gets close to 16 Hz and the damping of Mode-1 decreases. When the line compensation is 83%, Mode-1 has highest negative damping. At this point, the frequency of the network mode is very close to the frequency of Mode-1 (16 Hz). In contrast to Mode-1, the network mode has highest positive damping at this point. High interactions between the state variables of generator-turbine

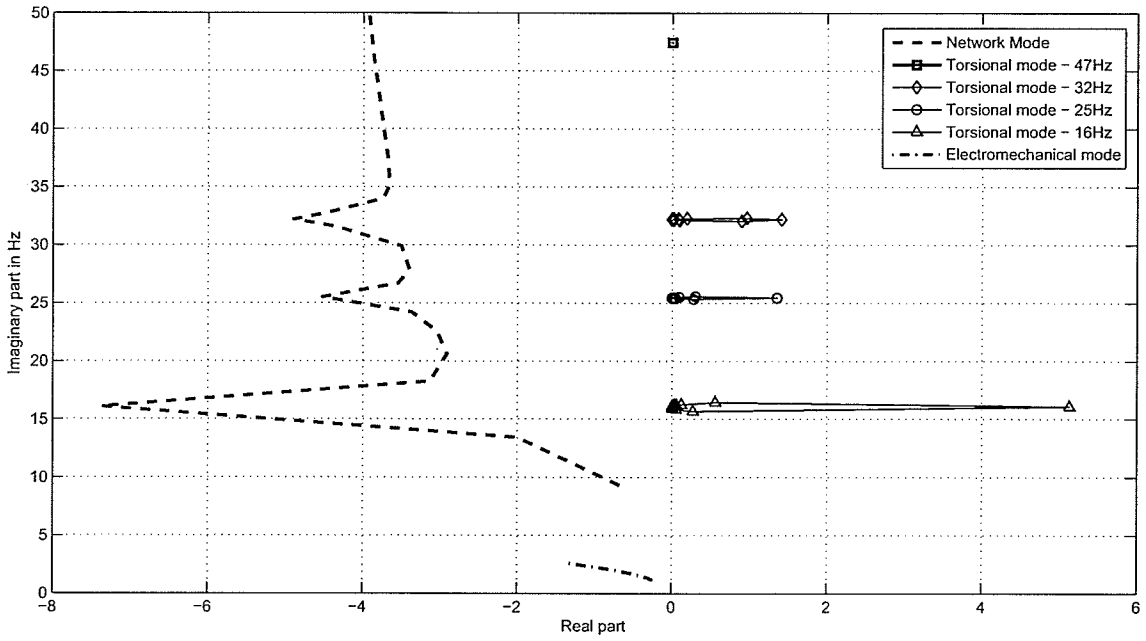

Figure E.2: Polar plot of the modes obtained when the compensation level is changed

unit and the state variables of the network can be observed in Mode-1 and network mode. The damping of Mode-1 starts to increase again as the line compensation is reduced further.

Similarly, the network mode gets close to Mode-2 (25Hz) in frequency as the line compensation drops to 51%. At this point, Mode-2 has highest negative damping. The damping of the mode starts to improve again as the line compensation drops further. If the line compensation is reduced further, the damping of Mode-3 gets worst. When the line compensation is 33%, the network mode is very close to Mode-3 (32Hz) in frequency and the torsional mode has worst damping.

It can be evidenced in Figures E.2 and E.3 that the changes in the network do not cause significant changes in Mode-4 (47Hz). Modal analysis shows that the generator mass does not participate in Mode-4 and the mode can not be observed in the generator speed or any other state variable of the generator. Therefore, Mode-4 can not

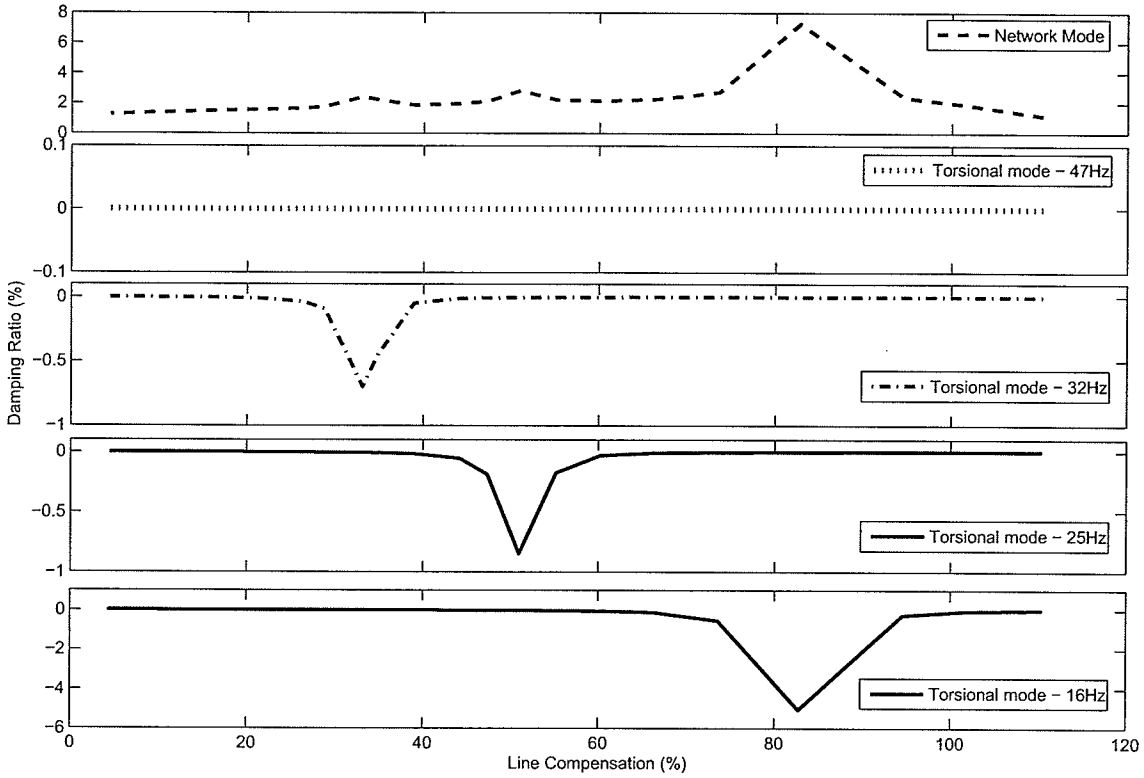

Figure E.3: Damping versus compensation level characteristics of the modes

be observed in the generator terminal or in the network. Because of this, the network mode can not interact with Mode-4 although it is close to Mode-4 in frequency.

The results of this analysis were verified using time domain simulations obtained using PSCAD/EMTDC. The IEEE first benchmark model available in the PSCAD/EMTDC library was used in the simulations. Under nominal conditions (66% line compensation), the changes in the generator speed for a 5%, 100ms pulse on the generator field voltage is shown in Figure E.4(a). Very low (-ve) damping of Mode-1 can be observed in the speed. As the line compensation decreases, the mode becomes more and more unstable. Figure E.4(b) shows the changes in generator speed when the line compensation is 73%. High instability of Mode-1 can be clearly observed in the speed. The good comparisons of the results of the small signal model with the results

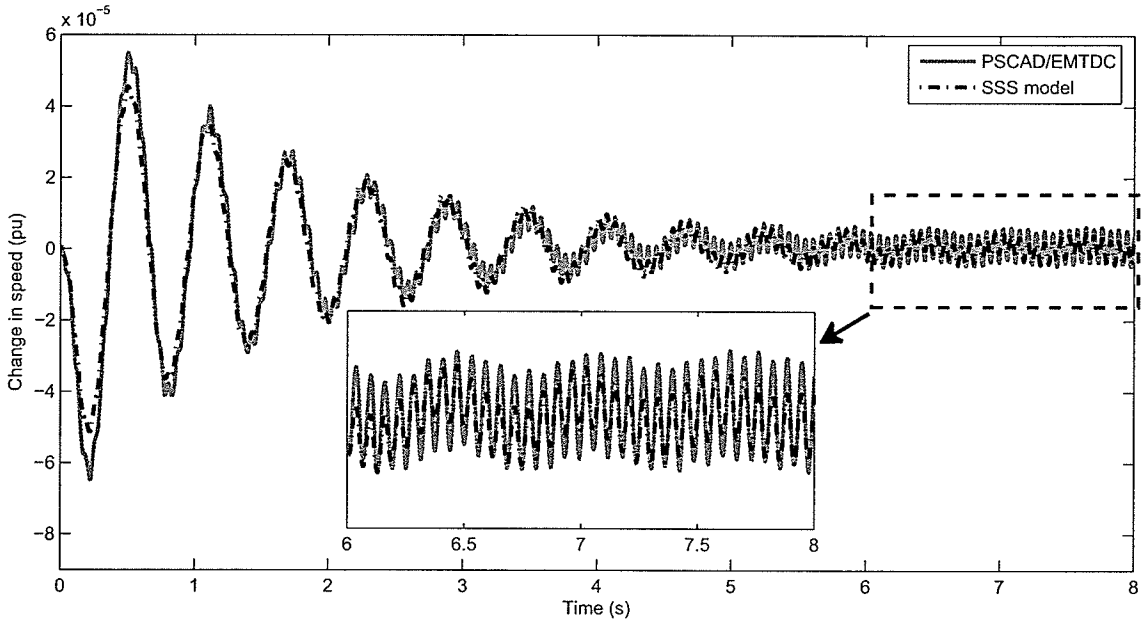

(a) Change in generator speed when line compensation is 66%(nominal value)

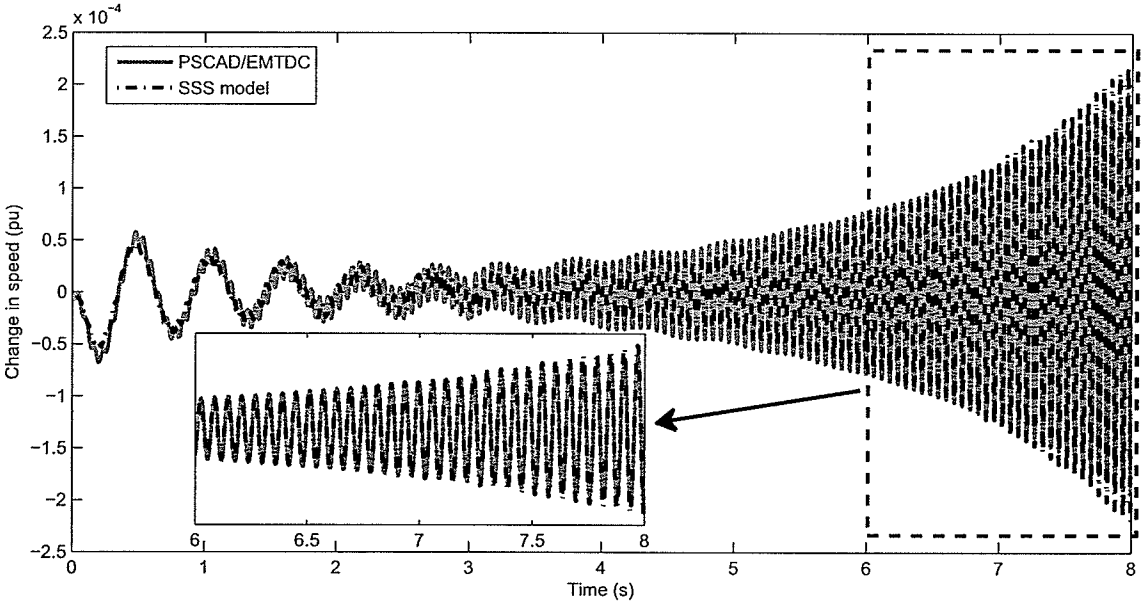

(b) Change in generator speed when line compensation is 73%

Figure E.4: Change in generator speed (in pu) for a 5%, 100ms pulse on the generator field voltage

of the PSCAD/EMTDC model confirm the accuracy of the linearized small signal model used in this analysis.

E.4 Summary of Analysis

The torsional modes of the generator-turbine units may interact with some modes of the AC network. If the network mode is close the torsional mode in frequency, the two modes may highly interact and this may even cause the instability in the torsional mode. In order to interact with the network, the torsional mode should be observed at the network. If it is not so, the torsional mode does not react to the changes in the network (or network mode).

This analysis further demonstrates the performance of the small signal stability assessment in analyzing subsynchronous frequency torsional interactions in power systems. The interactions can be analyzed quantitatively and the causes can be identified accurately. The modeling techniques described in this thesis can be used to obtain the linearized small signal model.

Acronyms

AC	Alternating Current
CC	Constant Current controller (rectifier)
CEA	Constant Extinction Angle controller (inverter)
CIGRE	International Council on Large Electric Systems
DAE	Dynamic and Algebraic Equations
DC	Direct Current
EMT	Electro Magnetic Transient
ESCR	Effective Short Circuit Ratio
FACTS	Flexible Alternative Current Transmission System
HP	High Pressure (turbine)
HVDC	High Voltage Direct Current
IEEE	Institution of Electrical and Electronics Engineers
IP	Intermediate Pressure (turbine)
LPA	Low Pressure - A (turbine)
LPB	Low Pressure - B (turbine)
PI	Proportional and Integral (controller)
PLO	Phase Lock Oscillator
SSDC	SubSynchronous Damping Controller
SSO	SubSynchronous Oscillation
SSR	SubSynchronous Resonance
SSS	Small Signal Stability
STATCOM	Static Synchronous Compensator
SVC	Static Var Compensator
UPFC	Unified Power Flow Controller
VC	Voltage Controller (inverter)
VSC	Voltage Source Converter

References

[1] G. Asplund, L. Carlsson, and O. Tollerz, "50 Years HVDC", *ABB Review 4/2003*, pp. 6–13.

[2] N.G. Hingorani, "High-voltage DC transmission: a power electronics workhorse", *IEEE Spectrum*, vol. 33, no. 4, pp. 63–72, April 1996.

[3] S. Arabi, G.J. Rogers, D.Y. Wong, P. Kundur, and M.G. Lauby, "Small Signal Stability Program Analysis of SVC and HVDC in AC Power Systems", *IEEE Transactions on Power Systems*, vol. 6, no. 3, pp. 1147–1153, August 1991.

[4] T. Smed and G. Andersson, "Utilizing HVDC to Damp Power Oscillations", *IEEE Transactions on Power Delivery*, vol. 8, no. 2, pp. 620–627, April 1993.

[5] M. Szechtman, L.A.S. Pilotto, W.W. Ping, E. Salgado, A.R. Carvalho, A. Wey, W.F. Long, F.L. Alvarado, C.L. Demarco, and S.L. Nilsson, "The Behaviour of Several HVDC Links Terminating in the Same Load Area", International Conference on Large High Voltage Electric Systems -CIGRE Paper 14-201, August 1992, vol. 1.

[6] L.A.S. Pilotto, M. Szechtman, A. Wey, W.F. Long, and S.L. Nilsson, "Synchronizing and Damping Torque Modulation Controllers for Multi-infeed HVDC Systems", *IEEE Transactions on Power Delivery*, vol. 10, no. 3, pp. 1505–1513, July 1995.

[7] IEEE SSR Working Group, "Terms, definitions and symbols for subsynchronous oscillations", *IEEE Transactions on Power Apparatus and Systems*, vol. PAS-104, no. 6, pp. 1326–1334, June 1985.

[8] M. Bahrman, E.V. Larsen, R.W. Piwko, and H.S. Patel, "Experience with HVDC-turbine-generator torsional interaction at Square Butte", *IEEE Transactions on Power Apparatus and Systems*, vol. PAS-99, no. 5, pp. 966–976, July-August 1980.

[9] M. Bahrman, E.V. Larsen, R.W. Piwko, and H.S. Patel, "Field Tests and Analysis of Torsional Iinteraction Between the Coal Creek Turbine-Generators and the CU HVDC System", *IEEE Transactions on Power Apparatus and Systems*, vol. PAS-100, no. 1, pp. 336–344, January 1981.

[10] R.W. Piwko and E.V. Larsen, "HVDC System For Damping of Subsynchrnous Oscillations", *IEEE Transactions on Power Apparatus and Systems*, vol. PAS-101, no. 7, pp. 2203–2211, July 1982.

[11] R.M. Hamouda, M.R. Iravani, and R. Hackam, "Torsional Oscillations of Series Capacitor Compensated AC/DC Systems", *IEEE Transactions on Power Systems*, vol. 4, no. 3, pp. 889–896, August 1989.

[12] Y.Y. Hsu and L. Wang, "Modal Control of An HVDC System For The Damping of Subsynchronous Oscillations", *IEE Proceedings*, vol. 136-C, no. 2, pp. 78–86, March 1989.

[13] D.J. Kim, H.K. Nam, and Y.H. Moon, "A Practical Approach to HVDC System Control for Damping Subsynchronous Oscillation Using the Novel Eigenvalue Analysis Program", *IEEE Transactions on Power Systems*, vol. 22, no. 4, pp. 1926–1934, November 2007.

[14] B. Gemmell and J. Laughran, "HVDC Offers the Key to Untapped Hydro Potential", *IEEE Power Engineering Review*, vol. 22, no. 5, pp. 8–11, May 2002.

[15] P. Kundur, *Power System Stability and Control*, McGrew-Hill, Inc, 1994.

[16] D.Y. Wong, G.J. Rogers, B. Porretta, and P. Kundur, "Eigenvalue Analysis of Very Large Power Systems", *IEEE Transactions on Power Systems*, vol. 3, no. 2, pp. 472–480, May 1988.

[17] IEEE/CIGRE Joint TF on Stability Terms and Definitions, "Definition and Classification of Power System Stability", *IEEE Transactions on Power Systems*, vol. 19, no. 2, pp. 1387–1401, May 2004.

[18] A.M. Lyapunov, *Stability of Motion-English Translation*, Academic Press Inc., 1967.

[19] P. Kundur, G.J. Rogers, D.Y. Wong, L. Wang, and M.G. Lauby, "A comprehensive computer program package for small signal stability analysis of power systems", *IEEE Transactions on Power Systems*, vol. 5, no. 2, pp. 1076–1083, November 1990.

[20] N. Martins, S. Gomes Jr., P. E. M. Quinto, J.C.R. Ferraz, S.L. Varricchio, and A. de Castro, "Some recent developments in small-signal stability and control", Proc. of Power Engineering Society Winter Meeting 2002, New York, 2002, pp. 1171–1177.

[21] C. Osauskas and A. Wood, "Small-Signal Dynamic Modeling of HVDC Systems", *IEEE Transactions on Power Delivery*, vol. 18, no. 1, pp. 220–225, January 2003.

[22] M. Parniani and M.R. Iravani, "Computer analysis of small-signal stability of power systems including network dynamics", *IEE Procedings of Generation, Transmission and Distribution*, vol. 142, no. 6, pp. 613–617, November 1995.

[23] K.R. Padiyar and M.K. Geetha, "Study of torsional interactions in multi-terminal DC systems through small signal stability analysis", International Conference on AC and DC Power Transmission, September 1991, pp. 411–413.

[24] J.M. Undrill and T.E. Kostyniak, "Subsynchronous Oscillations Part1 - Comprehensive System Stability Analysis", *IEEE Transactions on Power Apparatus and Systems*, vol. PAS-95, no. 4, pp. 1446–1455, February 1976.

[25] D. Jovcic, N. Pahalawaththa, and M. Zavahir, "Analytic Modeling of HVDC-HVAC systems", *IEEE Transactions on Power Delivery*, vol. 14, pp. 506–511, April 1999.

[26] X. Yang and C. Chen, "HVDC dynamic modelling for small signal analysis", *IEE Proceedings-Generation, Transmission and Distribution*, vol. 151, no. 6, pp. 740–746, November 2004.

[27] M. Szechtman, T. Wess, and C.V. Thio, "First Benchmark Model for HVDC Control Studies", *Electra*, , no. 135, pp. 55–75, April 1991.

[28] *PSCAD/EMTDC Users Manual*, Manitoba HVDC Research Centre, Winnipeg, Canada, 2002.

[29] M.A. Pai, *Energy Function Analysis for Power System Stability*, Kluwer Academic Publishers, 1989.

[30] C. Osauskas, D.J. Hume, and A. Wood, "A small signal frequency domain model of an HVDC converter", *IEE Proceedings-Generation, Transmission and Distribution*, vol. 148, no. 6, pp. 573–578, April 2001.

[31] D.J. Hume, *Harmonic and Interharmonic Cross Modulation in HVDC Links*, PhD thesis, University of Canterbury, New Zealand, 2002.

[32] E.V. Larsen, D.H. Baker, and J.C. McIver, "Low order harmonic interaction on ac/dc systems", *IEEE Transactions on Power Delivery*, vol. 4, no. 1, pp. 493501, January 1989.

[33] K.R. Padiyar, *Hvdc Power Transmission Systems: Technology and System Interactions*, John Wiley & Sons., 1990.

[34] V.K.Sood, V. Khatri, and H.Jin, "Performance Assessment using EMTP of Two Gate Firing Units for HVDC Converters Operating With Weak AC Systems", IPST95-International conference on power system transients, Lisbon, September 1995, pp. 517–522.

[35] W. Hammer, *Dynamic Modeling of Line and Capacitor Commutated Converters for HVDC Power Transmission*, PhD thesis, Swiss Federal Institute of Technology, Zurich, 2003.

[36] D.A. Woodford, "Validation of Digital Simulation of DC Links", *IEEE Transactions on Power Apparatus and Systems*, vol. PAS-104, no. 9, pp. 2588–2595, September 1985.

[37] IEEE Std. 421.5-1992, *IEEE Recommended Practice for Excitation System Models for Power System Stability Studies*, IEEE, 1992.

[38] W.G. on Prime Mover and Energy Supply Models for System Dynamic Performance Studies, "Hydraulic Turbine And Turbine Control Models For System Dynamic Studies", *IEEE Transactions on Power Systems*, vol. 7, no. 1, pp. 167–179, February 1992.

[39] IEEE Subsynchronous Resonance TF, "First Benchmark Model For Computer Simulation Of Subsynchronous Resonance", *IEEE Transactions on Power Ap-*

paratus and Systems, vol. PAS-96, no. 5, pp. 1565–1572, September/October 1977.

[40] Chi-Tsong Chen, *Linear System Theory and Design*, Oxford University Press, 1999.

[41] I.J. Perez-Arriaga, G.C. Verghese, and F.C. Schweppe, "Selective Modal Analysis with Applications to Electric Power Systems, PART I: Heuristic Introduction", *IEEE Transactions on Power Apparatus and Systems*, vol. PAS-101, no. 9, pp. 3117–3125, September 1982.

[42] G.C. Verghese, I.J. Perez-Arriaga, and F.C. Schweppe, "Selective Modal Analysis With Applications to Electric Power Systems, Part II: The Dynamic Stability Problem", *IEEE Transactions on Power Apparatus and Systems*, vol. PAS-101, no. 9, pp. 3126–3134, September 1982.

[43] L.E. Jones and G. Andersson, "Selecting Robust Input Signals For HVDC Damping Controllers", Conference on AC and DC Power Transmission-IEE, April-May 1996, pp. 152–156.

[44] P. Kundur, M. Klein, G.J. Rogers, and M.S. Zywno, "Application of Power System Stabilizers for Enhancement of Overall System Stability", *IEEE Transactions on Power Systems*, vol. 4, no. 2, pp. 614–626, May 1989.